UNIVERSIDADE DE SÃO PAULO
Escola de Engenharia de São Carlos

Dynamic-based damage detection in scaled unreinforced masonry panels

Detecção de danos com base na resposta dinâmica em painéis de alvenaria não armada em escala reduzida

Júlia Maria de França Moura

Dissertação de Mestrado do Programa de Pós-Graduação em Engenharia Civil (Engenharia de Estruturas) da Escola de Engenharia de São Carlos, Universidade de São Paulo

EESC · USP

Júlia Maria de França Moura

Dynamic-based damage detection in scaled unreinforced masonry panels

Dissertation submitted to the Graduate Program in Civil Engineering (Structural Engineering) of the São Carlos School of Engineering at the University of São Paulo, as part of the requirements for obtaining the degree of Master in Structural Engineering.

Advisor: Prof. Dr. Ricardo Carrazedo

CORRECTED VERSION

(Original version is available at São Carlos School of Engineering)

São Carlos

2025

Ficha catalográfica elaborada pela Biblioteca Prof. Dr. Sérgio Rodrigues Fontes da EESC/USP com os dados inseridos pelo(a) autor(a).

Moura, Júlia Maria de França
M929d Dynamic-based damage detection in scaled unreinforced masonry panels / Júlia Maria de França Moura; orientador Ricardo Carrazedo. São Carlos, 2025.

Dissertação (Mestrado) - Programa de Pós-Graduação em Engenharia Civil (Engenharia de Estruturas) e Área de Concentração em Estruturas -- Escola de Engenharia de São Carlos da Universidade de São Paulo, 2025.

1. Unreinforced masonry walls. 2. Damage identification. 3. Experimental Modal Analysis. 4. Nondestructive tests. 5. Dynamic characterization. 6. Small-scale models. I. Título.

Eduardo Graziosi Silva - CRB - 8/8907

FOLHA DE JULGAMENTO

Candidata: Bacharel **JÚLIA MARIA DE FRANÇA MOURA**.

Título da dissertação: "Detecção de danos com base na resposta dinâmica em painéis de alvenaria não armada em escala reduzida".

Data da defesa: 05/08/2025.

Comissão Julgadora	**Resultado**
Prof. Associado Ricardo Carrazedo **(Orientador)** (Escola de Engenharia de São Carlos/EESC-USP)	APROVADA
Profa. Dra. Elisa Bertolesi (Cardiff University)	APROVADA
Prof. Dr. Cláudius de Sousa Barbosa (Escola Politécnica/EP-USP)	APROVADA

Coordenador do Programa de Pós-Graduação em Engenharia Civil (Engenharia de Estruturas):
Prof Associado **Ricardo Carrazedo**

Presidente da Comissão de Pós-Graduação:
Prof. Titular **Carlos De Marqui Junior**

To my grandmother Joselita (in memoriam)

ACKNOWLEDGEMENTS

I would like to thank my parents, Fábio and Karla, and my sister, Luísa, for their love, support, and trust. They are the reason behind everything I do. I am also deeply grateful to my grandparents, Maria José and Ítalo, for their affection and especially for the invaluable help they gave me during my first months in São Carlos.

To João, my partner, for always making me smile and for standing tirelessly by my side through both good and hard times.

I acknowledge my advisor, Ricardo Carrazedo, for sharing his expertise and for the trust and opportunities he consistently offered throughout this journey.

To Professor Vladimir Haach, I am thankful for his patience, suggestions, and readiness to answer all my questions about masonry and shear testing.

My thanks also go to Amaury, Fabiano, Romeu, and Luiz Vareda for their assistance, companionship, and support during my tests at the Structures Laboratory.

To my lab friends, Paulo and Thássia, for always being willing to help and for creating a lighter, more enjoyable work environment.

I am grateful to the friends who were true gifts over these years: Larissa, Camila, Talita, Geraldo, Rodrigo, and Denisson. From day one, they made me feel at home.

Finally, I acknowledge the financial support provided by CNPq, which partially funded this research, as well as the enterprise Cerâmica City for kindly providing the clay blocks used in this study.

ABSTRACT

MOURA, J. M. F. **Dynamic-based damage detection in scaled unreinforced masonry panels**. 2025. M.Sc. Thesis - Escola de Engenharia de São Carlos, Universidade de São Paulo, São Carlos, 2025.

The dynamic behavior of structures has become increasingly relevant in the assessment of structural performance, particularly in light of extreme events such as earthquakes and blasts. In this context, vibration-based methods have emerged as effective tools for non-destructive evaluation, especially when applied to structural health monitoring (SHM). Modal parameters—such as natural frequencies, mode shapes, and damping ratios—are sensitive to changes in stiffness and have proven useful in identifying damage and monitoring degradation over time. Unreinforced masonry (URM) walls, are especially vulnerable to shear-induced cracking, which can substantially affect their dynamic response. Despite their prevalence, the dynamic behavior of URM infill walls under progressive damage remains underexplored, particularly with regard to the influence of construction variables and in-plane degradation. This study investigates the dynamic response of scaled load-bearing unreinforced masonry wall models under cyclic in-plane loading. Experimental tests were conducted on panels built with different materials and geometries, and their modal parameters were recorded before and after damage using ambient vibration testing. The results are complemented by numerical modeling to validate mode identification and guide sensor placement. Damage progression is analyzed through variations in modal properties and assessed using dynamic-based identification techniques. The findings confirm the progressive reduction of natural frequencies with increasing damage and demonstrate the effectiveness of dynamic parameters, along with MAC and COMAC coefficients, for damage detection. Overall, the adopted methodology highlights the potential of vibration-based techniques as practical tools for the monitoring of masonry structures.

Keywords: Unreinforced masonry walls. Damage identification. Experimental Modal Analysis. Nondestructive tests. Dynamic characterization. Small-scale models.

RESUMO

MOURA, J. M. F. **Detecção de danos com base na resposta dinâmica em painéis de alvenaria não armada em escala reduzida**. 2025. Dissertação (Mestrado) - Escola de Engenharia de São Carlos, Universidade de São Paulo, São Carlos, 2025.

O comportamento dinâmico das estruturas tem se tornado cada vez mais relevante na avaliação do desempenho estrutural, especialmente diante de eventos extremos como terremotos e explosões. Nesse contexto, métodos baseados em vibração têm se consolidado como ferramentas eficazes para avaliações não destrutivas, especialmente quando aplicados ao monitoramento da integridade estrutural (em inglês, SHM). Parâmetros modais — como frequências naturais, formas modais e coeficientes de amortecimento — são sensíveis a variações na rigidez e têm se mostrado úteis na identificação de danos e no acompanhamento da degradação ao longo do tempo. Paredes de alvenaria não armada são particularmente vulneráveis a fissuração por esforços cortantes, o que pode afetar substancialmente sua resposta dinâmica. Apesar de sua ampla utilização, o comportamento dinâmico desses painéis de alvenaria sob danos progressivos ainda é pouco explorado, especialmente no que diz respeito à influência de variáveis construtivas e à degradação no plano. Este estudo investiga a resposta dinâmica de modelos em escala de paredes de alvenaria estrutural não armada submetidos a carregamentos cíclicos no plano. Ensaios experimentais foram realizados em painéis construídos com diferentes materiais e geometrias, e seus parâmetros modais foram registrados antes e após os danos por meio de testes de vibração ambiente. Os resultados são complementados por modelagem numérica, empregada para validar a identificação dos modos e orientar o posicionamento dos sensores. A progressão dos danos é analisada a partir das variações nos parâmetros modais e avaliada por meio de técnicas de identificação baseadas em propriedades dinâmicas. Os resultados confirmam a redução progressiva das frequências naturais com o aumento dos danos e demonstram a eficácia dos parâmetros modais, juntamente com os coeficientes MAC e COMAC, na detecção de danos. De forma geral, a metodologia adotada evidencia o potencial das técnicas baseadas em vibração como ferramentas práticas para o monitoramento de estruturas de alvenaria.

Palavras-chave: Paredes de alvenaria não armada. Identificação de Danos. Análise dinâmica experimental. Ensaios não destrutivos. Caracterização dinâmica. Modelos reduzidos.

LIST OF FIGURES

LIST OF TABLES

LIST OF FRAMES

CONTENTS

1 INTRODUCTION

The dynamic behavior of structures plays an increasingly important role in the assessment of their safety and performance, especially considering the growing frequency and intensity of extreme events such as heavy rainfall, rising sea levels, hurricanes, and earthquakes (Orcesi *et al.*, 2022). In this context, techniques based on modal analysis have become widely used as non-destructive methods for evaluating structural systems. The modal parameters obtained from dynamic tests—such as natural frequencies, mode shapes, and damping ratios—not only provide insights into the global behavior of structures but also serve as a basis for structural health monitoring (Bernat-Masó; Gil, 2019).

The effects of damage on structures can be evaluated by comparing their dynamic properties over time, for instance, before and after seismic events (Hamid; Schuller, 2019). In this approach, even subtle damage can be identified by shifts in frequency or changes in modal shapes, making modal analysis a valuable technique not only for calibration of numerical models (Ceravolo *et al.*, 2016) but also for long-term performance monitoring.

Dynamic-based damage identification is a particularly attractive tool for masonry structures, as damage in these systems is typically associated with reductions in stiffness. In masonry, such damage primarily manifests as cracking, material deterioration, or excessive deformation. When cracks occur, they are often localized and tend to divide the structure into macro-blocks (Ramos *et al.*, 2010). Unreinforced masonry walls are notable for their widespread use and variety of forms. They may function as freestanding walls, load-bearing elements, or as infill panels within reinforced concrete frames. The latter configuration is common in concrete-framed structures across South America and Europe. Although infill panels are often classified as non-structural, depending on how they are connected to the surrounding frame, they can act as diagonal bracing, supporting lateral loads and significantly affecting the stiffness and strength of the structure (Alva; Montandon, 2019). Despite their potential impact, the influence of infill masonry is frequently neglected in the design of new buildings and in the evaluation of existing ones (Šipoš; Rodrigues; Grubišić, 2018), which can lead to inaccurate predictions of dynamic behavior due to the associated changes in mass and stiffness.

Additionally, the importance of considering infill walls has grown in the study of progressive collapse. Catastrophic events such as the collapse of the World Trade Center (2001) and the Wilton Paes de Almeida Building (2018) have emphasized how secondary structural elements can influence the failure mechanism of framed structures (Shan *et al.*, 2019). Infill walls may provide additional redundancy and energy dissipation, mitigating the effects of extreme actions and contributing to the overall structural response. Despite this, few studies have focused on the dynamic response and modal damage signatures of

URM walls as infilled masonry—particularly considering in-plane behavior and progressive damage processes. This gap is highlighted in recent reviews such as that by Nicoletti *et al.* (2022).

In this context, given the high variability to which masonry walls are susceptible – related to the materials and geometry of the units, mortar composition, boundary conditions and slenderness of the panel – it becomes necessary to evaluate the influence of different variables and, additionally, the damage process of the structure on its dynamic performance.

To address these issues, the present study focuses on the dynamic behavior and damage assessment of load-bearing unreinforced masonry walls, with particular attention to shear-related damage. Reduced-scale physical models were employed to evaluate the in-plane cyclic response and to monitor changes in modal properties throughout the damage progression. The study of structural system behavior using reduced models has been an important tool in civil engineering and is commonly employed in research with satisfactory results (Harris; Sabnis, 1999; Nascimento Neto, 2003). Several studies conducted in Brazil (Capuzzo Neto, 2015; Maurício, 2005; Moreira, 2007; Nascimento Neto, 2003; Silva, 2014) using reduced models of concrete or clay block masonry (scales between 1:3 and 1:5) have demonstrated the feasibility of their use.

On this context, Komur, Kara and Deneme (2020) analyzed 1:3 scaled three-story infilled frames to study the impact of different infill configurations on in-plane modal behavior. Dönmez and Çankaya (2013) also worked with 1:5 scaled models of reinforced concrete frames with and without masonry panels, where natural frequencies and mode shapes were obtained at different damage levels to correlate modal variation with structural degradation. Although the authors did not adopt specific damage detection tools, the changes in modal response were indicative of damage evolution.

Focusing explicitly on damage detection through dynamic parameters, Ramos *et al.* (2006) correlated modal properties with progressive damage in masonry arches and walls under controlled loading. Using ambient vibration tests, the study applied the Damage Index and Direct Stiffness Calculation to detect and quantify damage in accordance with Rytter's classification levels. Additional contributions by Oyarzo-Vera and Chouw (2017) and Anwar and Elwaly (2023) further explored the use of modal-based indices to detect artificially induced damage in masonry walls.

In this research, load-bearing masonry wall models will be constructed using different materials and geometries. Their dynamic properties will be captured in both undamaged conditions and after damage induced by in-plane shear testing. The collected data will be processed using dynamic-based damage identification techniques. This approach aims to enhance the understanding of how damage influences the dynamic performance of URM walls and contributes to the development of practical tools for the structural health

monitoring of masonry elements in real-world applications.

1.1 Objectives

The overall objective of this study is to analyze the dynamic behavior of unreinforced masonry walls subjected to progressive damage and to assess the influence of this degradation, along with parameters such as the material and geometry of the masonry units and the level of pre-compression, on the modal response of the structure. To address this main objective, the study defines the following specific objectives:

- Characterize the mechanical and dynamic properties elements of masonry by conducting tests on clay and concrete units, mortar and masonry prisms, in accordance with applicable standards.
- Develop numerical models of masonry walls to predict and analyze vibration modes and natural frequencies.
- Implement and conduct ambient vibration tests on reduced-scale masonry panel models constructed in the Structures Laboratory (LE-SET), considering different block materials and geometries, in order to obtain in-plane and out-of-plane natural frequencies and mode shapes.
- Introduce controlled progressive damage into the experimental models and assess its effects on modal parameters.
- Apply damage identification techniques based on the modal analysis data.

1.2 Significance

In recent years, the demand for reliable and efficient methods to assess structural safety has grown significantly, particularly in the face of extreme events and aging infrastructure. Among these methods, dynamic-based damage identification and structural health monitoring have emerged as powerful tools for evaluating changes in structural performance. These techniques rely on the analysis of modal properties—such as natural frequencies and vibration modes—which are sensitive to stiffness degradation, cracking, and other forms of structural damage.

Unreinforced masonry walls, widely used in various structural systems including load-bearing elements and infill panels in reinforced concrete frames, are especially suited to this type of analysis. Damage in masonry typically manifests as localized cracking, which can substantially affect the wall's dynamic behavior. Despite their prevalence and potential to influence the global response of a structure, URM walls remain underexplored in the

context of vibration-based damage detection, particularly when it comes to understanding how different construction variables and damage mechanisms affect their modal response.

Therefore, this research is motivated by the need to deepen the understanding of the dynamic behavior of masonry walls under progressive damage and to explore their potential for integration into SHM frameworks. By investigating the evolution of modal parameters in small-scale masonry panels subjected to in-plane shear damage, this work aims to contribute to the development of efficient and non-destructive techniques for monitoring the structural condition of masonry elements.

1.3 Methodology

The main information regarding the proposed procedures and the experimental campaign of this research are summarized in the following topics.

1. **Literature review:** This stage consists of an in-depth review of the available literature to improve the understanding of key concepts related to experimental modal analysis, numerical modeling techniques best suited for masonry, and methodologies for detecting structural damage through dynamic properties.

2. **Characterization of employed materials:** This phase involves conducting a series of tests to characterize the materials used and determine the mechanical properties of the masonry components.

3. **Development of numerical models:** Numerical models will be developed using the finite element software ABAQUS to simulate structural behavior and estimate the expected dynamic characteristics. These models will also provide guidance for the optimal placement of accelerometers in the experimental setup.

4. **Fabrication of small-scale models:** Scaled models of masonry panels will be constructed, ensuring that the relationship between the model and the prototype satisfies the required similitude conditions.

5. **Dynamic tests on masonry panels:** Modal identification tests will be conducted on undamaged models to characterize their initial dynamic behavior. Subsequently, the models will be progressively damaged, and vibration measurements will be repeated after each stage to evaluate the effects of damage on the dynamic response.

6. **Digital processing of experimental data:** The modal parameters—such as natural frequencies, vibration modes, and damping ratios—will be obtained through digital signal processing using computational routines.

7. **Analysis and correlation of the results obtained:** This final stage involves identifying damage using computational procedures and analyzing the influence of

the tested variables, with the goal of characterizing the dynamic behavior of masonry walls.

2 EXPERIMENTAL MODAL ANALYSIS

Modal analysis is an important and reliable method in the analysis of structural behavior, and it is used in various applications like troubleshooting, damage detection and quantification, validation of FE model, load estimation, structural dynamic modification and Structural Health Monitoring (Zahid *et al.*, 2023). Its definition consists of describing the structure in terms of its natural characteristics, namely frequency, damping, and vibration modes (Avitabile, 2001). These parameters can be defined by theoretical or experimental methods. Theoretical methods start from the spatial description of the study structure, often using the Finite Element Method; Besides, experimental methods start from the measurement of dynamic responses obtained in vibration tests. This approach is also crucial for verifying and validating the results obtained by numerical models (Nóbrega, 2005). Figure 1 illustrates the possible paths for vibration analysis in a structural system.

Figure 1 – Modal analysis routes

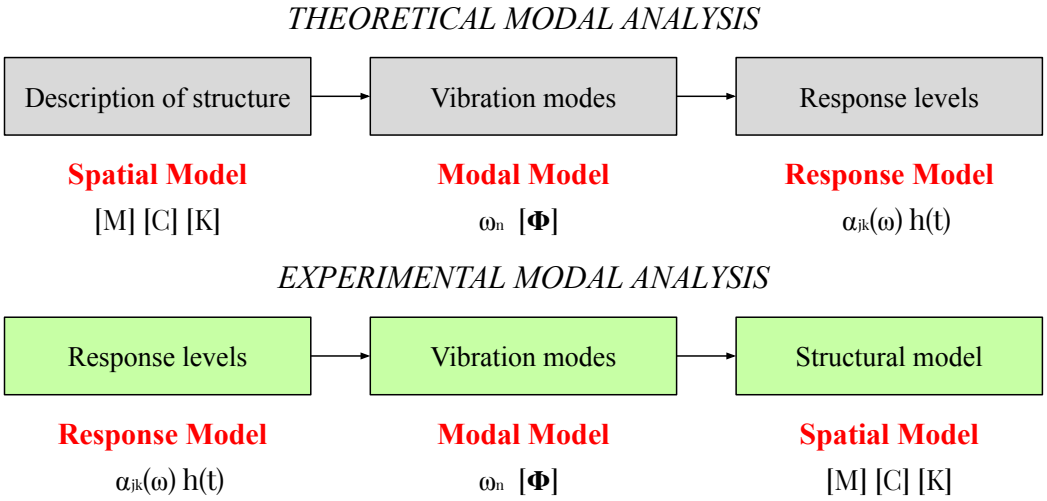

Source: Adapted from Ewins (1984)

This chapter introduces, therefore, the theme of Modal Analysis, presenting its theoretical foundation, experimental methods, equipments, damage identification based on dynamic characteristics and finally, the dynamic models on small scale.

2.1 Fundamental concepts of structural dynamics

When a structure is disturbed, being displaced from its static equilibrium position and allowed to oscillate without any external excitation, it will vibrate at certain frequencies: its natural frequencies. A structure has an unlimited number of natural frequencies, and for each of these frequencies, there is an associated unique deformed shape of the structure, referred to as a mode shape (Johansson, 2009).

In structural dynamics, determining the response of a system is achieved through mathematical models consisting of systems of differential equations in which time plays a fundamental role (Brasil; Silva, 2015). The dynamic behavior of a linear, discretized structural system with N degrees of freedom, subjected to external forces $p(t)$, can be expressed by the following matrix equation 2.1:

$$[M]\{\ddot{u}\} + [C]\{\dot{u}\} + [K]\{u\} = \{p(t)\} \tag{2.1}$$

where $[M]$, $[C]$ e $[K]$: are the mass, viscous damping, and stiffness matrices of the system, respectively $(n \times n)$;
$\{p(t)\}$: it is the vector of external forces $(n \times 1)$;
$\{\ddot{u}\}, \{\dot{u}\}$ e $\{u\}$: are the acceleration vector, the velocity vector and the displacement vector, respectively $(n \times 1)$.

When damping is neglected and there is no consideration of external force acting on the system ($\{p(t)\} = \{0\}$), the free undamped or conservative response is observed, where the modal properties are obtained. In this scenario, Eq. 2.1 assumes the following form:

$$[M]\{\ddot{u}\} + [K]\{u\} = \{0\} \tag{2.2}$$

In solving this ordinary differential equation, the approach adopted is $\{u\} = \{\phi\}\, e^{st}$. Here, $\{\phi\}$ is a vector of real elements and s is complex. Substituting this solution into the differential equation and making the variable change $s^2 = -\lambda$ conveniently, yields the key equation for the solution process:

$$[[K] - \lambda [M]]\{\phi\} = \{0\} \tag{2.3}$$

Therefore, the free response of the system can be reduced to an eigenvalue-eigenvector determination problem. Each eigenvector $\{\phi\}_n$ is termed a modal vector or simply a normal mode of vibration, and the eigenvalues λ_n are equal to the square of the undamped natural frequencies ω_n^2 of the system. For a system with N degrees of freedom, the modal model becomes:

$$[\omega_n] = \begin{bmatrix} \omega_1 & 0 & \cdots & 0 \\ 0 & \omega_2 & \cdots & 0 \\ \vdots & \vdots & \ddots & \vdots \\ 0 & 0 & \cdots & \omega_n \end{bmatrix} \tag{2.4}$$

$$\Phi = \begin{bmatrix} \phi_1 & \phi_2 & \cdots & \phi_n \end{bmatrix} = \begin{bmatrix} \phi_{11} & \phi_{12} & \cdots & \phi_{1n} \\ \phi_{21} & \phi_{22} & \cdots & \phi_{2n} \\ \vdots & \vdots & \ddots & \vdots \\ \phi_{n1} & \phi_{n2} & \cdots & \phi_{nn} \end{bmatrix} \tag{2.5}$$

The square matrix that assimilates the column vectors of the vibration mode values is termed the modal matrix (Soriano, 2014). The vibration mode $\phi_{\mathbf{n}}$ corresponds to the natural frequency ω_n and has elements ϕ_{jn}, where the index j indicates the degree of freedom.

These mode shape vectors are linearly independent and have orthogonal relations relative to the elastic properties of the system, which are described by Eq. 2.6 and 2.7.

$$\{\phi\}_s^T [M] \{\phi\}_r = 0 \tag{2.6}$$

$$\{\phi\}_s^T [K] \{\phi\}_r = 0 \tag{2.7}$$

When the indices refer to the same mode ($\omega_r = \omega_s$), the result of the matrix operation is no longer zero, yielding the following self-orthogonality expressions:

$$\{\phi\}_r^T [M] \{\phi\}_r = M_r \tag{2.8}$$

$$\{\phi\}_r^T [K] \{\phi\}_r = K_r \tag{2.9}$$

Where M_r and K_r are known as modal or generalized mass and stiffness, respectively. Those expressions could be written considering all the possible combinations of r and s as follows:

$$[\Phi]^T [M] [\Phi] = \begin{bmatrix} M_1 & 0 & \cdots & 0 \\ 0 & M_2 & \cdots & 0 \\ \vdots & \vdots & \ddots & \vdots \\ 0 & 0 & \cdots & M_n \end{bmatrix} \tag{2.10}$$

$$[\Phi]^T [K] [\Phi] = \begin{bmatrix} K_1 & 0 & \cdots & 0 \\ 0 & K_2 & \cdots & 0 \\ \vdots & \vdots & \ddots & \vdots \\ 0 & 0 & \cdots & K_n \end{bmatrix} \tag{2.11}$$

Once the mode shapes are known within an indeterminate scaling factor it's also possible mass-normalize by the matrix $[\Phi]_m$ which is composed by the normalized eigenvalues ($\{\phi_{m,i}\} = \{\phi_i\} / \sqrt{m_i}$), leading to the relations shown in Eq. 2.12 and 2.13.

$$[\Phi]_m^T [M] [\Phi]_m = [I] \tag{2.12}$$

$$[\Phi]_m^T [K] [\Phi]_m = \left[\omega^2\right] \tag{2.13}$$

Where $[I]$ denotes the identity matrix and $[\Phi]_m$ is the mass-normalized modal matrix. These properties are essential for deriving the free vibration solution of Eq. 2.2. Before

proceeding, however, it is necessary to define the coordinate transformation introduced in Eq. 2.14.

$$\{u(t)\} = \sum_{i=1}^{N} \{\phi_i\}\, \eta_i(t) \quad \text{or} \quad \{u\} = [\Phi]\, \{\eta\} \tag{2.14}$$

This formulation is based on the principle of mode superposition, in which the total displacement vector is expressed as a linear combination of the system's eigenvectors. The vector $\{\eta\}$ denotes the modal (or normal) coordinates (Clough; Penzien, 2003). Through this coordinate transformation, the physical displacement vector $u(t)$ is replaced by $\eta(t)$, allowing the equations of motion to be reformulated in modal space. Substituting this into Eq. 2.2 and performing the appropriate mathematical operations, the system reduces to Eq. 2.15, which consists of N uncoupled single degree-of-freedom (SDOF) equations. This decoupled form significantly simplifies the solution for the free vibration problem.

$$\{\ddot{\eta}\} + \left[\omega^2\right] \{\eta\} = \{0\} \tag{2.15}$$

Returning to Eq. 2.1, now including viscous damping and considering a non-zero excitation force represented by $\{f_0\}\, e^{i\omega t}$ – with ω denoting the harmonic excitation frequency and $\{f_0\}$ the amplitude vector – the same coordinate transformation defined in Eq. 2.14 is applied. By pre-multiplying the resulting equation by $[\Phi]^T$, the following expression is obtained:

$$[\Phi]^T [M] [\Phi] \{\ddot{\eta}\} + [\Phi]^T [C] [\Phi] \{\dot{\eta}\} + [\Phi]^T [K] [\Phi] \{\eta\} = [\Phi]^T \{f_0\}\, e^{i\omega t} \tag{2.16}$$

The same orthogonality relationship derived from the undamped modal model—which diagonalizes the mass and stiffness matrices—can also diagonalize the damping matrix if, and only if, the damping is a linear combination of the mass and stiffness matrices. This condition is known as proportional damping, and it is expressed by Eq. 2.17.

$$[C] = a_0 [K] + a_1 [M] \tag{2.17}$$

Here, a_0 and a_1 are scalar constants defining the proportional damping model. By applying the orthogonality properties, the equations of motion can be decoupled into the following form:

$$[M_r] \{\ddot{\eta}\} + [C_r] \{\dot{\eta}\} + [K_r] \{\eta\} = \{\mu\}\, e^{i\omega t} \tag{2.18}$$

For the r-th vibration mode, this reduces to:

$$\ddot{\eta}_r + 2\xi_r \omega_r \dot{\eta}_r + \omega_r^2 \eta_r = \mu_r e^{i\omega t} \tag{2.19}$$

In this equation, the terms correspond to the modal parameters associated with mode r, defined as follows:

$$\xi_r = \frac{c_r}{2\sqrt{k_r m_r}} \qquad \text{modal damping ratio}$$

$$\omega_r = \sqrt{\frac{k_r}{m_r}} \qquad \text{undamped natural frequency}$$

$$\mu_r = \frac{1}{m_r}\{\phi\}_r^T\{f_0\} \qquad \text{modal excitation force}$$

The solution for the Eq. 2.19 may be expressed by:

$$\eta_r(t) = Q_r e^{i\omega t} \tag{2.20}$$

And the solution in terms of physical coordinates is given using the concept of mode superposition, that is:

$$\{u(t)\} = \sum_{r=1}^{N} \frac{\{\phi\}_r\{\phi\}_r^T\{f_0\}}{m_r\left(\omega_r^2 - \omega^2 + i\,2\zeta_r\omega_r\omega\right)} e^{i\omega t} \tag{2.21}$$

From this expression, the Frequency Response Function (FRF) matrix of the system can be derived – an essential concept in modal analysis. Denoted by $H(\omega)$, this complex frequency-dependent function relates the system's input to its output. When the output response is expressed in terms of displacement, the FRF is specifically referred to as the Receptance, which is given by Eq. 2.22.

$$[H(\omega)] = \sum_{r=1}^{N} \frac{\{\phi\}_r\{\phi\}_r^T}{m_r\left(\omega_r^2 - \omega^2 + i\,2\xi_r\omega_r\omega\right)} \tag{2.22}$$

Each element $H_{ij}(\omega)$ of the FRF matrix $(N \times N)$ is defined as:

$$H_{ij}(\omega) = \frac{U_i}{F_j}(\omega) \tag{2.23}$$

Where $U_i(\omega)$ denotes the displacement response at coordinate i, and $F_j(\omega)$ represents the force applied at coordinate j, both expressed in the frequency domain. It is also important to note that the FRF satisfies the principle of reciprocity, meaning that $H_{ij}(\omega) = H_{ji}(\omega)$ for $i \neq j$.

Although damping is typically non-proportional, when it is small, the off-diagonal terms of the damping matrix can often be neglected without a significant loss of accuracy. When non-proportional damping is accounted for, modal analysis leads to complex mode shapes and natural frequencies (Silva; Maia, 1999). In structural systems, damping represents the dissipation of mechanical energy – usually into thermal energy – and causes a gradual decay in vibration amplitude, even in conservative responses (Bachmann *et al.*,

1995). The estimation of structural damping is influenced by numerous factors, making the determination of accurate values challenging. As a result, modal damping ratios are frequently estimated based on data from similar structures or, when possible, through direct experimental measurements (Marcos, 2015; Chopra, 2020).

2.2 Experimental modal identification

In section 2.1, the process of deriving a structure's natural characteristics was briefly outlined by discretizing it into matrices and vectors corresponding to its mechanical properties. In the experimental approach, structures can be described using functions that characterize their response.

The success in obtaining these response data is intrinsically linked to the accurate assessment of errors and the quality of the preceding steps leading to the determination of modal parameters (Nóbrega, 2005). ALLEMANG and BROWN (2002) summarize these steps as: theory of Modal Analysis, methods of Experimental Modal Analysis, data acquisition, estimation of modal parameters, and finally, presentation and validation of the obtained properties. In this context, the following topics will delve into the main stages of this process and the possible methods to execute them: data acquisition and modal identification.

2.2.1 Data acquisition equipment

In experimental structural analysis, obtaining accurate and representative results requires the use of measurement devices capable of capturing the relevant physical quantities. In this context, transducers are widely employed, as they are specifically designed to convert a physical phenomenon being measured into an electrical signal (Bendat; Piersol, 2011). The dynamic response of structures can be assessed in terms of displacement, velocity, or acceleration. For low-frequency systems, such as civil engineering structures, displacement and velocity transducers are often suitable, whereas acceleration transducers are typically preferred for high-frequency applications. However, However, even in low-frequency scenarios, displacement measurement devices can be bulky and more expensive, making accelerometers a more practical and commonly adopted choice (Caetano, 1992; Ramos, 2007).

Two additional categories of equipment essential to experimental structural analysis are excitation systems and data acquisition systems. The selection and application of excitation mechanisms are directly influenced by the specific modal analysis technique adopted, as discussed in detail in Section 2.2.3. This decision depends on whether both the input excitation forces and the structural responses will be measured, or whether only the responses will be recorded. The main characteristics and considerations associated with these components are addressed in the following sections.

2.2.1.1 Excitation devices

Excitation mechanisms are employed to induce a response in a mechanical system through the application of controlled forces. These forces can be generated using a variety of devices, including shakers (Figure 2a), impulse hammers (Figure 2b), and eccentric rotating mass vibrators (Figure 2c).

Figure 2 – Examples of excitation equipments

(a) Electrodynamic shaker (BKSV, 2019)

(b) Impulse hammer (BKSV, 2012)

(c) Eccentric mass vibrator (Rodrigues, 2004)

The selection of an appropriate excitation device depends on factors such as the size of the structure under investigation and the desired excitation waveform. For small- to medium-sized structures, excitation is typically performed using impact hammers or electrodynamic shakers. The latter can apply a wide range of input signals, while impact hammers are primarily used for transient response analysis. In contrast, large-scale civil engineering structures—such as bridges or dams—require more robust equipment, such as eccentric mass vibrators or servo-hydraulic shakers (Cunha; Caetano, 2006).

2.2.1.2 Accelerometers

Among the various types of sensors used to assess the dynamic response of structures, accelerometers are the most commonly employed. Several types are available—such as piezoelectric, piezoresistive, capacitive, and force-balance accelerometers. However, this section focuses specifically on piezoelectric accelerometers and their key performance parameters.

Piezoelectric sensors take advantage of the piezoelectric property of materials such as quartz or polycrystalline ceramics, which causes ions to accumulate on opposite surfaces of the crystal when a force is applied, producing an electrical output signal proportional to the acceleration (Ramos, 2007). These sensors are typically modeled as SDOF spring–mass–damper systems, where the seismic mass is mechanically coupled to the piezoelectric element, which provides both the elastic (spring) and damping behavior of the system. Consequently, several performance characteristics of piezoelectric accelerometers

can be derived from the analysis of the FRF, which relates the input acceleration to the resulting output voltage (Rainieri; Fabbrocino, 2014).

There are different design configurations for this type of accelerometer, depending on how the electrical charge is induced in the piezoelectric crystal—either through compression, shear, or flexural deformation. The typical structures of compression-type and shear-type accelerometers are illustrated in Figure 3.

Figure 3 – Different types of piezoeletric accelerometers

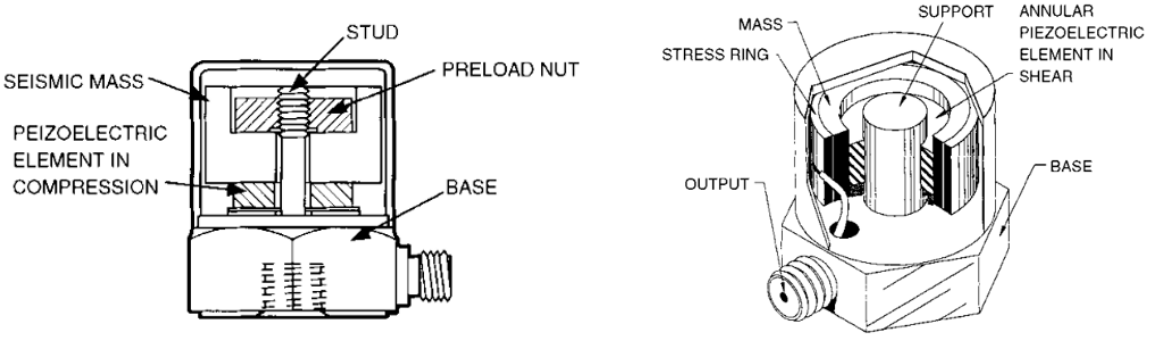

(a) Compression piezoelectric accelerometer (b) Annular shear accelerometer

Source: Harris and Piersol (2002)

Piezoelectric accelerometers offer advantages such as self-generation of signals without external power, high stability, good signal-to-noise ratio, and linear response across wide frequency and dynamic ranges (Ramos, 2007). Besides these characteristics, other parameters should be taken into account in order to properly select them for a specific application, such as ambient vibration testing which usually presents low amplitude of motion and limited frequency range.

The first important specification is the *sensitivity* of the sensor, sometimes referred as "scale factor". That is, the ratio of its electrical output to it mechanical input, that is, the minimum input of physical parameter that will create a detectable output change (Rainieri; Fabbrocino, 2014). Sensitivity is expressed in terms of charge per unit acceleration (e.g. $\mathrm{pC/ms^{-2}}$) or in terms of voltage per unit acceleration (e.g., $\mathrm{mV/ms^{-2}}$).

Sensor *resolution* refers to the smallest mechanical input variation that produces a detectable change in output, expressed either in absolute terms or as a percentage of the full-scale range. The *frequency response* characterizes how the sensitivity may deviate from its reference value across the specified frequency range. The *transverse sensitivity*, also known as "cross-axis sensitivity", indicates the sensor's response to motion perpendicular to its primary axis. Typically expressed as a percentage of the axial sensitivity, it is usually around 2% or lower in accelerometers for modal testing (Mayo, 2022; Rainieri; Fabbrocino, 2014). Other key specifications include the *dynamic range*, which expresses the ratio between the largest and smallest measurable signals (commonly given in decibels) and

the *self-noise*, which can be a determining factor for accurately capturing the structural response.

2.2.1.3 Data aquisition systems

A data acquisition system (DAQ) is responsible for recording the excitation and response signals and converting them into a digital form that can be manipulated by a computer and analyzed by software. The basic elements of a DAQ system include the transducers, a data acquisition hardware with multiple channels and signal conditioning circuitry that provide the interface between the external sensors and the analog-to-digital converters (ADC), and a controller, which is usually a computer with dedicated data acquisition software (Potter; Eren, 2012).

Since sensors often produce noisy electrical signals that cannot be directly processed, it is essential to use signal-conditioning circuitry to convert the raw output into conditioned signals suitable for digitization and acquisition. In general, the functions of a signal conditioner include amplification, isolation, filtering, sensor excitation (for passive transducers), linearization, and other sensor-specific adjustments (Potter; Eren, 2012; Ramos, 2007).

Among the various functions of signal conditioning, two particularly important ones are amplification and anti-aliasing. Piezoelectric transducers typically generate low-amplitude analog signals that must be amplified before analysis to ensure accurate data acquisition. Amplifiers enhance signal strength, mitigating attenuation and minimizing the impact of external noise. To address this requirement, most piezoelectric accelerometers incorporate simple internal electronic circuits that perform signal amplification directly within the sensor casing (Caetano, 1992; Harris; Piersol, 2002).

Additionally, anti-aliasing filters are essential to prevent information loss by eliminating frequency components above the Nyquist limit prior to digitization. The aliasing phenomenon occurs when a continuous signal is sampled at an insufficient rate, causing frequency components higher than the Nyquist frequency (half the acquisition frequency) to be misrepresented as lower-frequency ones (Rainieri; Fabbrocino, 2014), as illustrated in Figure 4.

To prevent this issue in practice, the signal conditioner applies an analog low-pass filter before the sampler and ADC. This filter allows low-frequency components to pass while attenuating high-frequency components that could otherwise lead to aliasing. The potential for aliasing is also why the Shannon sampling theorem must be followed, which states that the sampling frequency must be at least twice—and preferably slightly higher than—the highest frequency of interest.

To digitize a conditioned signal, ADCs apply two steps: first, the signal is quantized,

Figure 4 – Example of aliasing problem

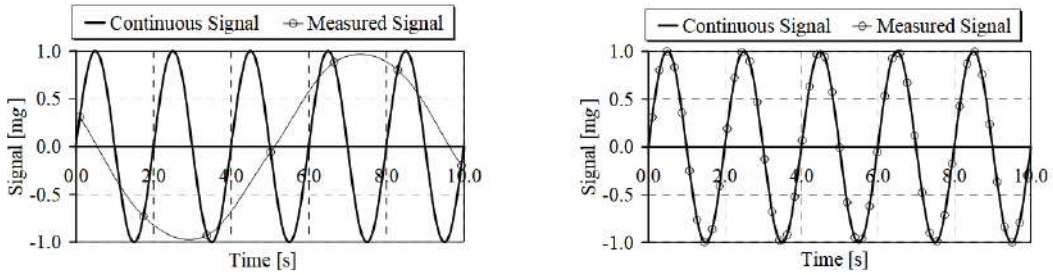

Source: Ramos (2007)

meaning that the continuous values of the analog signal are represented using a set of discrete levels; then, the signal is encoded, that is, represented by bit sequences. The number of bits of an ADC is sometimes also referred to as its resolution. A converter with n-bit capacity can represent 2^n levels of analog signal (Potter; Eren, 2012; Rainieri; Fabbrocino, 2014). Figure 5 summarizes the data acquisition process described above.

Figure 5 – Diagram of data acquisition process

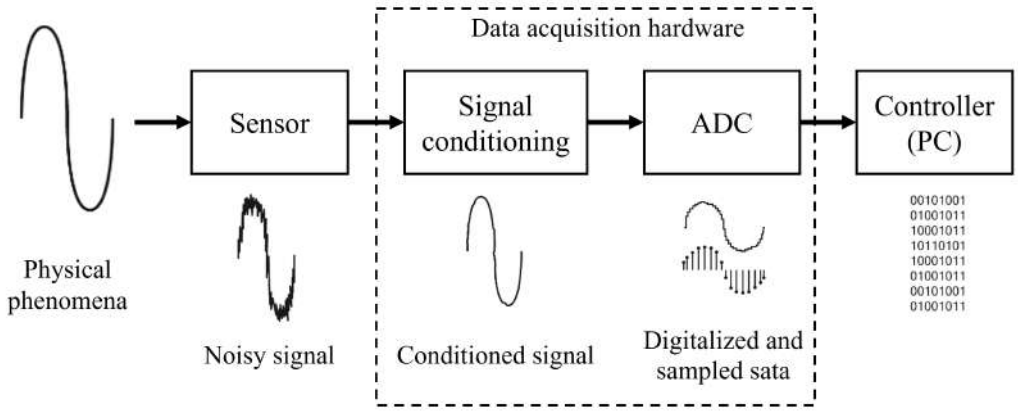

Source: Author (2025)

2.2.2 Frequency analysis of discrete-time signals

In practical applications involving digital signal acquisition and processing, the signal $x(t)$ is sampled at discrete, uniformly spaced time intervals. As a result, both the time and frequency domains are treated in a discrete manner, and the Fourier transform must be reformulated accordingly to account for this discretization (Rainieri; Fabbrocino, 2014).

Analyzing the spectrum of a signal involves decomposing the original time-domain signal into its constituent frequency components. This frequency-domain representation enables the extraction of important characteristics—such as the amplitude spectrum, power spectrum, or power spectral density—that are not readily observable in the time domain alone. To obtain any of these spectral representations from finite, discrete time-domain

data, the first step is to apply the Discrete Fourier Transform (DFT). In practice, the DFT is most efficiently computed using the Fast Fourier Transform (FFT) algorithm. The mathematical expression for the DFT is given by Eq. 2.24:

$$X[k] = \sum_{n=0}^{N-1} x_n \cdot e^{-\frac{i2\pi}{N}kn} \tag{2.24}$$

Where x_n is the discrete time domain signal and the X_k are the Fourier coefficients. This expression operates by multiplying the time-domain signal by a set of sinusoidal basis functions—specifically, complex exponentials of varying frequencies indexed by the variable k. Given Euler's identity $e^{in} = cos(n) + isin(n)$, each component corresponds to a projection of the signal onto a particular frequency. The summation then accumulates these projections to compute the frequency-domain representation. Computationally, this process can be interpreted as the multiplication of a $N \times N$ transformation matrix—composed of complex exponentials – with the $1 \times N$ vector of discrete time-domain samples, resulting in a vector X_n of Fourier coefficients. For signals with large numbers of samples, the Fast Fourier Transform (FFT) algorithm, introduced by Cooley and Tukey (1965), significantly optimizes this computation by exploiting symmetries and redundancies in the transformation matrix, thereby reducing the computational complexity.

The Discrete Fourier Transform yields complex-valued results. These can be interpreted such that the real part of the DFT corresponds to the correlation of the time-domain signal with a cosine function of a given frequency – representing the magnitude component – while the imaginary part corresponds to the correlation with a sine function of the same frequency – associated with the phase component.

The full output of the Fast Fourier Transform spans both positive and negative frequency components, commonly referred to as the two-sided spectrum. The Nyquist frequency represents the upper limit of the positive frequency range and serves as the boundary between positive and negative frequencies. In a one-sided FFT, only the positive frequencies (i.e., one side of the spectrum) are considered, which is often sufficient for real-valued signals.

To properly interpret the frequency content, it is essential to understand the relationship between the sampling parameters. The sampling interval, denoted as Δt, is the inverse of the sampling frequency f_s, which defines the rate at which the continuous-time signal is sampled and converted into a discrete-time representation. Given a finite number N of sampled points, the frequency resolution – also known as the bin width – can be defined as shown in Eq. 2.25:

$$\Delta f = \frac{f_s}{N} \tag{2.25}$$

Consequently, for a fixed sampling frequency, a finer frequency resolution is achieved only by increasing the total duration of the measurement, which implies a larger number

of samples (Rainieri; Fabbrocino, 2014). Assuming that the signal x_n has been sampled at N equally spaced time instants, the obtained discrete signal is given by Eq. 2.26:

$$x_n = x(n\Delta t) \quad \text{with} \quad n = 0, 1, 2, \ldots, N-1 \tag{2.26}$$

The discrete frequency values for the computation of $X[k]$ are given by Eq. 2.27:

$$f_k = \frac{kf_s}{N} \quad \text{with} \quad k = 0, 1, 2, \ldots, N-1 \tag{2.27}$$

2.2.3 Modal analysis techniques

The modal data acquisition of a system is generally done by two methods – which will be developed in this research: Classical Experimental Modal Analysis (EMA) and Operational Modal Analysis (OMA). Recently, a third method has been developed by combining existing techniques: Impact-synchronous Modal Analysis (ISMA). In this method, the structure is artificially excited by controlled forces, similar to what is done in EMA, but the test is performed in the presence of ambient vibrations, as in OMA (Zahid; Ong; Khoo, 2020; Rahman *et al.*, 2014).

Experimental Modal Analysis is a widely used technique for about six decades and therefore, a well-established field with a consistent theoretical foundation (Zahid; Ong; Khoo, 2020; Rainieri; Fabbrocino, 2014). In these tests, both the applied excitation forces and the structure's responses are measured using appropriate transducers. For this purpose, equipment such as shakers, impact hammers, servo-hydraulic or mechanical vibration exciters are used to induce forced vibrations. Figure 6 illustrates the typical setup of an EMA test.

Figure 6 – Generic experimental set-up for EMA

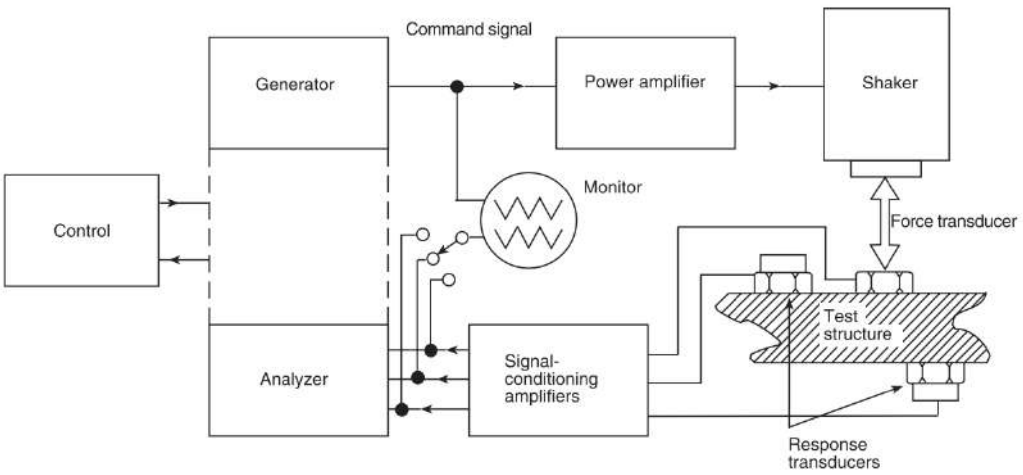

Source: Ewins (2001)

The measurement of system inputs and outputs enables the evaluation of FRFs. During signal processing, the time series obtained in the tests are transformed into the

frequency domain using the Fast Fourier Transform algorithm. With this transformation, FRFs can be defined as complex ratios between the measured responses at different points of the structure and the applied forces, each of these ratios associated with an excitation frequency ω. The structural response outputs can be measured in terms of displacement, velocity, or acceleration, corresponding to the receptance, mobility, and accelerance FRFs, respectively (Rodrigues, 2004; Avitabile, 2001; Døssing; Kjær, 1988).

The measurement of these functions is extremely important for Experimental Modal Analysis. This is because the FRF contains information about the frequency and damping of the system, while a collection of them provides data on the mode shape at the measured locations. By plotting the magnitude (or amplitude) curve of the FRF against frequency, the resulting peaks will indicate the damped natural frequencies, as schematically illustrated in Figure 7.

Figure 7 – Identification of the first frequency from the peak in the magnitude of the Frequency Response Function

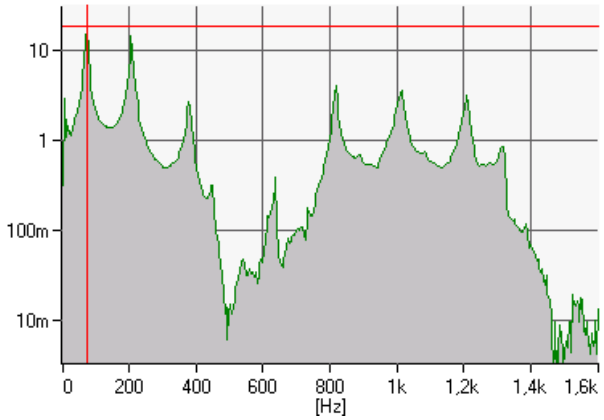

Source: Gade, Herlufsen and Konstantin-Hansen (2002)

Modal damping ratios can also be easily estimated from the slope of the peaks of the FRF. The extraction of mode shapes considers only the imaginary part of the numbers from the acceleration FRF - since accelerometers are the most common sensors in modal analysis tests. By examining the magnitude of the imaginary part of the frequency response function at various points on the structure, it is possible to find the relative modal displacement at each point. Eventually, the coordinate values can be normalized (Nóbrega, 2005). From the graph in Figure 8, it is easy to see that the mode of vibration can be determined by the peaks of the imaginary part for each frequency response function measured at successive points along the structure.

In civil engineering structures, which typically have large dimensions, applying forced vibrations can pose challenges such as disruption of use or the presence of very low-frequency vibration modes that are difficult to identify with existing excitation equipment. In such cases, Operational Modal Analysis (OMA) is an alternative that eliminates the need for force application equipment. As a result, tests are cheaper and faster, and they do

Figure 8 – Identification of the second mode shape of a beam from the imaginary part of the FRF

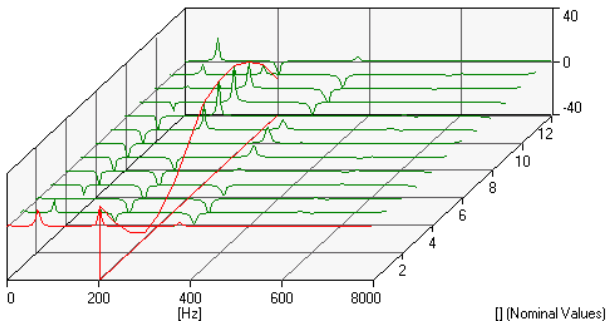

Source: Gade, Herlufsen and Konstantin-Hansen (2002)

not interfere with the normal use of the structure (Rainieri; Fabbrocino, 2014; Rodrigues, 2004).

In this type of modal analysis, only the structure's response to actions resulting from its own usage is measured. For instance, this could include traffic on a viaduct, wind effects on tall buildings, or the audience in gymnasium and stadium bleachers, which represent operational and environmental excitation forces (Juliani, 2014). Since it's impossible to deterministically know the system inputs, assumptions about their characteristics must be made. Therefore, in the general scenario, it's assumed that the structure's excitation forces are a realization of a Gaussian stochastic process of white noise type with a zero mean (Rodrigues, 2004).

However, this is rarely the case as excitation typically has its own spectral distribution. Therefore, it's necessary to interpret the output measurements as resulting from both a virtual system - excited by a white noise process - and the structural system in series (Rainieri; Fabbrocino, 2014; Rodrigues, 2004). Thus, the modal model of the structure is extracted from the combined model. Figure 9 illustrates this concept and distinguishes between the approaches of the experimental modal analysis techniques discussed in this topic.

2.2.4 Modal identification methods

The intermediate stage between measuring system responses and obtaining the Modal Model is the modal identification step. In this stage, the modal parameters of the structures are extracted from the signals obtained in the tests through different methods, which depend on the applied test technique as well as the chosen domain for analysis: time or frequency. Naturally, employing multiple identification modes ensures greater confidence in the results (Masciotta; Ramos, 2019).

The **input-output methods** belong to the field of classical Experimental Modal Analysis, where excitations and responses are measured, enabling identification based

Figure 9 – Diagram of the basic concepts of experimental modal analysis techniques

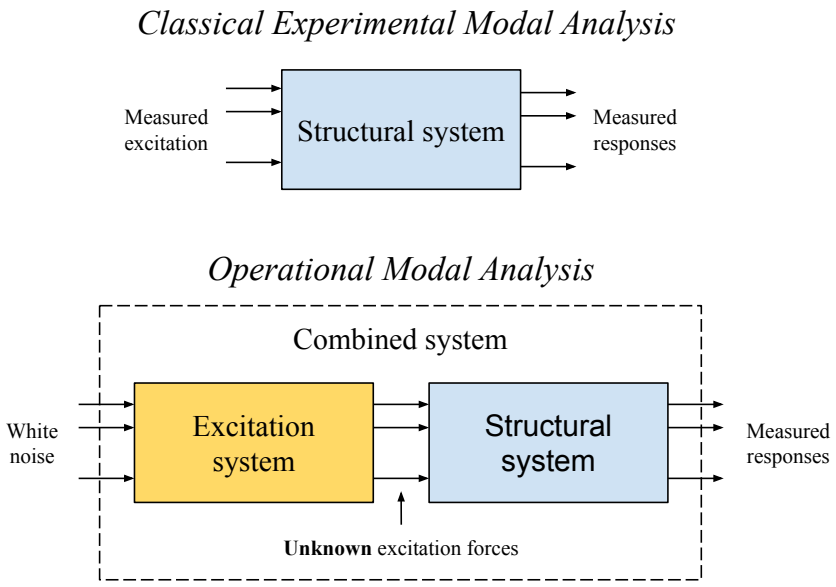

Source: Author (2025)

on Frequency Response Functions (FRFs) or their corresponding functions in the time domain, Impulse Response Functions (IRFs), usually obtained by taking the inverse Fourier transform of the system's FRF data (Rodrigues, 2004; Nóbrega, 2005). According Masciotta and Ramos (2019), since the 1960s, EMA has made significant progress, leading to the development of numerous modal identification algorithms.

From the preceding paragraph, it can be deduced that among the various approaches to extract modal information from a structure, they can be initially categorized into two main groups based on the implementation domain: methods utilizing data in the time domain and those presenting them in the frequency domain. For both domains, there is a subdivision based on the type of dynamic property identified, classifying them as direct or indirect methods. Direct methods estimate the dynamic properties in terms of their mass, stiffness, and damping matrices, thereby obtaining the spatial model immediately. Conversely, indirect methods assess the properties associated with each mode of vibration, such as natural frequency, damping ratio, and modal constant (representative amplitude and phase of modal deformations) (Maia; Silva, 2001).

Furthermore, modal identification can be conducted so that multiple modes are identified simultaneously, characterizing multi-mode identification, also known as multi-degrees-of-freedom (MDOF) methods. Although the vast majority of approaches adopt this strategy, some indirect methods in the frequency domain estimate modal parameters by conducting an analysis where each mode is identified separately, known as mode to mode, or single-degree-of-freedom (SDOF) methods (Varoto, 1991; Maia, 2001).

The final classification pertains to the number of excitation and measurement

points – the system's inputs and outputs. Thus, the methods are divided into single-input/single-output (SISO) techniques, single-input/multiple-output (SIMO) techniques, and multiple-input/multiple-output (MIMO) techniques. Figure 10 illustrates the classifications discussed for modal identification in Experimental Modal Analysis.

Figure 10 – Classification of methods for input-output modal identification

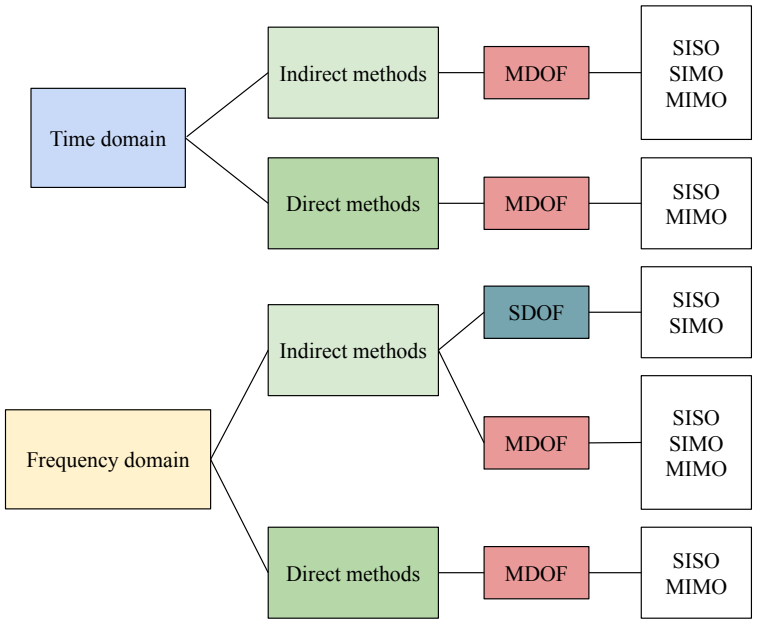

Source: Adapted from Maia (2001)

The early developed methods were fundamentally performed in the frequency domain and classified as mode to mode identification algorithms. One of the most popular in this context is the Circle-Fitting Method (also known as the Kennedy–Pancu Method). The concept of this method is to consider the receptance FRF values near resonance as a circle in the Nyquist plot (Zrayka; Mucchi, 2019) – imaginary part versus real part. Other formulations in the frequency domain can be mentioned, ranging from simpler single-degree-of-freedom methods like Peak Picking and the Inverse Method to more complex multi-mode formulations such as the Rational Fraction Polynomial, Complex Exponential Frequency Domain, and Polyreference Frequency Domain (Masciotta; Ramos, 2019).

Operating in the frequency domain, however, introduces the potential for errors stemming from the applied data transformation, such as leakage, truncation, frequency resolution, and handling lengthy time records. An alternative approach involves utilizing identification methods in the time domain (Ibrahim, 1999). Widely acknowledged are the Complex Exponential Method, a SISO type, and the Ibrahim Time Domain Method, a SIMO type that employs free acceleration responses instead of IRFs (Maia; Silva, 2001).

Considering the options presented, it's worth noting that the selection of the method hinges mainly on the available time and resources, the study's objectives, and the user's personal expertise (Maia, 1999).

The modal identification methods capable of estimating a structure's natural parameters from unknown ambient excitations are referred to as **Input-only techniques**, falling within the realm of Operational Modal Analysis (Masciotta; Ramos, 2019). These approaches are fundamentally divided into two groups: the first comprises signal analysis methods, also known as *non-parametric methods*, which involve analyzing estimates of the spectral density functions of system responses. The second group corresponds to model-fitting methods, which rely on the response correlation functions of structural systems or directly on the response time series themselves, referred to as *parametric methods* (Rodrigues, 2004). Due to the inherent nature of ambient vibration providing multiple inputs, OMA is based on multiple-inputs/multiple-outputs (MIMO) techniques (Masciotta; Ramos, 2019).

Additionally, depending on the type of database, both parametric and non-parametric methods can be classified into one-phase or two-phase methods. One-phase methods directly use the response time series, while two-phase methods rely on the analysis of correlation functions in the time domain or spectral density functions in the frequency domain. These functions are used to characterize random vibrations (Brincker, 2014), and the advantage of using them lies in the synthesis they provide of information, reducing the volume of data required for the modal identification phase (Rodrigues, 2004)

Among the frequency domain methods, the simplest is the Basic Frequency Domain (BFD) method, or Peak-Picking method, which involves identifying modes by peaks in spectral density plots. This method assumes that the vibration modes of the tested structures have sufficiently separated frequencies and low damping. Thus, if the system has modes with very close frequencies, which is common in more complex structures, the results obtained can be misleading (Rodrigues, 2004; Zahid; Ong; Khoo, 2020). To overcome this limitation, the Frequency Domain Decomposition (FDD) Method was developed, widely used in modal identification. FDD is an extension of the BFD method, which uses Singular Value Decomposition (SVD) algorithms to diagonalize the matrix of spectral density functions and detect mode multiplicity (Rodrigues, 2004; Zahid; Ong; Khoo, 2020). Although the FDD method accurately identifies natural frequencies and vibration modes, it cannot estimate damping factors. Enhanced Frequency Domain Decomposition (EFDD) was then introduced as an improvement of the FDD method, capable of estimating modal shapes, damping ratios, and natural frequencies with even greater accuracy than the previous method. Additionally, there are parametric methods in the frequency domain based on fitting a model to the output spectrum or half-spectrum matrix, from which modal parameters are extracted in a second phase. Among them, the Least Squares

Complex Frequency Method and the Poly-Reference Least Squares Complex Frequency Method can be mentioned, widely used in civil engineering applications and commercially implemented under the name PolyMAX (Rainieri; Fabbrocino, 2014; Magalhães; Cunha, 2011).

Identification algorithms using time-domain methods are generally better conditioned than their frequency-domain counterparts (Rainieri; Fabbrocino, 2014). Among the parametric time-domain methods, there is a distinction between covariance-driven and data-driven methods. The former are two-phase methods, where the first phase involves estimating response correlation functions from measured data, followed by applying an identification method. The latter are one-phase methods, where model fitting is done directly to the response series (Rainieri; Fabbrocino, 2014; Rodrigues, 2004).

Within the covariance-driven methods, procedures from the NExT (Natural Excitation Technique) class are notable, relying on the autocorrelation and cross-correlation functions of the output responses in time, as well as the Covariance-driven Stochastic Subspace Identification (SSI-COV). Data-driven methods encompass the second variation of Stochastic Subspace Identification algorithms, the data-driven SSI (SSI-DATA), and methods based on ARMA (Auto-Regressive Moving Average) or AR (Auto-Regressive) models. The latter are not commonly employed in civil engineering, whereas SSI formulations represent the most commonly adopted parametric approach for applications in this field (Magalhães; Cunha, 2011).

2.3 Damage identification methods

The assessment of structural integrity through non-destructive methods, especially through vibration measurement tests, has emerged as an increasingly essential and relevant tool (Ceravolo *et al.*, 2016; Naderpour; Fakharian, 2016; Fan; Qiao, 2011).

The modal parameters obtained in dynamic tests include the natural frequencies, mode shapes, and modal dampings of the structure, which are intrinsically related to the stiffness and mass of the system, as discussed in Section 2.1. Thus, changes in these physical properties, caused by induced damage, material degradation, or possible changes in boundary conditions, directly affect the natural characteristics. Therefore, it becomes intuitive that damages can be identified by analyzing the changes in the vibration characteristics of the structures (Fan; Qiao, 2011).

Doebling *et al.* (1996) mention research related to damage detection methods in structures based on changes in dynamic properties. Among these approaches are variations in natural frequencies, changes in mode shapes and their derivatives, differences in curvature derived from vibration modes, alterations in modal flexibility, methods using modal strain energy (MSE), and the use of artificial neural networks. In recent decades,

the development of signal processing techniques, machine learning, deep learning, and artificial intelligence has been incorporated into the field of SHM, enabling significant advancements in performance and accuracy in damage modal identification methods, as demonstrated by reviews conducted by Hou and Xia (2021), Avci *et al.* (2021).

Therefore, a wide range of techniques, algorithms, and methods are available, capable of assessing everything from basic structural components to complex structural systems (Fan; Qiao, 2011). According to Rytter (1993), damage identification methods can be categorized at different levels, as follows:

- Level 1 (Detection): Determination that there is damage in the structure.
- Level 2 (Localization): Determination of the geometric location of the damage.
- Level 3 (Assessment): Quantification of the severity of the damage.
- Level 4 (Consequence): Prediction of the remaining service life of the structure.

The first three levels are addressed in the literature of modal analysis, while Level 4 prediction is generally categorized in the fields of fracture mechanics, fatigue life analysis, or structural design evaluation (Doebling *et al.*, 1996). The next topics will delve into some of the techniques mentioned earlier in greater detail, specifically those that will be adopted in this work.

2.3.1 Natural Frequency-based Methods

The choice to analyze the change in natural frequencies is convenient since obtaining these parameters can be done quickly, they exhibit less data dispersion, and are usually less contaminated by noise during acquisition (Oyarzo-Vera; Chouw, 2017; Fan; Qiao, 2011). However, relying on natural frequencies can have limitations such as not being able to locate the position of damage in the structure and being sensitive to changes caused by environmental and operational conditions that may mask the alterations in frequencies (Feijão, 2023).

The frequency data measured at different stages of damage can then have their sensitivity analyzed using statistical methods. Oyarzo-Vera and Chouw (2017) employ the "two-sample t-test for equal means" method to verify if the mean values of two populations are equal. Another possibility is the use of the Unified Significance Indicator (USI), proposed by Brincker *et al.* (1995) and expressed by Equation 2.28, which indicates the sum of the statistical significances for each of the natural frequencies ω_i.

$$USI = \sum_{i=1}^{m} (S_f)_i = \sum_{i=1}^{m} \frac{\omega_i^u - \omega_i^d}{\sqrt{(\sigma_\omega^u)_i^2 + (\sigma_\omega^d)_i^2}} \tag{2.28}$$

Where σ denotes the standard deviation, the subscript "u" refers to the undamaged state, the subscript "d" refers to the damaged state, and "m" is the number of estimated modes.

2.3.2 The Modal Assurance Criteria

The Modal Assurance Criteria (MAC) coefficient is an indicator that quantifies the degree of similarity between two mode shape vectors (Oyarzo-Vera; Chouw, 2017) and is calculated by the expression in equation 2.29. For example, modal vectors obtained in numerical modeling can be compared with those obtained experimentally, or experimental results can be compared with each other, with one of them serving as the reference (Juliani, 2014). In this work, the results of models in the undamaged condition, used as reference values, will be compared with the vectors obtained at different damage levels.

$$MAC_{(i,j)} = \frac{\left|\{\Phi_i^0\}^T - \left\{\Phi_j^d\right\}\right|^2}{\left(\{\Phi_i^0\}^T\{\Phi_i^0\}\right)\left(\left\{\Phi_j^d\right\}^T\left\{\Phi_j^d\right\}\right)} \tag{2.29}$$

where $\{\Phi_i^0\}$: is the mode shape vector of ith mode for the undamaged condition;
$\left\{\Phi_j^d\right\}$: is the mode shape vector of ith mode for the damaged condition.

The result of this expression is a scalar that varies from zero - representing no consistent correspondence (i.e., orthogonal vectors) - to one - indicating a consistent correspondence (Allemang, 2003). A popular way to represent the values of this coefficient is through two-dimensional plots (Figure 11a) or three-dimensional plots (Figura 11b), which provide a mode to mode discrete comparison using color gradients.

Figure 11 – Presentations of MAC values

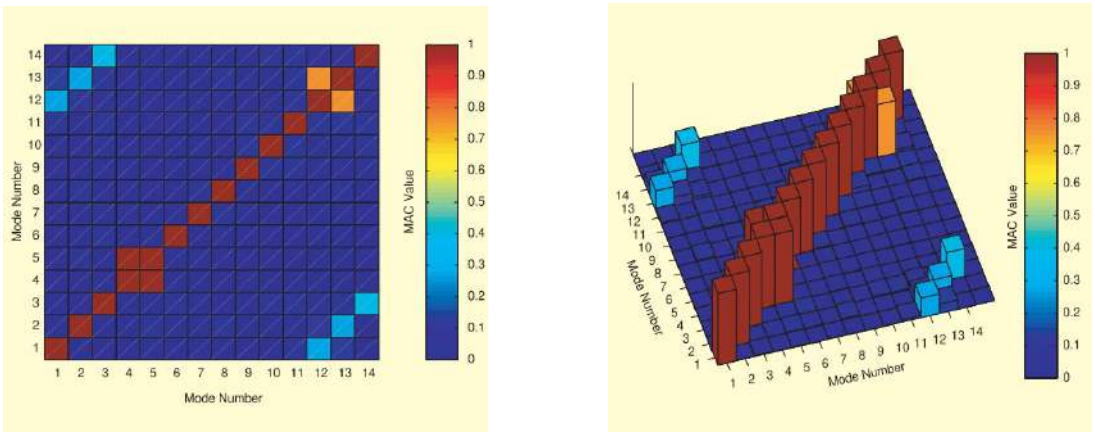

(a) (b)

Source: Allemang (2003)

2.3.3 The Coordinate Modal Assurance Criterion

A more effective method for determining damage location in a structure is the use of the Coordinate Modal Assurance Criterion (COMAC). Similar to the MAC coefficient, this indicator detects differences between two modal vectors (Oyarzo-Vera; Chouw, 2017). The difference is that COMAC indicates where these differences are located, as it investigates the correlation between the vectors for each degree of freedom j (Equation 2.30).

$$COMAC_{(j)} = \frac{\left(\sum_{i=1}^{m} \{\Phi_i^0\}_j - \left\{\Phi_i^d\right\}_j\right)^2}{\left(\sum_{i=1}^{m} \{\Phi_i^0\}_j \{\Phi_i^0\}_j\right)\left(\sum_{i=1}^{m} \left\{\Phi_i^d\right\}_j \left\{\Phi_i^d\right\}_j\right)} \tag{2.30}$$

where $\{\Phi_i^0\}$: is the mode shape vector of ith mode for the undamaged condition;
$\left\{\Phi_i^d\right\}$: is the mode shape vector of ith mode for the damaged condition;
m: is the number of modes considered in the analysis.

The COMAC also assumes values between 0 and 1, where 1 indicates a good correlation and 0 indicates low correlation. The discrepancy eventually detected by this indicator may be related to damage in the analyzed degree of freedom.

2.3.4 The Curvature Damage Factor

In structures exhibiting bending modes, a parameter used for damage identification and localization is the curvature of the vibration mode (Juliani, 2014). Initially proposed by Pandey, Biswas and Samman (1991), this method assumes that cracks or other forms of damage reduce the bending stiffness (EI) of the structures at the cracked section or damaged region, resulting in increased curvature in that segment. Therefore, the Curvature Damage Factor (CDF), introduced by Abdel Wahab and De Roeck (1999), corresponds to the average absolute change of the modal curvatures (second derivative of the mode shape) considering several modes, as observed in the equation 2.31.

$$CDF = \frac{1}{m} \sum_{i=1}^{m} \left| \phi''_{i,0} - \phi''_{i,d} \right| \tag{2.31}$$

where $\phi''_{i,0}$: is the undamaged modal curvature of the ith node;
$\phi''_{i,d}$: is the damaged modal curvature of the ith node;
m: is the number of modes considered in the analysis.

According to Oyarzo-Vera and Chouw (2017), when considering multiple modes, the change in curvature at the damaged location becomes non-zero, allowing for damage identification. For instance, the consideration of only one vibration mode might not stress a damaged section. Figure 12 illustrates the modal curvature difference plot, the typical representation of these coefficient results, with the peak distinctly indicating the damage location among the listed measurement points on the abscissa axis.

Figure 12 – Plot of Curvature Damage Factor (CDF)

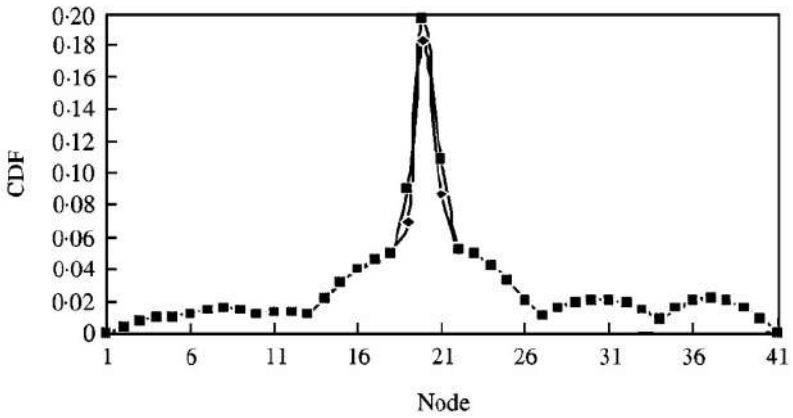

Source: Abdel Wahab and De Roeck (1999)

2.4 Dynamic models

According to Pacífico (2017), "A model is a representation of a physical system that can be used to predict the behavior of a system concerning some desired aspect." Typically, the model is constructed at a reduced scale and aims to meet similitude requirements with the prototype: the full-scale physical system for which the predictions are made.

The choice of small-scale models is a strategy adopted in various research studies and addresses challenges that may arise in the experimental analysis of large-scale specimens related to transportation, manufacturing, costs, or the considerable capacity demand of reaction frames and hydraulic actuators (Milani *et al.*, 2021).

The modeling study should consider the scope of the problem, namely what needs to be evaluated in the model, as well as the specific similitude requirements for geometry, materials, loading, and interpretation of results. These requirements are established by Buckingham's Pi theorem, a crucial procedure in dimensional analysis for calculating dimensionless terms from the variables of the problem. Obviously, it is not always possible to establish complete similarity in all structural models. In this regard, three types are considered according to the fulfillment of the requirements (Casaburo *et al.*, 2019):

1. **True models:** These satisfy all the stipulations established and possess complete similarity.
2. **Adequate models:** These fulfill the first-order stipulations – conditions related to the main parameters – but not necessarily the second-order ones.
3. **Distorted models:** These do not adhere to one or more first-order stipulations.

In the dimensional analysis of dynamic models, in addition to the length (L) and force (F) variables considered in static loading situations, time (T) needs to be included

as one of the fundamental quantities of the problem (Harris; Sabnis, 1999). Thus, the similitude requirements for elastic vibration problems can be given by scale factors, defined by Equation 2.32, which relate the physical quantities and parameters to be determined.

$$S_i = i_p / i_m \tag{2.32}$$

S_i is defined as the scale factor for quantity i and the subscripts p and m reference prototype and model, respectively. In Frame 1 below, the similarity requirements are presented by the scale factors related to the Elastic Modulus (E) and length (l).

Frame 1 – Similitude requirements for elastic vibrations

			Scale Factor	
Group	Quantity	Dimension	Exact Scaling	Gravity Forces Neglected
Loading	Force, Q	F	$S_E S_l^2$	$S_E S_l^2$
	Gravitational acceleration, g	LT^{-2}	1	1
	Time, t	T	$S_l^{1/2}$	S_l
Geometry	Linear dimension, l	L	S_l	S_l
	Displacement, δ	L	S_l	S_l
	Frequency, f	T^{-1}	$S_l^{-1/2}$	S_l^{-1}
Material properties	Modulus, E	FL^{-2}	S_E	S_E
	Stress, σ	FL^{-2}	S_E	S_E
	Poisson's ratio, ν	$-$	1	1
	Specific weight, γ	FL^{-3}	S_E/S_l	*Neglected*

Source: Harris and Sabnis (1999)

It is noted that the scale factor for time is equal to $S_l^{1/2}$ or S_l if the effect of gravity is disregarded. This implies that the frequency – which is the inverse of the period in seconds – will have a scale factor equal to $S_l^{-1/2}$ or S_l^{-1}. In other words, in small-scale models, the frequency values are higher when compared to prototypes (Harris; Sabnis, 1999). Taking the scale adopted in this work, 1:5 ($S_l = 5$), as an example, and considering that the model has the same material-related constants as the real structure, it is expected that the natural frequencies will be $\sqrt{5} = 2,24$ times higher.

3 STRUCTURAL BEHAVIOR OF MASONRY WALLS

Modern masonry is a composite material made of units - ceramic bricks, concrete blocks, stone, glass - joined by mortar joints. Masonry walls may be constructed with solid or hollow units, which may or may not be reinforced (Hamid; Schuller, 2019). Its behavior is anisotropic, nonlinear, and complex (when compared to materials like concrete or steel), due to the different materials composing it and the large number of interfaces (Costigan; Pavía; Kinnane, 2015). As structural elements, masonry walls are commonly used in masonry buildings or as infill panels within reinforced concrete frames. In such configurations, they play a critical role in resisting in-plane loads generated by wind or seismic actions (Drysdale; Hamid; Baker, 1994).

This research focuses specifically on unreinforced masonry walls and their behavior under shear-induced damage. Therefore, this chapter aims to present the fundamental concepts related to that structural element, including its modeling, failure mechanisms, and reduced scale models, based on the literature.

3.1 Numerical modeling of masonry

The need to predict and understand the behavior of masonry has led, in recent decades, to the development of theoretical and numerical tools for modeling this material. In simulating masonry walls using the Finite Element Method, three distinct strategies with different levels of detail can be implemented, as proposed by Lourenço (1996). These strategies include detailed micro-modeling (a), simplified micro-modeling (b), and macro-modeling (c), as illustrated in Figure 13.

Figure 13 – Modeling strategies for masonry structures

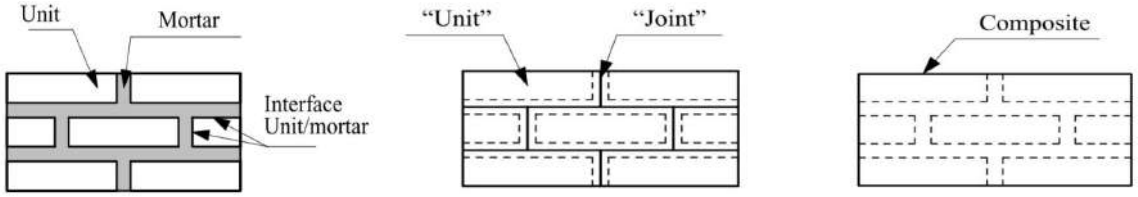

Source: Adapted from Lourenço (1996)

Detailed micro-modeling involves separately modeling the units, mortar joints, and the wall/frame interface, as well as their respective constitutive models. In the **simplified micro-modeling** method, the thickness of the units is increased on all sides to half the thickness of the mortar, which, in turn, is represented as an average zero-thickness interface using discontinuous elements—this transformation is depicted in Figure

14. **Macro-models**, on the other hand, follow a simplified simulation technique in which the entire masonry wall, including the units and mortar, is modeled as a single panel, aiming to predict only the relevant outcomes (Bhaskar; Bhunia; Palchuri, 2023; Uemura, 2023).

Figure 14 – Transforming to simplified micro modeling according to Lourenço (1996)

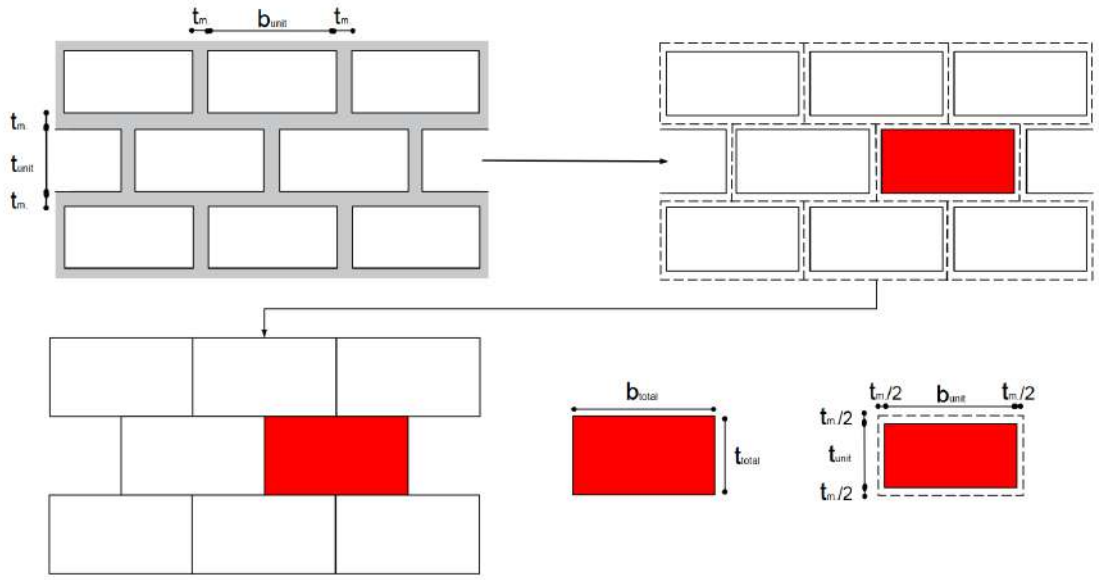

Source: Adapted from Bouarroudj and Boudaoud (2022)

The choice of technique depends on the the specific application and analytical goals. It's evident that different methods lead to different results, depending on the approach and available information (Sarhosis; Lemos, 2018). For the study of structural details or deformations at high stress levels, micro-modeling is recommended. On the other hand, macro-modeling is geared towards large structures, simulating their overall behavior (Uemura, 2023). In all cases, however, a detailed description of the materials is fundamental to improve the accuracy of the models (Lourenço, 1996).

3.2 Failure modes of shear walls

Walls subjected to in-plane loading are referred to as shear walls due to the dominance of shear efforts. Functioning like vertical cantilevers or fixed end elements, their stiffness is largely influenced by the aspect ratio (height-to-length). This ratio significantly affects the failure mode since low aspect ratios lead to shear failures, while slender walls exhibit flexural behavior. Other factors also affect the failure mechanism, including the combination of applied loads, material properties, and the bond pattern (Haach, 2009). To introduce this subject, Figure 15 presents crack patterns exhibited by shear walls.

To accurately predict the behavior of masonry walls under biaxial stress, as in the case of shear walls, it is essential to understand the deformation and failure characteristics

Figure 15 – Representative cracking patterns observed in shear walls

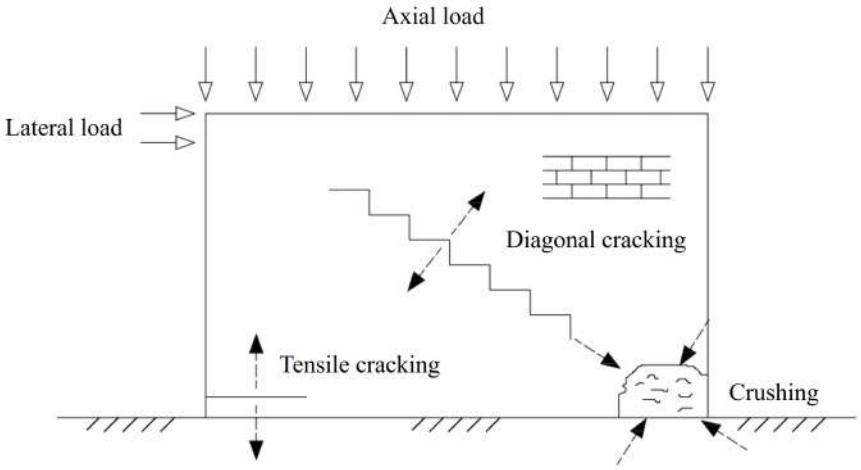

Source: Adapted from Haach (2009)

of masonry under such loading conditions (Andreaus, 1996). As noted by Drysdale, Hamid and Baker (1994), the shear capacity of unreinforced shear walls is significantly influenced by the level of axial compression-based on a Coulomb failure criterion-as it tends to delay tensile cracking and enhance the shear friction component of the overall shear strength. When axial loads remain at moderate levels, failure may occur either in shear or in flexure, depending primarily on the wall's aspect ratio. In the shear failure mode, diagonal cracks typically develop along the unit mortar interfaces, or both along the interfaces and through the units, as a result of a biaxial tension compression stress state, which often leads to collapse in unreinforced masonry. In contrast, flexural failure is characterized by the formation of horizontal cracks at the unit mortar interfaces due to the low tensile bond strength of the masonry (Haach, 2009).

According Andreaus (1996) there are ten mechanisms of failure to masonry subject to in-plane loading corresponding with three distinct modes failure criterions, namely: Mohr-Coulomb (associated with the slipping mode), Saint-Venant (with the splitting mode) and Navier (with the spalling mode). Those failure models are listed below and Figure 16 provides a graphical representation of all the mentioned failure modes.

1. **Slipping on mortar joints:** Failure occurred mainly in the mortar joints, following a stepped cracking pattern, and typically developed under compression levels up to 2 MPa.

2. **Slipping on bed joints:** Failure was observed along one or more planes perpendicular to the specimen's surface, characterized by sliding along a bed joint. This occurred under conditions of high parallel compressive and shear stresses relative to the normal compressive stress.

3. **Splitting and slipping of bed joints:** Failure was observed to occur along the bed joints, constituting the ultimate failure of the wall, and was associated with both low parallel tensile and shear stresses relative to the normal tensile stress, as well as high parallel compressive and shear stresses relative to the normal tensile stress.

4. **Splitting of bricks and slipping of mortar joints:** Panel failure occurs through cracking and sliding in the bed and/or head joints, or through a combined mechanism involving cracking in both the brick and the joint, depending on the relative levels of shear and compressive stresses along the joints.

5. **Splitting of bricks and head joints:** This failure mode is characterized by tensile debonding between the mortar and the brick along the head joints, and/or by tensile cracking of the brick itself in certain courses. This type of failure tends to occur in weaker bricks.

6. **Slipping of bed joints and splitting of head joints:** The splitting crack propagates along the head joints, resembling the previous failure mode but typically occurring in cases where the bricks are stronger and the mortar is comparatively weaker.

7. **Splitting of bed joints:** Panel failure occurs in a direction perpendicular to the plane of the panel, either due to compression parallel to the bed joints or tension perpendicular to them.

8. **Slipping and splitting of mortar joints:** A combined slipping and splitting failure mechanism, forming a zigzag pattern through the bed and head joints, is observed when high parallel tensile and shear stresses acted relative to the normal tensile stress or when shear and tensile stresses are of comparable magnitude, leading to ultimate failure along the bed and head joints.

9. **Biaxial deformation:** All failures within this range propagate along the jointing planes and the final collapse occurs once a sufficient number of joints have failed, enabling the formation of a collapse mechanism.

10. **Middle plane spalling:** Failure occurs in the case of biaxial compression with very high compressive stresses with respect to shear stress. The spalling occurs suddenly and in a brittle manner.

3.3 Small scaled models for masonry

The study of structural system behavior through scaled models has been an important tool in civil engineering and is widely used in research with satisfactory outcomes (Nascimento Neto, 2003; Harris; Sabnis, 1999). Several studies conducted in Brazil (Silva,

Figure 16 – Summary of failure modes observed in masonry panels

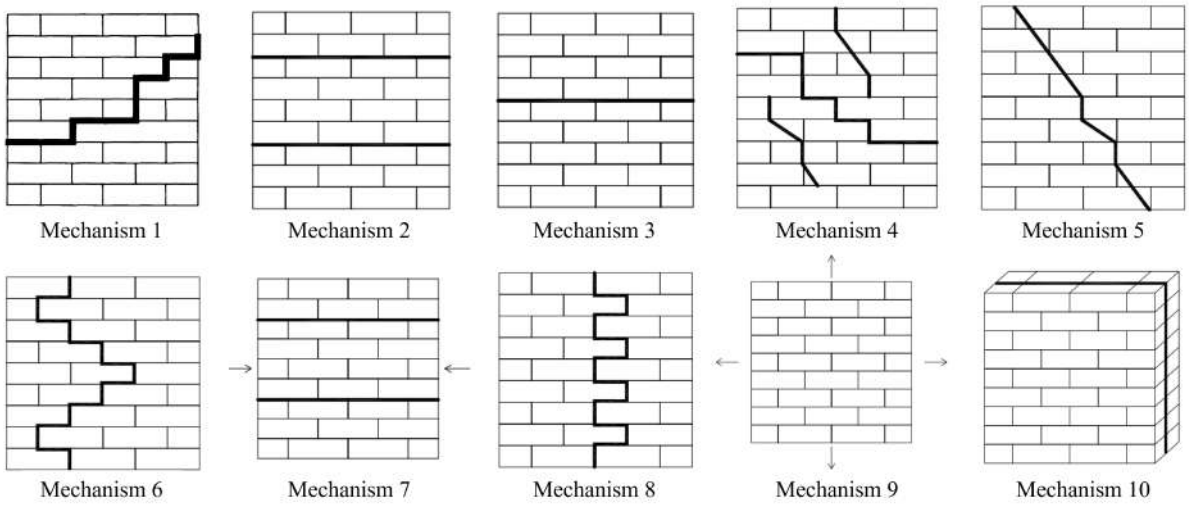

Source: Adapted from Haach (2009)

2014; Moreira, 2007; Maurício, 2005; Capuzzo Neto, 2015; Nascimento Neto, 2003) using reduced models of masonry made of concrete or load-bearing clay blocks—typically at scales ranging from 1:3 to 1:5—have demonstrated the feasibility and effectiveness of this approach. When a model satisfies the conditions of similitude, it is expected to reproduce the qualitative behavior of the prototype (Casaburo *et al.*, 2019).

It is thus essential to choose materials and loading conditions that are consistent with the scale and intended purpose of the physical model. The data obtained from testing the reduced-scale structure must be carefully interpreted to enable reliable predictions of the behavior of the full-scale structure. This requires the application of scaling laws that establish the relationships between the responses of the model and those of the prototype (Capuzzo Neto, 2015).

To achieve full similarity in structural behavior, including inelastic effects such as cracking and yielding, a model with complete similitude, referred to as a true model, must be constructed. However, when the stresses caused by the self-weight of the structure are considered negligible, as is often the case in masonry buildings, a "practically true" modeling approach may be adopted. Even in this simplified approach, it remains necessary for the stress and strain behavior of the materials in the model and in the prototype to be equivalent. This presents a significant challenge, since masonry is a composite material and it is difficult to produce units at reduced dimensions that replicate the mechanical properties of full-size elements (Harris; Sabnis, 1999). Frame 2 presents the similitude requirements for various quantities, expressed in terms of scale factors related to stress (σ) and length (l), as applied in the static analysis of masonry structures.

It should also be noted that it is essential to consider, predict, and attempt to minimize the size effect, that is, changes in the structural response to external actions

Frame 2 – Similitude requirements for masonry

			Static Loading	
Group	Quantity	Dimension	True Model	Practical True Model
Loading	Concentrated load, Q	F	$S_\sigma S_l^2$	S_l^2
	Line load, w	FL^{-1}	$S_\sigma S_l$	S_l
	Pressure, q	FL^{-2}	S_σ	1
	Moment, M	FL	$S_\sigma S_l^3$	S_l^3
Geometry	Linear dimension, l	L	S_l	S_l
	Displacement, δ	L	S_l	S_l
	Angular displacement, β	1	1	1
	Area, A	L^2	S_l^2	S_l^2
Material properties	Masonry unit stress, σ_m	FL^{-2}	S_σ	1
	Masonry unit strain, ε_m	1	1	1
	Modulus of masonry unit, E_m	FL^{-2}	S_σ	1
	Masonry unit Poisson's ratio, ν_m	1	1	1
	Specific weight, γ_m	FL^{-3}	S_σ/S_l	$1/S_l$
	Mortar stress, σ'_m	FL^{-2}	S_σ	1
	Mortar strain, ε'_m	1	1	1
	Modulus of mortar, E'_m	FL^{-2}	S_σ	1
	Mortar Poisson's ratio, ν'_m	1	1	1
	Reinforcement stress, σ_{rm}	FL^{-2}	S_σ	1
	Reinforcement strain, ε_{rm}	1	1	1
	Modulus of reinforcement, E_{rm}	FL^{-2}	S_σ	1

Source: Harris and Sabnis (1999)

resulting from variations in the geometric dimensions of the structure or its components (Casaburo *et al.*, 2019). Despite the challenges involved, it is considered feasible to conduct tests on masonry models, provided that careful attention is given to all stages, from the selection of materials to the manufacturing process of the masonry units (Capuzzo Neto, 2015).

4 EXPERIMENTAL PROGRAM

This chapter presents the methodology adopted for the study of the dynamic behavior of masonry walls in this research. In addition to detailing the physical models selected for investigation and describing the procedures and equipment used in the experimental campaign, it also includes the characterization of the constituent materials. The main results of this experimental campaign are discussed in detail in Chapter 5.

4.1 Masonry specimens description

As aforementioned, reduced scale (1:5) units were used in the tested masonry panels. The choice of reduced-scale physical models to obtain the dynamic properties of this material is a strategy that allows for increased testing scenarios and enables damage analysis by overcoming the limitations of laboratory equipment such as reaction frames and hydraulic actuators.

Two wall typologies were considered in this study: one built with concrete blocks, manufactured by MiniBloco, and the other with clay blocks, produced by Cerâmica City. Both shared the same overall geometry to isolate the influence of the material and its specific characteristics. Three specimens of each type were constructed, totaling six wall panels. From this point forward, models built with concrete blocks are referred to as "PCO", and those with clay blocks as "PCE". Figure 17 shows the adopted dimensions for each typology.

The overall geometry of the panels was defined to reflect the typical proportions adopted for masonry infill walls in reinforced concrete frames commonly used in Brazilian construction practice. It is also important to note that slight variations in wall width occurred due to differences in the dimensions of the individual blocks, which are detailed in Section 4.2.1. For this reason, in the case of the concrete block walls, a configuration using a single half block per course was adopted to maintain dimensional consistency.

4.2 Characterization of materials

Accurate experimental and numerical analyses require a thorough specification of the material, which depends on the availability of detailed information on the mechanical properties of both the individual masonry materials and the composite masonry system. Thus, a series of characterization tests were conducted to determine the geometrical and mechanical properties of each material and masonry element used in this research.

To summarize all planned procedures, Figure 18 presents a flowchart that specifies the prescribed tests, the number of samples, and the corresponding standards.

Figure 17 – Geometry of masonry walls with distinct block materials. Measurements in millimeters

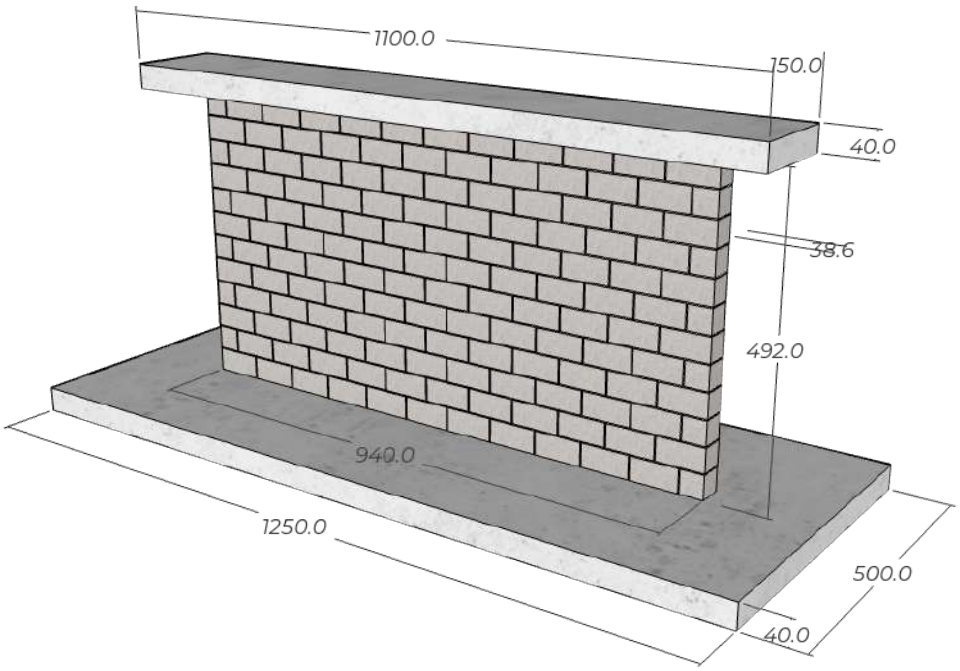

(a) Concrete block wall

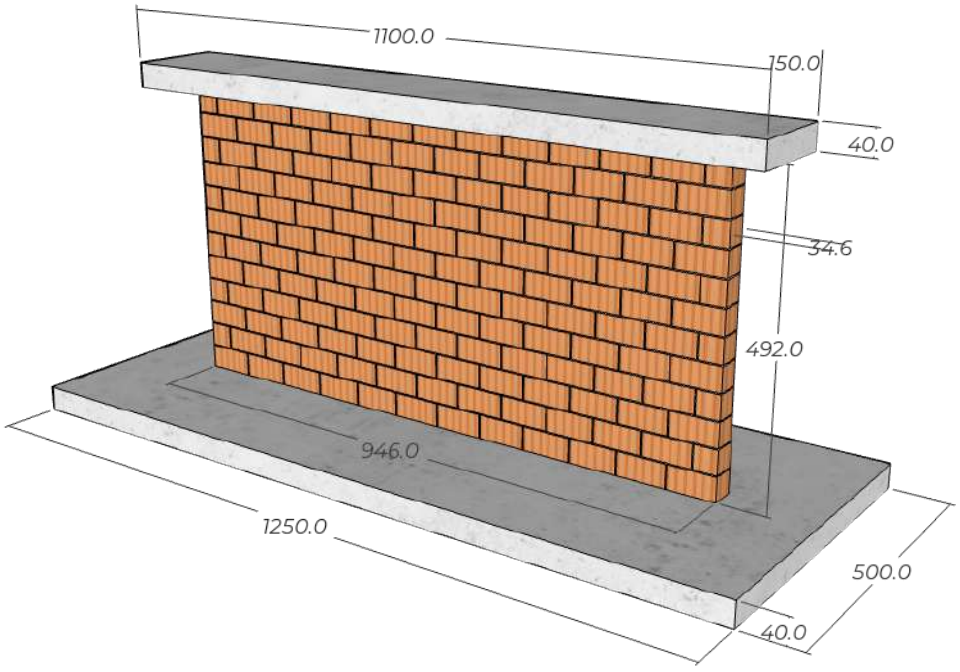

(b) Clay block wall

Source: Author (2025)

Figure 18 – Diagram of characterization tests

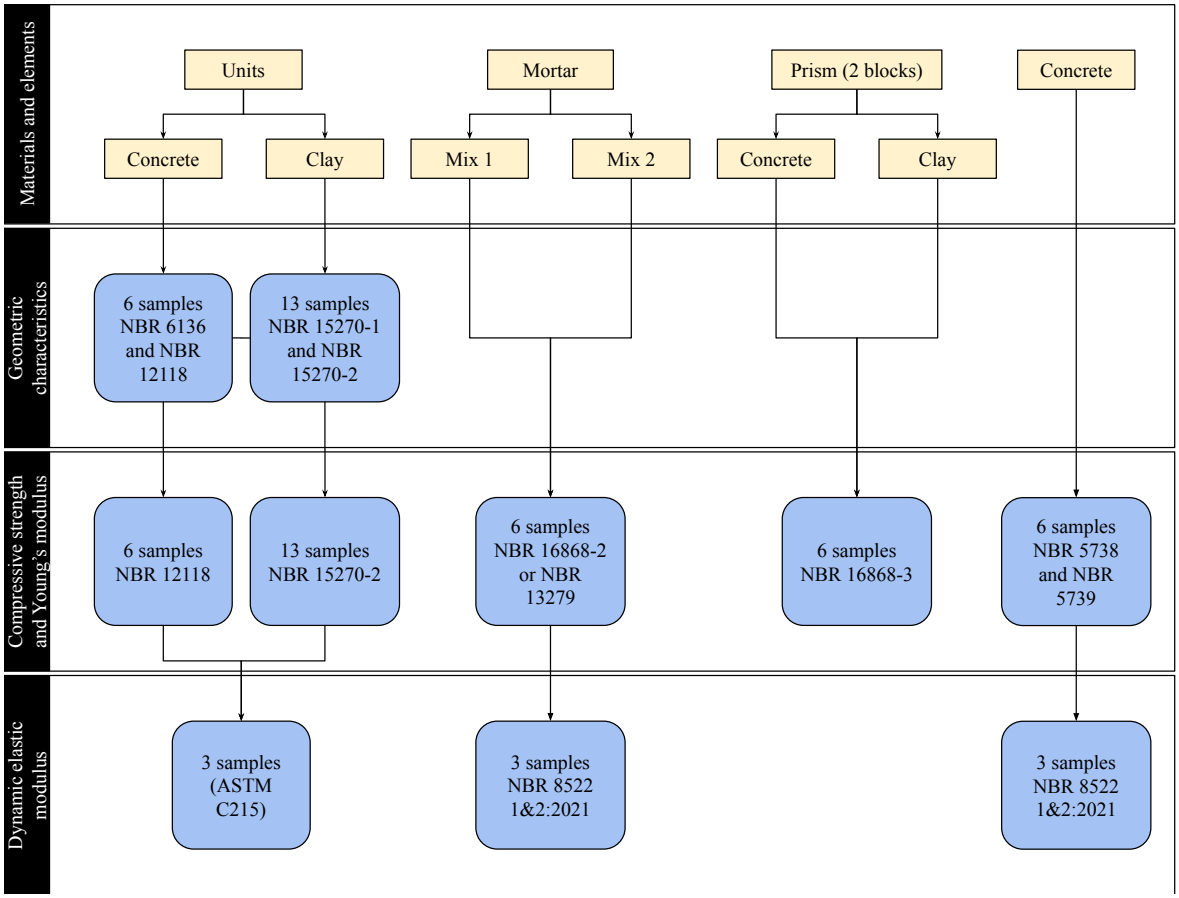

Source: Author (2025)

4.2.1 Units

The characterization of units (blocks and bricks) and the understanding of their basic properties constitute the first step toward a comprehensive understanding of masonry (Parsekian; Hamid; Drysdale, 2013). For this reason, this section begins with the description of these elements.

Two distinct types of units were analyzed: load-bearing concrete blocks and load-bearing clay blocks, both at a reduced scale of 1:5. Figure 19a shows the typologies of the blocks used in this study, while Figure 19b provides a visual comparison between the full-scale (1:1) and reduced-scale (1:5) versions of the units. It is important to emphasize that no control was exercised over the production process of the concrete blocks, and the specific materials used in their manufacturing are not known. Consequently, no considerations were made regarding the aggregates incorporated in the concrete or their potential influence on scale effects.

The concrete blocks were based on a standard block family with nominal dimensions of 19 × 19 × 39 cm (Width × Height × Length) in their full-scale form. The corresponding reduced dimensions were 3.8 × 3.8 × 7.8 cm, which matched the actual measurements of the

acquired concrete units, thereby validating the adopted scaling approach for this material. In contrast, the scaled clay blocks represent a block family with nominal dimensions of 14 × 19 × 29 cm at full scale, corresponding to 2.8 × 3.8 × 5.8 cm at the 1:5 scale. However, the clay blocks used in the experiments exhibited actual dimensions of 3.4 × 3.8 × 6.9 cm, showing a slight deviation from the theoretical values. In order to assess the implications of this discrepancy, a detailed dimensional analysis will be presented in the following sections.

Figure 19 – Typical small-scale blocks used in this study

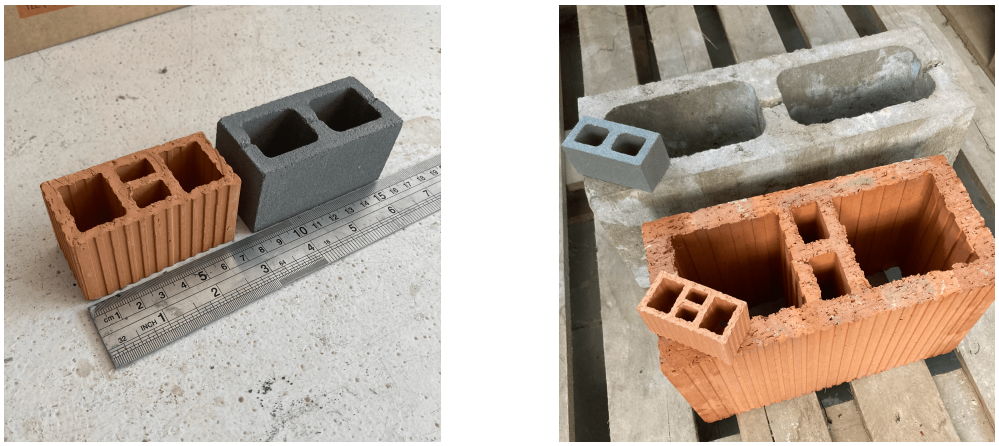

(a) (b)

Source: Author (2025)

4.2.1.1 Geometrical and mechanical properties of concrete blocks

The geometrical properties of the concrete units were determined using a 200 mm digital caliper. The measurements included the width, length, and height – each obtained from at least three measurements at different points on the face with the greatest shell thickness (the peripheral material between a cell and the face of the unit). The minimum web thicknesses (the solid material between adjacent cells) were measured at two locations along each shell and at one location on each web, all taken on the face with the smallest shell thickness. Additionally, the cell dimensions were determined by two measurements per cell: one in the longitudinal direction and one in the transverse direction, both taken approximately at the center of the cell on the face with the greatest shell thickness.

The results for the effective dimensions of the regular and half concrete blocks are presented in Table 1, along with the standard deviation and the coefficient of variation. Other properties, including the minimum equivalent thickness – calculated as the sum of the thicknesses of all webs divided by the measured block length – are shown in Table 2, which also includes the individual measurements. Finally, all data are summarized in Figure 20.

The effective dimensions refer to blocks from the 20 x 40 family, which have nominal dimensions of 190 x 190 x 390 mm (width x height x length), as specified in ABNT NBR

Table 1 – Effective dimensions for regular and half concrete blocks at reduced scale

	Regular block			**Half block**		
	Width (mm)	Height (mm)	Length (mm)	Width (mm)	Height (mm)	Length (mm)
Mean	38.57	38.28	78.67	38.55	37.07	40.71
SD	0.462	0.170	0.900	0.455	0.545	1.463
COV(%)	1.20	0.22	2.35	1.18	1.34	3.95

Source: Author (2025)

Table 2 – Shell and web thicknesses and cell dimensions of regular concrete blocks at reduced scale

	Thicknesses			**Cell dimensions**	
	Shells (mm)	Webs (mm)	Minimum equivalent thickness (mm/m)	Longitudinal (mm)	Transversal (mm)
CO - 01	6.95	7.26	276.86	26.25	22.03
CO - 02	7.00	7.18	273.94	26.25	22.15
CO - 03	7.29	7.30	278.26	28.34	24.21
CO - 04	7.17	7.37	281.18	26.05	21.76
CO - 05	7.32	7.14	272.41	26.11	21.92
CO - 06	7.44	7.28	277.62	26.08	21.95
Mean	7.19	7.26	276.71	26.51	22.34
SD	0.19	0.08	3.14	0.90	0.93
COV(%)	2.64	1.14	1.14	3.39	4.15

Source: Author (2025)

6136:2016 (Associação Brasileira de Normas Técnicas, 2016), with the application of a geometric scale factor of 5. According to this standard, the dimensional tolerances are ±2.0 mm for the width and ±3.0 mm for the height and length. For the reduced scale, proportional tolerances of ±0.4 mm for the width and ±0.6 mm for the average height and length were applied. Table 3 presents the deviations from the nominal values.

Table 3 – Compliance with dimensional tolerances for concrete blocks

	Regular block			**Half block**		
	Width (mm)	Height (mm)	Length (mm)	Width (mm)	Height (mm)	Length (mm)
Nominal	38	38	78	38	38	38
Measured	38.569	38.277	78.668	38.545	37.065	40.705
Deviation	0.569	0.277	0.668	0.545	-0.935	2.705
Tolerance	±0.4	±0.6	±0.6	±0.4	±0.6	±0.6
Compliance	No	Yes	No	No	Yes	No

Source: Author (2025)

Figure 20 – Geometry of concrete blocks and half blocks. Measurements in millimeters

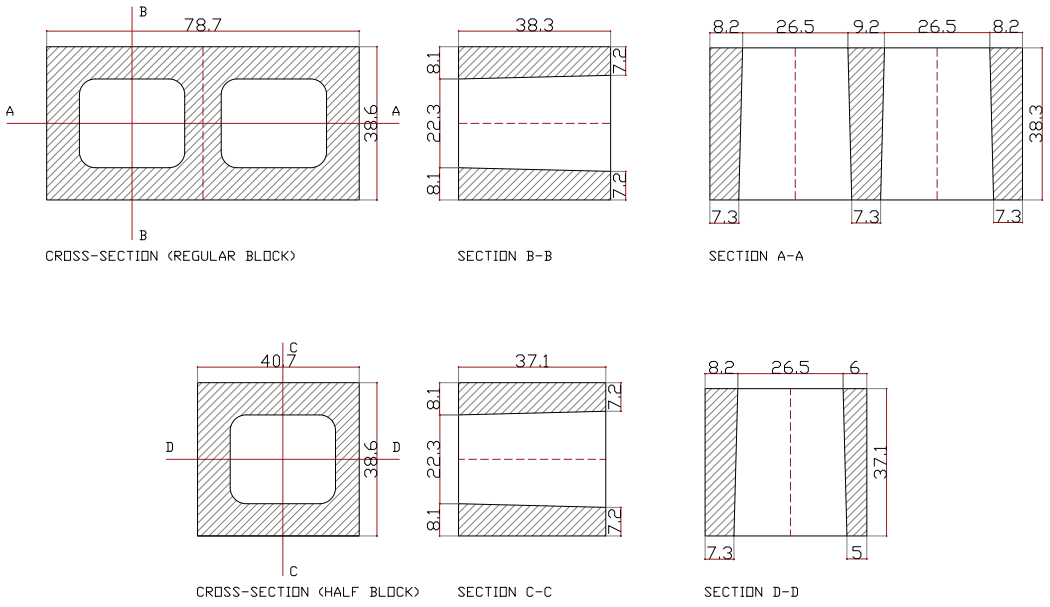

Source: Author (2025)

From the analysis, it can be observed that only the height of the blocks and half blocks complies with the standard tolerance, indicating a strict criterion corresponding to the proportional scale reduction. It is also noted that the length of the half blocks shows a significant dimensional discrepancy, which can be attributed to the production process of these reduced-scale elements, derived from cutting the regular blocks. Furthermore, NBR 6136:2016 specifies minimum values for the shells and webs, equivalent thickness, and the smallest cell dimension for blocks in classes A and B with a nominal width of 190 mm. These values must be 32 mm, 25 mm, 188 mm/m, and 110 mm, respectively, with a tolerance of 1 mm. After applying the scale factor, these values become 6.4 mm, 5 mm, 37.6 mm/m, and 22 mm, with a tolerance of 0.2 mm. Based on the data in Table 2, it can be concluded that the blocks met the required specifications.

The net area (A_{net}) of the concrete block was determined by immersing the saturated block in water and applying Archimedes' principle to calculate the displaced volume, based on the difference between submerged and saturated mass, as defined by Eq. 4.1

$$A_{\text{net}} = \frac{m_{\text{sat}} - m_{\text{sub}}}{\rho_{\text{water}} \cdot h} \times 1000 \tag{4.1}$$

Where ρ_{water} is the specific weight of water (typically taken as 1 g/cm^3) and H is the average height of the block (in mm). Therefore, when the masses are expressed in grams, the resulting net area A_{net} is given in mm^2. Table 4 presents the results for both gross and net areas, along with the ratio between them.

Table 4 – Gross and net areas of reduced-scale concrete blocks

	Gross area (mm²)	**Net area (mm²)**	A_{net}/A_{gross} **(%)**
Mean	3034.17	1741.55	
SD	40.60	25.73	57.40
COV(%)	1.20	1.48	

Source: Author (2025)

For the determination of compressive strength, six samples were selected for the axial compression test, along with three additional control blocks used to verify relative humidity, which ultimately met the requirements established by the standards. The tests were carried out using a servo-hydraulic Instron machine, with a nominal load capacity of 1500 kN, located at the Structural Laboratory (LE-SET). The load was applied under displacement control at a rate of 0.005 mm/s. The bearing surfaces were leveled using a grinding machine, and the specimens were conditioned in the laboratory environment for 72 hours prior to testing. Individual results were subjected to the Grubbs statistical test, with a significance level 5%, to identify potential outliers. The test did not indicate sufficient evidence to detect any outliers.

The average values of ultimate load and the mean compressive strength based on the gross cross-sectional area (f_{bm}) are presented in Table 5. The characteristic compressive strength (f_{bk}), calculated according to ABNT NBR 6136:2016, along with its parameters and results, is shown in Table 6.

Table 5 – Compressive strength of reduced-scale concrete blocks

	Load (kN)	f_{bm} **(MPa)**
Mean	34.82	11.47
SD	7.56	2.49
COV(%)	21.7	21.7

Source: Author (2025)

Table 6 – Characteristic compressive strength of reduced-scale concrete blocks

f_{bm} (MPa)	11.47
$f_{bk,est}$ (MPa)	6.32
$\phi \times f_{b1}$ (MPa)	7.04
f_{bk} **(MPa)**	**7.04**

Source: Author (2025)

4.2.1.2 Geometrical and mechanical properties of clay blocks

The geometric properties of the clay units were evaluated following a procedure similar to that applied to the concrete blocks. The assessed characteristics include the face

dimensions and the thicknesses of the webs and external walls of the blocks.

For the measurement of the effective dimensions, two readings were taken for each dimension of the sampled blocks, and the mean values are presented in Table 7. The thicknesses of the external walls and internal webs were measured only on regular blocks, with the individual values and the corresponding measurement locations detailed in Table 8. Figure 21 exposes in detail the cross-section geometry of clay units and half blocks.

Table 7 – Effective dimensions for regular and half clay blocks at reduced scale

	Regular block			**Half block**		
	Width (mm)	Height (mm)	Length (mm)	Width (mm)	Height (mm)	Length (mm)
Mean	34.57	38.43	69.91	33.92	38.07	34.64
SD	0.275	0.421	0.394	0.198	0.494	0.335
COV(%)	0.79	0.60	1.02	0.58	1.42	0.88

Source: Author (2025)

Table 8 – Individual measurements of external walls and internal webs of clay blocks

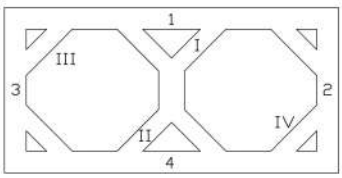

	External walls				**Internal webs**			
	1 (mm)	**2 (mm)**	**3 (mm)**	**4 (mm)**	**I (mm)**	**II (mm)**	**III (mm)**	**IV (mm)**
CE - 1	4.93	4.61	4.65	4.71	4.30	4.37	4.10	3.46
CE - 2	4.63	4.54	4.09	4.58	3.53	3.93	3.60	3.20
CE - 3	4.58	4.46	4.48	4.42	3.71	3.44	4.10	3.40
CE - 4	4.65	4.26	4.57	4.71	3.70	4.39	4.39	3.85
CE - 5	4.21	4.39	4.55	4.62	4.22	4.20	3.82	3.16
CE - 6	4.68	4.49	4.35	4.30	3.90	4.29	4.15	3.68
CE - 7	5.33	4.65	4.53	4.50	3.67	3.97	4.00	3.42
CE - 8	4.07	4.52	4.38	4.88	4.20	4.07	3.47	3.58
CE - 9	4.68	4.54	4.45	4.75	4.07	3.85	3.57	3.70
CE - 10	4.64	4.60	4.53	5.08	4.30	3.52	3.45	3.68
CE - 11	4.50	4.44	4.30	4.66	3.75	4.32	3.75	3.34
CE - 12	4.07	4.51	4.25	4.66	4.06	4.13	3.28	3.46
CE - 13	4.57	4.77	4.32	4.74	3.66	4.30	3.80	3.50

Source: Author (2025)

Ideally, the blocks used would correspond to the 14 family of load-bearing clay blocks, featuring real-scale dimensions of 140 × 190 × 390 mm and reduced-scale dimensions

Figure 21 – Geometry of clay blocks and half blocks. Measurements in millimeters

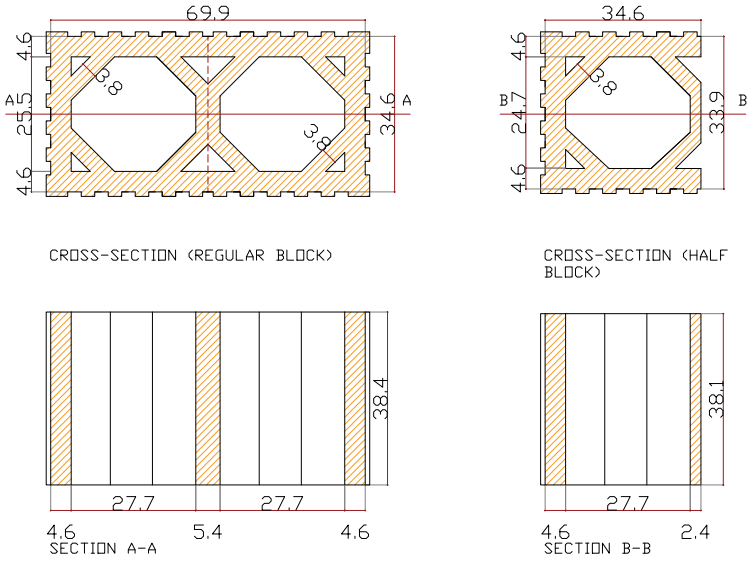

Source: Author (2025)

of 28 × 38 × 78 mm. However, as shown in Table 9, the deviations observed in height and length significantly exceed the dimensional tolerance limits for the mean effective dimensions, as established by ABNT NBR 15270-2:2023 (Associação Brasileira de Normas Técnicas, 2023b): ±3 mm for real scale and ±0.6 mm for the scale adopted in this study. Furthermore, according to the same standard, for load-bearing clay blocks with hollow walls, the minimum thickness requirements are 7 mm for internal webs and 8 mm for external walls. When scaled, these thresholds correspond to 1.4 mm and 1.6 mm, respectively, with the blocks meeting these specifications.

Table 9 – Compliance with tolerance in clay block dimensions

	Regular block			**Half block**		
	Width (mm)	Height (mm)	Length (mm)	Width (mm)	Height (mm)	Length (mm)
Nominal	28	38	78	28	38	38
Measured	34.573	38.435	69.912	33.923	38.066	34.643
Deviation	6.573	0.435	8.088	5.923	0.066	3.357
Tolerance	±0.60	±0.60	±0.60	±0.60	±0.60	±0.60
Compliance	No	Yes	No	No	Yes	No

Source: Author (2025)

To calculate the net area of the clay blocks, the same methodology used for the concrete blocks was adopted, as also prescribed by ABNT NBR 15270-2 (Associação Brasileira de Normas Técnicas, 2023b). The corresponding values of gross and net areas

are presented in Table 10.

Table 10 – Gross and net areas of reduced-scale clay blocks

	Gross area (mm²)	**Net area (mm²)**	A_{net}/A_{gross} **(%)**
Mean	2417.14	1066.11	
SD	31.67	37.58	44.11
COV(%)	1.31	3.53	

Source: Author (2025)

The equipment and procedures employed for the axial compression testing of the concrete units were also utilized for the clay units, with the exception of the method adopted to ensure the flatness of the bearing surfaces, which was achieved through manual sanding. According to ABNT NBR 15270-3:2017 (Associação Brasileira de Normas Técnicas, 2017), clay blocks must be tested for compression in a saturated condition. Therefore, the blocks were immersed in water for 12 hours prior to testing and subsequently positioned in the testing machine, configured as shown in Figure 22. The load was applied under displacement control at a rate of 0.005 mm/s. As with the concrete units, individual results were subjected to the Grubbs test with a 5% significance level, and no outliers were identified.

Figure 22 – Axial compression test on reduced-scale clay units

Source: Author (2025)

Table 11 presents the results obtained from the axial compression tests, while Table 12 summarizes the characteristic compressive strength values.

4.2.1.3 Determination of dynamical elastic modulus

The impulse excitation technique is the methodology adopted in the non-destructive test for obtaining the dynamic elastic modulus of materials. In this characterization test, the test specimen is positioned steel wires connected to a rigid frame in order to simulate free–free boundary conditions. An impact is applied to the sample, and the acoustic response

Table 11 – Compressive strength of reduced-scale clay blocks

	Load (kN)	f_{bm} **(MPa)**
Mean	55.24	22.86
SD	12.15	5.03
COV(%)	22	22

Source: Author (2025)

Table 12 – Characteristic compressive strength of reduced-scale clay blocks

f_{bm} (MPa)	22.86
$f_{bk,est}$ (MPa)	14.18
$\phi \times f_{b1}$ (MPa)	12.77
f_{bk} **(MPa)**	**14.18**

Source: Author (2025)

is captured by a directional acoustic sensor connected to a computer, as illustrated in Figure 23. The Sonelastic software mathematically processes the captured frequency by Fast Fourier Transform to obtain the frequency spectrum and identify the the peak corresponding to the first flexural mode (ALVES; OTANI, 2022).

Figure 23 – Schematic representation of acoustic tests

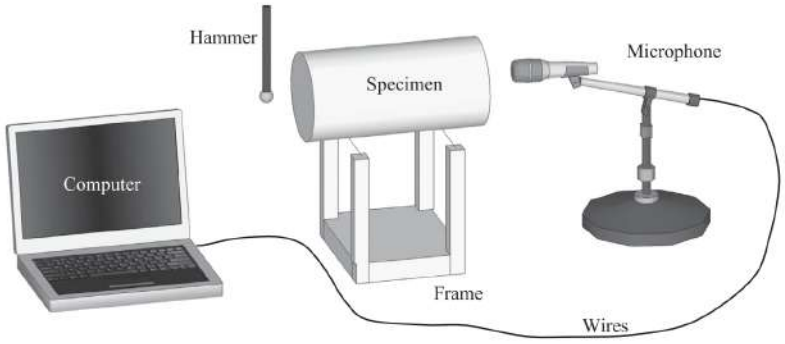

Source: Haach *et al.* (2013)

The American standard ASTM C215 (Americal Society for Testing and Materials, 2014) states that the dynamic elastic modulus can be determined based on the natural frequency of the first longitudinal mode (Eq. 4.2) or the flexural mode (Eq. 4.3).

$$E_{long} = DM(f_{1long})^2 \tag{4.2}$$

$$E_{flex} = CM(f_{1flex})^2 \tag{4.3}$$

Where M = mass (kg), f_{1long} = the first longitudinal mode (Hz), f_{1flex} = the first flexural mode (Hz) and C and D = geometrical constants. Although ASTM C215 is limited to prismatic and cylindrical concrete samples, studies by Santos *et al.* (2014) and Sombra and Haach (2022) demonstrated the successful application of the impulse

excitation technique to masonry units, yielding reliable estimates of their dynamic elastic modulus.

Following the methodology proposed in these studies, the geometric constant can be obtained through parametric analysis using numerical modeling. As previously discussed, the natural frequency of a body is directly related to its dynamic elastic modulus and mass through a shape-dependent geometric constant α (Eq. 4.4), assuming isotropic material behavior.

$$f_i = \alpha_i \sqrt{\frac{E}{M}} \tag{4.4}$$

In this approach, a specific vibration mode is selected, and a range of elastic modulus and density values are applied to the model. This generates a series of curves that relate natural frequency to variations in material properties. From these curves, a graph can be constructed showing the relationship between the elastic modulus and the product $M \times f^2$ for the selected values of E and M. The aforementioned studies confirmed that this relationship is linear, regardless of the values chosen for mass and modulus of elasticity. The slope of the resulting line is directly proportional to the geometric constant α, making it possible to determine the dynamic elastic modulus of the block using Eq. 4.5.

$$E = \beta M f^2 \tag{4.5}$$

Where β is a geometric parameter defined as $1/\alpha^2$. With the geometric constants determined and the vibration modes estimated, the final step involves conducting the acoustic test to collect the resonant frequencies.

The numerical simulation of the blocks used in this study was performed using ABAQUS software, version 6.26. A distinct model was developed for each block typology, with dimensions defined based on the dimensional analysis. To conduct the modal analysis, it is necessary to provide material properties related to mass and stiffness, namely density, Poisson's ratio, and elastic modulus. Table 13 presents the parameters adopted for the simulations. It is important to note that the Poisson's ratio values were obtained from the literature (Sombra, 2020), while the elastic modulus was estimated based on the Eurocode 6 (European Committee for Standardization, 2005), which states that, in the absence of experimental data, the elastic modulus may be assumed as $E = K_E f_{bk}$, where K_E is equal to 1000.

Table 13 – Material properties used in the numerical modeling of the blocks

ID	E **(MPa)**	υ	ρ **(ton/mm³)**
Concrete block (BCO)	7036	0.23	$1.984e^{-}9$
Clay block (BCE)	14180	0.17	$1.649e^{-}9$

Source: Author (2025)

The finite element used in the numerical models was the eight-node brick element (C3D8). Each model was also partitioned into rectangular regions where possible, to improve mesh quality. Four levels of mesh refinement were tested. Since there are no analytical solutions available for the natural frequencies of the evaluated geometries, numerical convergence was assessed using the Δ factor, which measures the relative variation due to mesh refinement, as calculated by Equation 4.6.

$$\Delta = \left| \frac{f_1 - f_2}{f_2} \right| \tag{4.6}$$

Where f_1 and f_2 are the natural frequencies of a given vibration mode obtained from meshes composed of elements of the same type, with f_2 corresponding to the result from the most refined mesh. A total of 16 eigenvalues and eigenvectors were requested for each analysis in order to visualize the first 10 vibration modes, since the initial six correspond to rigid body motions due to the adopted free-free boundary condition. The mesh convergence study focused on the first natural frequency to compare the different discretizations. Table 14 presents the results of this analysis for each element size (s), along with the corresponding relative CPU time.

Table 14 – Mesh convergence study for the blocks models

	"BCO" Model				
	$s = 5$	$s = 2.5$	$s = 1.5$	$s = 1$	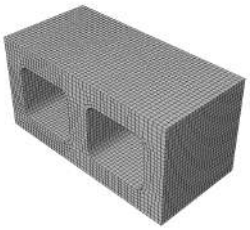
Elements	768	4560	21424	69578	
f_1 (Hz)	2805.3	2954.4	2999.3	3008.6	
Δ (%)	6.76	1.80	0.31	-	
t (s)	22	17	27	68	
	"BCE" Model				
	$s = 5$	$s = 2.5$	$s = 1.5$	$s = 1$	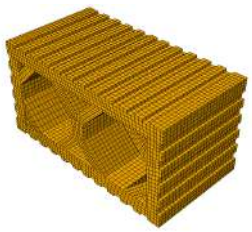
Elements	1664	4890	21450	63004	
f_1 (Hz)	4292.4	4734.3	5274.5	5324.9	
Δ (%)	19.39	10.95	0.95	-	
t (s)	20	17	30	61	

Source: Author (2025)

It is observed that with the adoption of finer meshes, the frequency values tend to stabilize, and the Δ value approaches zero. Although this analysis is not computationally expensive and does not require significant processing time, an element size of $s = 1.5$ was selected for the two models. Once the models were completed, the first ten natural frequencies and their corresponding mode shapes were extracted and are presented in Figures 24 and 25.

The next step in determining the geometric coefficients involved performing a parametric analysis. For each numerical model, five distinct values were assigned to both

Figure 24 – Estimated mode shapes and natural frequencies: concrete block

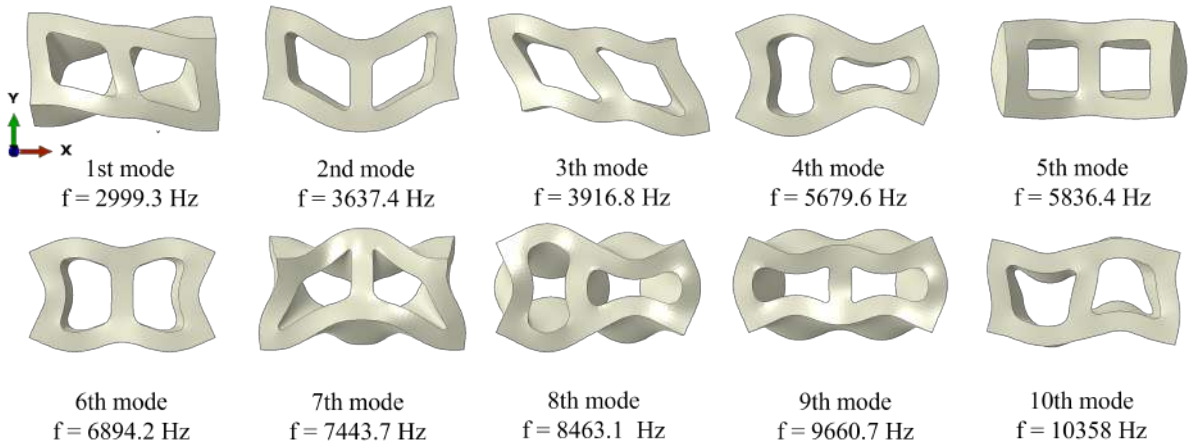

Source: Author (2025)

Figure 25 – Estimated mode shapes and natural frequencies: clay block

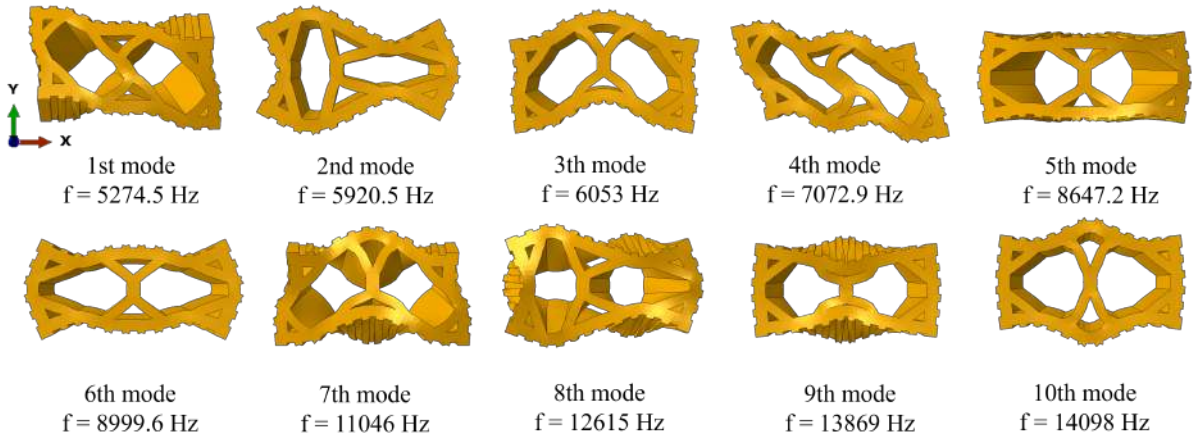

Source: Author (2025)

the material density and the dynamic elastic modulus, resulting in 25 unique parameter combinations. To illustrate this procedure, Figures 26 and 27 present the plots of elastic modulus versus natural frequency (arbitrarily defined) and elastic modulus versus the product of the assigned mass and the square of the frequency.

The graphs on the right confirm the expected linear behavior, since the coefficient of determination (R^2) is equal to the unit. The overlaid lines follow the equation $Mf^2 = aE$ where the slope "a" is numerically equal to $1/\beta$, as indicated by Eq. 4.5. From this relationship, the parameters α and β can be readily determined. Table 15 presents the geometric constants calculated for the first ten vibration modes of the two block typologies analyzed.

The observation of modal deformations also guided the definition of excitation and sensor point setups for the acoustic test, as well as in the arrangements prescribed

Figure 26 – Determination of geometric constants via parametric analysis: concrete block, 2nd mode

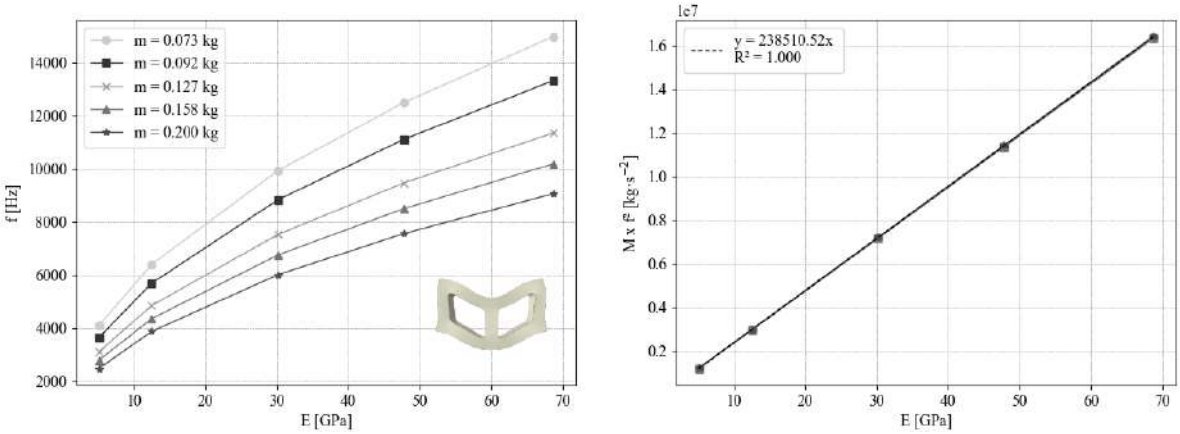

Source: Author (2025)

Figure 27 – Determination of geometric constants via parametric analysis: clay block, 4th mode

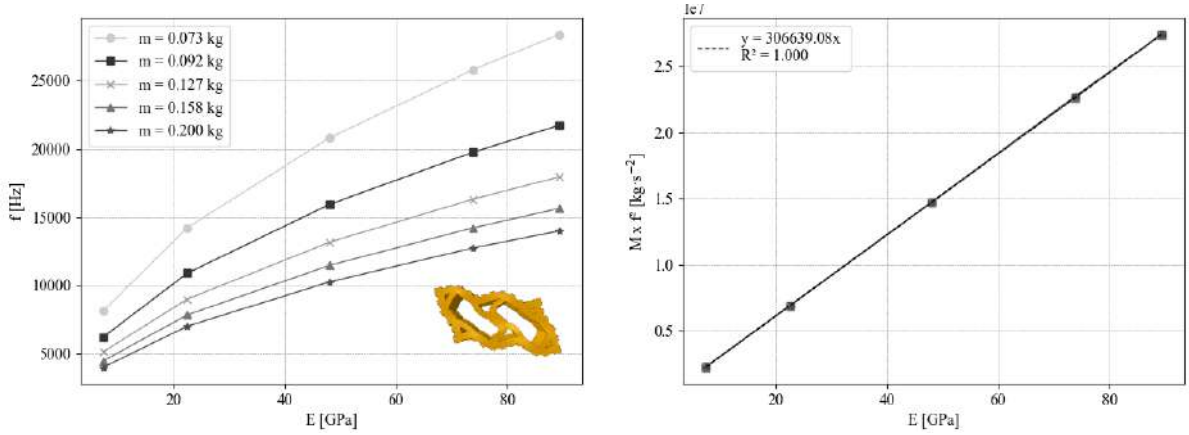

Source: Author (2025)

Table 15 – Geometric constants of the blocks

Mode Shape	Concrete block		Clay block	
	α	β	α	β
1	402.639	$6.168e^{-}6$	412.949	$5.864e^{-}6$
2	488.303	$4.194e^{-}6$	463.526	$4.654e^{-}6$
3	525.808	$3.617e^{-}6$	473.901	$4.453e^{-}6$
4	762.426	$1.720e^{-}6$	553.742	$3.261e^{-}6$
5	783.499	$1.629e^{-}6$	676.988	$2.182e^{-}6$
6	925.501	$1.167e^{-}6$	704.579	$2.014e^{-}6$
7	999.263	$1.001e^{-}6$	864.761	$1.337e^{-}6$
8	1136.121	$7.747e^{-}7$	987.636	$1.025e^{-}6$
9	1296.873	$5.946e^{-}7$	1085.788	$8.482e^{-}7$
10	1390.507	$5.172e^{-}7$	1103.774	$8.208e^{-}7$

Source: Author (2025)

by Americal Society for Testing and Materials (2022). As illustrated in Figure 28, the numerical model (Figure 28a) highlights the highest displacement amplitudes in red/orange and nodal points in blue. Therefore, the optimal arrangement involves supporting the specimen at nodal points (low amplitude) and applying the impact and capturing the response at antinodes (high amplitude), as shown in Figure 28b. This procedure was performed for five different configurations to excite the first five vibration modes, as higher modes proved more challenging to detect.

Figure 28 – Example of a test configuration based on numerical modal analysis

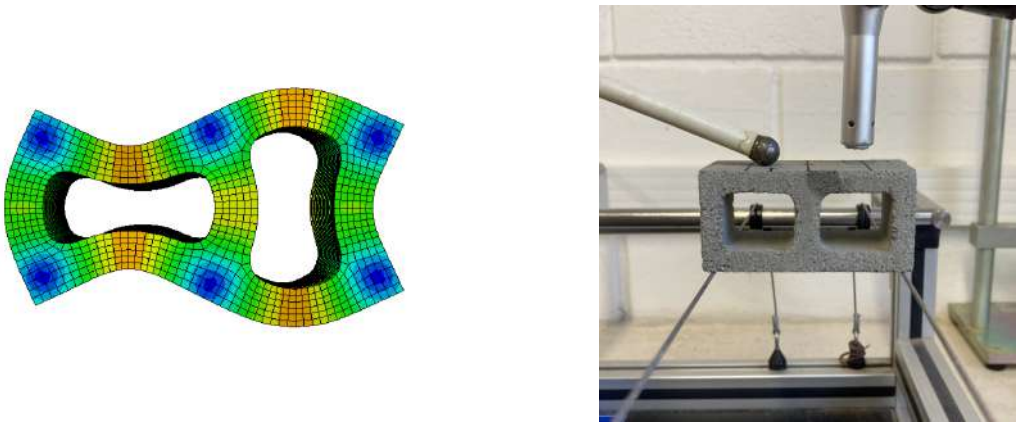

(a) (b)

Source: Author (2025)

The input parameters used in the Sonelastic software followed those adopted by Sombra (2020), namely: acquisition time = 0.683 s; processing time = Position 5; sensitivity = 0.025; detection filter = Standard [0.5 kHz – 20 kHz]. The first two parameters are recommended by ATCP – the software provider – for testing ceramic materials and materials with low damping.

The dynamic elastic moduli of the studied blocks were calculated based on the experimentally obtained natural frequencies and the geometric coefficients determined through numerical modeling. Table 16 presents the natural frequencies captured through acoustic testing while Table 17 the specimen weights and the resulting dynamic elastic modulus values for the concrete blocks specimens. Tables 18 and 19 provides the corresponding data for the clay blocks. For the individual experimental results, a Grubbs test with a 5% significance level was conducted, which led to the exclusion of the data corresponding to specimen "CE-1." Consequently, this specimen was not considered in the calculation of the mean, standard deviation, or coefficient of variation for both the frequency data and the dynamic elastic modulus.

As previously explained, the test setups were designed to facilitate the detection of the different vibration modes. For the concrete blocks, a comparison between Figure 24 and Table 16 shows that the predicted sequence of vibration modes matched the experimental

Table 16 – Experimental frequencies of concrete blocks. Values in Hertz

	f_1 **- Tors. X**	f_2 **- Bend. Z**	f_3 **- Long.**	f_4 **- Bend. Z**	f_5 **- Bend. Y**
CO-1	4669.5	5333.2	5859.7	8442.4	9476.0
CO-2	4743.0	5437.9	6041.7	8653.4	9578.4
CO-3	4554.8	5175.1	5646.2	8364.2	9048.1
CO-4	4530.8	5183.0	5739.6	8302.0	*
CO-5	4619.7	5274.3	5627.2	8270.1	*
CO-6	4731.2	5437.0	5893.0	8562.2	*
Mean	**4641.5**	**5306.8**	**5801.2**	**8432.4**	**9367.5**
SD	88.74	117.12	159.88	150.84	281.32
COV(%)	1.91	2.21	2.76	1.79	3.00

* = Resonant frequency not identified experimentally

Source: Author (2025)

Table 17 – Dynamic elastic modulus of concrete blocks

	M (g)	E_{cd} (GPa) MS* 1	E_{cd} (GPa) MS 2	E_{cd} (GPa) MS 3	E_{cd} (GPa) MS 4	E_{cd} (GPa) MS 5
CO-1	134.6	18.10	16.06	16.72	16.50	19.69
CO-2	134.8	18.70	16.72	17.80	17.36	20.15
CO-3	135.7	17.36	15.24	15.65	16.33	18.10
CO-4	129.8	16.44	14.62	15.47	15.39	-
CO-5	138.6	18.25	16.17	15.87	16.31	-
CO-6	140.7	19.43	17.44	17.67	17.74	-
Mean	**135.25**	**18.05**	**16.04**	**16.53**	**16.60**	**19.61**
SD	3.75	1.04	1.01	1.03	0.84	1.08
COV(%)	2.77	5.78	6.29	6.22	5.06	5.57

* = Mode Shape

Source: Author (2025)

Table 18 – Experimental frequencies of clay blocks. Values in Hertz

	f_1 **- Bend. Z**	f_2 **- Tors. X**	f_3 **- Bend. Z**	f_4 **- Long.**	f_5 **- Bend. Y**
CE-1	3948.5	4206.7	4397.4	5371.0	6426.1
CE-2	4377.3	4636.0	4851.2	5919.5	7057.8
CE-3	4477.4	4725.0	4983.1	6026.2	7164.8
CE-4	4355.5	4614.0	4861.2	5892.9	*
CE-5	4486.5	4734.0	5003.2	6045.2	*
CE-6	4627.0	4840.9	5150.0	6181.8	*
Mean	**4710.0**	**4464.7**	**4969.7**	**6013.2**	**7111.3**
SD	90.30	107.89	122.09	114.97	75.63
COV(%)	1.92	2.42	2.46	1.91	1.06

* = Resonant frequency not identified experimentally

Source: Author (2025)

Table 19 – Dynamic elastic modulus of clay blocks

	M (g)	E_{cd} (GPa) MS 1	E_{cd} (GPa) MS 2	E_{cd} (GPa) MS 3	E_{cd} (GPa) MS 4	E_{cd} (GPa) MS 5
CE-1	82.4	5.98	8.55	7.09	7.75	7.42
CE-2	88.1	7.86	11.10	9.23	10.07	9.58
CE-3	88	8.21	11.52	9.73	10.42	9.86
CE-4	86.9	7.67	10.85	9.14	9.84	-
CE-5	85.9	8.05	11.29	9.57	10.24	-
CE-6	89.3	8.90	12.27	10.55	11.13	-
Mean	**87.64**	**8.14**	**11.41**	**9.65**	**10.34**	**9.72**
SD	1.29	0.47	0.54	0.56	0.49	0.20
COV(%)	1.47	5.79	4.76	5.79	4.74	2.05

Source: Author (2025)

observations. However, the predicted natural frequencies were consistently higher, which suggests that the elastic modulus adopted in the simulation was underestimated.

In contrast, for the clay blocks, the comparison between Figure 25 and Table 18 showed that the first experimental mode corresponded to the first bending mode along the z-axis, while the second experimental mode was the first torsional mode along the x-axis. This order is reversed when compared to the numerical study (see Figure 25). This discrepancy between the experimental and numerical results may be attributed to the unique geometric characteristics of the clay block, as well as to potential material anisotropy. Nevertheless, the geometric coefficients used to compute the dynamic elastic modulus were selected based on the corresponding mode shapes, ensuring a consistent comparison. Additionally, the experimentally obtained natural frequencies were lower than the predicted values, indicating that, unlike in the case of the concrete block, the elastic modulus was overestimated in the simulation.

The average value of the dynamic elastic modulus obtained for the concrete blocks was 17.31 GPa, with a standard deviation of 1.34 GPa and a coefficient of variation of 7.78%. For the clay blocks, the average E_{cd} determined using the same methodology was 9.85 GPa, with a standard deviation of 1.19 GPa and more scattered results, as indicated by a higher CoV of 12.08%.

4.2.2 Mortar

The mortars used in this study were produced using CSN Portland cement class 32 (CPII F-32), Itaú type CH-III hydrated lime, and medium-grained sand with fineness modulus of 1.38 and a maximum diameter of 2.4mm. For mortar preparation, the volumetric mix ratios were converted to mass-based proportions, with the unit masses adopted from the work of Silva (2014), since a detailed investigation of the mortar properties is beyond the scope of this research. The selection of two distinct mix designs was based on Table 4

of ABNT NBR 13281-2:2023 (Associação Brasileira de Normas Técnicas, 2023a), which establishes the compressive strength classes for inorganic mortars used in the laying of load-bearing units as a function of the block's characteristic strength. The volumetric compositions of the mortars were selected based on the study by Haach, Vasconcelos and Lourenço (2011) and are presented in Table 20. In this table, mix ARG-CO corresponds to the mortar used for laying concrete blocks, whereas mix ARG-CE refers to the mortar employed for laying clay blocks.

Table 20 – Volumetric composition of mortars

Mix	**Cement class**	**Cement**	**Lime**	**Sand**	**a/c**
ARG-CO	CP II F - 32	1	0.5	4.5	1.5
ARG-CE	CP II F - 32	1	0.25	3	0.8

Source: Author (2025)

To determine the dynamic elastic modulus (E_{cd}), compressive strength (R_c), and flexural tensile strength (R_f), six prismatic specimens measuring 4 × 4 × 16 cm were cast for each mortar mix, in accordance with the recommendations of ABNT NBR 13279:2005 (Associação Brasileira de Normas Técnicas, 2005). Two days after casting, the specimens were demolded and subsequently stored in a curing chamber. All tests were conducted 28 days after casting. The average density of the mortars was $\rho = 2.11$ g/cm^3 for the ARG-CO mix and $\rho = 2.12$ g/cm^3 for the ARG-CE mix.

The dynamic elastic modulus of the mortars was determined using the impulse excitation technique (Figure 29a), with the Sonelastic system automatically calculating E_{cd} for prismatic and cylindrical specimens. Flexural tensile strength tests were performed using a loading device (Figure 29b), with a load rate of 50 N/s applied through a servo-hydraulic testing machine until specimen failure. The two halves resulting from the flexural tests were subsequently used for axial compression testing (Figure 29c), applying a load rate of 500 N/s.

Figure 29 – Mechanic characterization tests on mortar samples

(a) Impact acoustic test (b) Flexural strength test (c) Compressive strength test

Source: Author (2025)

Table 21 presents the average values obtained from the mechanical characterization of the mortar. The Grubbs test was applied to analyze the individual values, and for the ARG-CE mix, the highest value obtained in the compression test was excluded. Additionally, according to NBR 13279:2005, when the maximum deviation of the flexural tensile strength exceeds 0.3 MPa, a new average should be calculated, excluding the discrepant value. Therefore, to validate the flexural tensile strength results for the ARG-CE mix, three out of the six individual values were discarded to comply with the normative criterion.

Table 21 – Mechanical properties of the mortar mixes

	ARG-CO mix			**ARG-CE mix**		
	E_{cd}(GPa)	R_f(MPa)	R_c(MPa)	E_{cd}(GPa)	R_f(MPa)	R_c(MPa)
Mean	11.84	1.71	4.55	21.35	3.06	10.72
SD	0.386	0.134	0.160	0.682	0.118	0.216
COV(%)	3.25	7.86	2.95	3.20	3.84	2.01

Source: Author (2025)

By comparing the results presented in Tables 5, 11, and 21, it can be inferred that the ratio between the mortar strength and the block strength is 39.67% for the clay blocks and 93.46% for the concrete blocks. According to Ramalho and Corrêa (2003), this ratio only begins to negatively affect the masonry performance when it is below 30%. Therefore, the obtained values are within the limits considered suitable.

A different mortar mix was developed specifically for casting the bearing and top slabs. The decision to use a mortar mix was driven by the small cover thicknesses required at the chosen scale. To achieve the target characteristic compressive strength of 30 MPa, a volumetric mix ratio of 1:3:0.4 (CP V ARI Portland cement : natural silica sand : water) was adopted, with the addition of a superplasticizer at 1% of the cement mass to enhance the workability of the mixture. This proportion was tested in the laboratory to determine its compressive strength and dynamic elastic modulus. The molded specimens achieved a dynamic modulus of elasticity (E_{cd}) of 36.19 GPa, a characteristic compressive strength of 37.06 MPa, and an average density of $\rho = 2.14$ g/cm^3.

However, during the actual casting process, it was observed that the consistency of the mixture was still insufficiently fluid. As a result, the superplasticizer dosage was increased to 2%. The specimens molded with this adjusted mix exhibited significantly lower mechanical properties, with $E_{cd} = 12.28$ GPa and $\rho = 1.60$ g/cm^3. To assess the in-situ performance of the hardened slabs, a rebound hammer test was conducted in accordance with ABNT NBR 7584:2012 (Associação Brasileira de Normas Técnicas, 2012). Fifteen impact points were tested on each slab, yielding an average compressive strength of 15.1 MPa. Although this result fell short of the initial design target, it was considered satisfactory for the intended function of the element and the objectives of the experimental campaign.

4.2.3 Masonry

The experimental characterization encompassed not only the individual masonry components but also the evaluation of the mechanical behavior of the composite material. For this purpose, 12 ungrouted hollow prisms, each composed of two blocks, were assembled in the laboratory using the concrete and clay blocks and the mortar mixes described in previous sections. All prisms were constructed by a single operator using a trowel and a level. According to ABNT NBR 16868-3:2020 (Associação Brasileira de Normas Técnicas, 2020b), the mortar joint thickness must be 10 ± 3 mm, which corresponds to 2 ± 0.6 mm in the 1:5 reduced scale adopted in this study. However, achieving such a reduced thickness, particularly for the vertical joints, proved to be extremely challenging. Therefore, 3-mm plastic spacers were employed to ensure better control over the joint thickness. The prisms were stored under laboratory conditions for a curing period of 28 days.

The compressive strength tests were conducted using the same hydraulic press employed in the previous experiments. The top and bottom surfaces of the prisms were leveled with a thin layer of cement paste to minimize stress concentrations at the primary load application points. In accordance with ABNT NBR 16868-3:2020, two cycles of loading and unloading were performed up to 50% of the estimated ultimate load. To determine the elastic modulus, deformations were measured using two 50 mm clip-gages positioned at the center of opposite external faces of the prisms, as illustrated in Figure 30.

Figure 30 – Instrumentation of prisms for compression testing

Source: Author (2025)

The average compressive strength of the two-block prisms is presented in Table 22, along with the Efficiency Factor (η) – which evaluates the ratio between the prism's compressive strength and that of the corresponding individual block. According to Ramalho and Corrêa (2003), the Efficiency Factor typically ranges from 0.5 to 0.9 for concrete blocks and from 0.3 to 0.6 for clay blocks. Based on these reference values and the results, the tested specimens fall within the expected efficiency range for each material type.

Table 22 – Mechanical properties of the reduced-scale prisms

	Concrete block		**Clay block**	
	E_m **(GPa)**	f_{pm} **(MPa)**	E_m **(GPa)**	f_{pm} **(MPa)**
Mean	6.41	9.39	5.19	8.43
SD	2.48	2.27	0.71	2.19
COV(%)	38.72	24.16	13.71	25.92
η	0.819		0.369	

Source: Author (2025)

Table 22 also reports the static elastic modulus (E_m), determined in accordance with the criteria established by ACI 530-05 (American Concrete Institute, 2005), which specifies that E_m should be calculated from the linear portion of the stress–strain curve (Figure 31), between 5% and 33% of the prism's ultimate compressive strength. Furthermore, the characteristic compressive strength of the prisms (f_{pk}) was determined and is presented in Table 23.

Figure 31 – Stress-strain diagrams of the two-block prisms

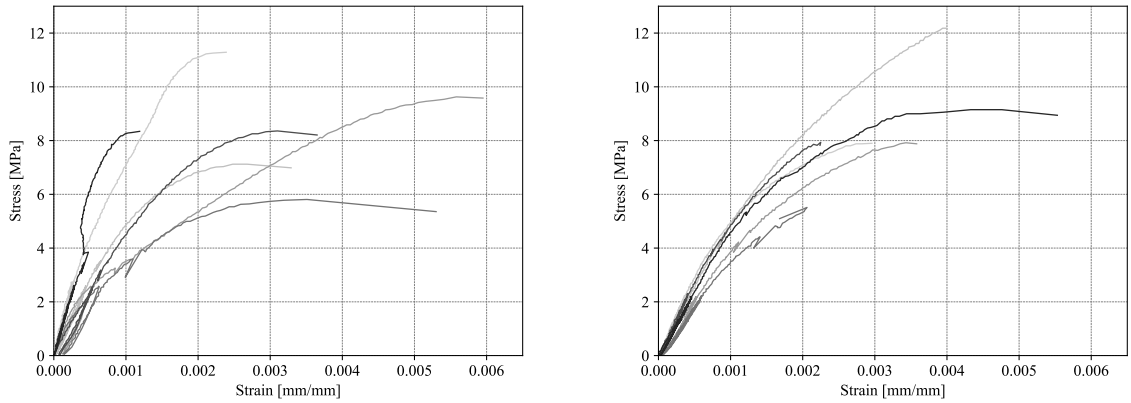

(a) Concrete prisms (b) Clay prisms

Source: Author (2025)

Table 23 – Characteristic compressive strength of reduced-scale prisms

	Concrete block	**Clay block**
f_{pm} (MPa)	9.39	8.43
$f_{pk,est}$ (MPa)	5.79	5.49
$\phi \times f_{p1}$ (MPa)	5.17	4.91
f_{pk} **(MPa)**	**5.79**	**5.49**

Source: Author (2025)

4.3 Laboratory static tests on masonry walls

Quasi-static cyclic tests were conducted on the masonry wall specimens to induce controlled and progressive structural damage. For each panel, four distinct damage states were defined, each corresponding to an incremental level of lateral loading. These stages were designed to activate cracking mechanisms associated with both flexural and shear behavior. A typical experimental setup for masonry subjected to monotonic or cyclic lateral loading is presented in Figure 32. As shown, the resulting internal forces distribution reflects cantilever-like behavior. A key experimental challenge associated with this configuration is the mitigation of rotational restraint at the top of the wall, which is essential to avoid artificial stiffness contributions (Haach, 2009).

Figure 32 – Typical shear test configuration and internal forces distribution

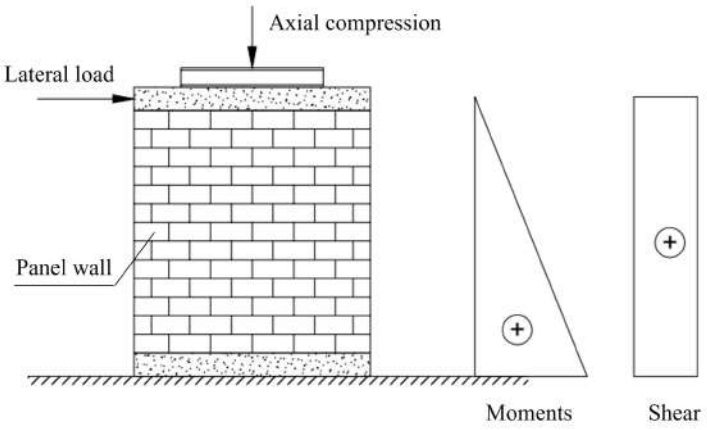

Source: Adapted from Haach (2009)

The following describes the configuration and procedures implemented in the experimental phase focused on damage progression.

4.3.1 Construction of specimens

The masonry specimens were assembled in a laboratory environment by the author, using the components described in Section 4.2. The wall specimens were constructed on reinforced mortar slabs, which served both as a base and for transportation. Additional reinforced mortar slabs were placed on top of the panels to ensure proper distribution of vertical and horizontal loads.

Each slab was built using the same reinforcement: a ribbed welded wire mesh of type Q113, featuring a 10 × 10 cm grid and CA60 steel wires with a diameter of 3.8 mm. The mesh was embedded at mid-depth within the 4 cm-thick slabs – equivalent to 20 cm in a full-scale model. Hooks were attached to the ends of the panels, as illustrated in Figure 33.

Figure 33 – Post-casting view of the reinforced mortar slabs

Source: Author (2025)

To ensure consistency during the panel construction and to minimize workmanship-related variations, a custom aluminum frame was used. It consisted of a vertical ruler marked with the height of each masonry course and a horizontal guide for controlling alignment and plumb, both of which were checked at every course. A thin mortar bed was applied at the base to initiate construction, and 3 mm plastic spacers were inserted between blocks to maintain consistent vertical joints, all of which were fully filled with mortar. Bed joints were formed by applying mortar to both the shells and webs of the masonry units. Figure 34 shows key steps in the wall construction process, from the placement of the first layer of blocks (Figure 34a) to the completed wall (Figure 34b), highlighting the importance of using the alignment frame.

The walls were cured in a controlled laboratory environment for 28 days. After proper curing of the specimens, the top slab was positioned and bonded using epoxy adhesive. An additional important aspect was the construction of custom wooden frames to ensure the integrity of the panels and provide out-of-plane bracing during the placement of the top slabs and transportation. As shown in Figure 35, an overhead crane was used to position the panels beneath the reaction frame. This stage was carried out with great care to avoid damaging the specimens or causing the total loss of the models.

4.3.2 Final setup and procedures

The test setup adopted for the shear test is shown in Figure 36, following the typical configuration in which the wall is subjected to a combination of vertical and horizontal loads. The bottom slab was leveled with a thin layer of sand and fixed using steel beams to prevent uplift and sliding at the base. The vertical axial load was applied using a hydraulic cylinder connected to the reaction frame and distributed through a stiff steel beam, while

Figure 34 – Details of the wall construction at reduced scale

(a) First masonry course – Concrete block wall (b) Final result – Clay block wall

Source: Author (2025)

Figure 35 – Handling with overhead crane and detail of the wooden support system

Source: Author (2025)

the lateral load was applied by a separate hydraulic cylinder anchored to an independent support structure.

Figure 36 – Test setup for in-plane cyclic horizontal load

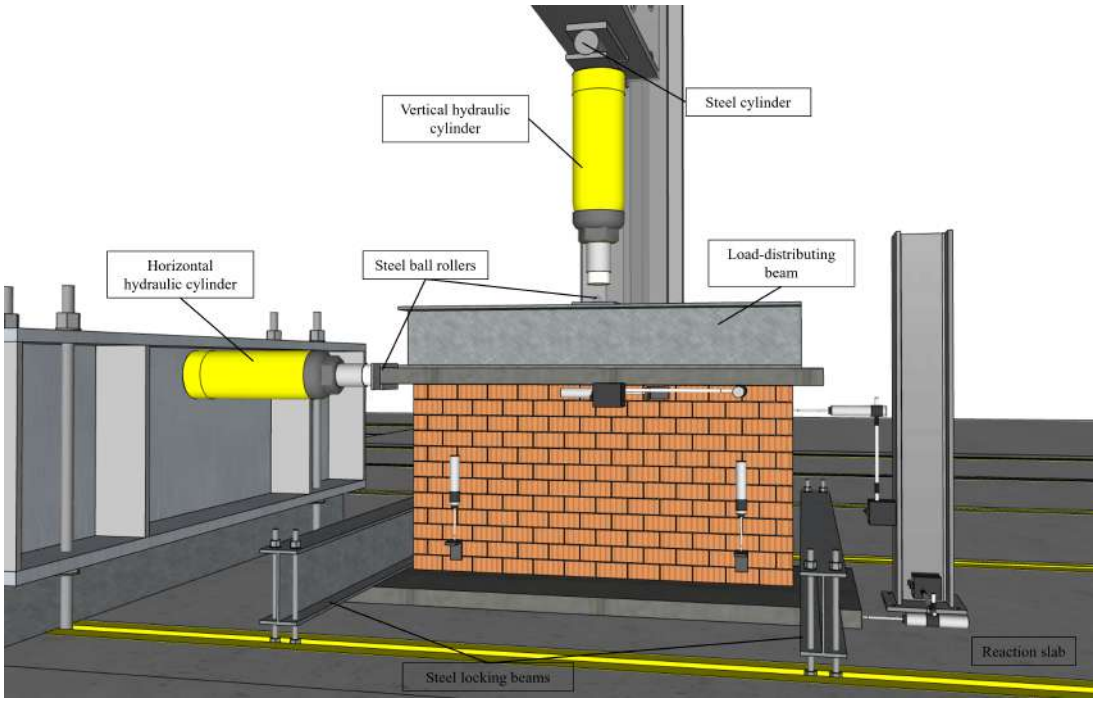

Source: Author (2025)

An important aspect of this setup is the boundary conditions. As represented in Figure 36, steel spheres were placed between the actuator and the top slab (Figure 37a), as well as between the actuator and the distributing beam (Figure 37b), in order to create a roller-type constraint. To connect the vertical hydraulic cylinder to the reaction frame, a device was installed to allow rotation only in the plane of the wall (Figure 37c). This articulated-type connection at both ends of the vertical actuator minimizes external constraints and permits horizontal displacement of the wall. It is also relevant to note that, after the application of the axial load, the nuts at the ends of the tie rods supporting the vertical actuator were loosened to allow rotation of the actuator about its base.

One of the observed aspects of the test planning concerns the influence of the level of pre-compression applied to the masonry panels. Given this, different levels of pre-compression stress were defined in this study based on varying percentages of the maximum service axial stress resulting only from compressive forces, aiming to represent typical limits found in building structures. In this context, the allowable compressive stress (f_m) can be calculated, according to NBR 16868-1:2020 (Associação Brasileira de Normas Técnicas, 2020a), using the Eq. 4.7:

$$\gamma_f \cdot f_m = \frac{0.7 \cdot f_{pk}}{\gamma_m} R \tag{4.7}$$

Figure 37 – Control of boundary conditions during the test

(a) Horizontal actuator–top slab connection (b) Vertical actuator–panel connection (c) Vertical actuator–reaction frame connection

Source: Author (2025)

Where f_{pk} is the characteristic strength of the prism, and the partial safety factors γ_m and γ_f are typically taken as 2.0 and 1.4, respectively. R is the strength reduction factor accounting for wall buckling, calculated using the following expression (Eq. 4.8):

$$R = \left[1 - \left(\frac{h_{ef}}{40 \cdot t_{ef}}\right)^3\right] \tag{4.8}$$

The parameters h_{ef} and t_{ef} correspond to the effective height and effective thickness, respectively. The effective height is equivalent to the buckling length in classical structural mechanics and depends on the wall's support conditions and actual height. The effective thickness is a simplified representation of the radius of gyration used in buckling calculations. In the absence of stiffeners, it is taken as the wall's actual thickness. For the models constructed in this study, average height values were obtained from measurements taken after panel construction. The resulting values of these parameters are presented in Table 24.

Table 24 – Geometric parameters used in the buckling reduction factor calculation

Model	h_{ef} (mm)	t_{ef} (mm)	R	$\lambda = h_{ef}/t_{ef}$
PCO	497.83	38.57	0.97	12.90
PCE	497.17	34.57	0.95	14.37

Source: Author (2025)

Considering the characteristic prism strengths of $f_{pk} = 5.79$ MPa for the concrete block masonry and $f_{pk} = 5.49$ MPa for the clay block masonry, and adopting a partial safety factor $\gamma_m = 1.0$ to obtain more realistic estimations, the resulting admissible compressive stress values for the masonry are presented in Table 25.

The stress values for the net area were obtained by dividing those for the gross area by the coefficients 0.57 for concrete block masonry and 0.44 for clay block masonry,

Table 25 – Admissible compressive stress values for masonry

Model	**Compressive stress (MPa)**	
	A_{gross}	A_{net}
PCO	2.79 (103.65 kN)	4.89 (181.84 kN)
PCE	2.61 (88.44 kN)	5.93 (201.00 kN)

Source: Author (2025)

according to the net-to-gross area ratio. Since the values of f_m refer to the highest estimated pre-compression intensity, three distinct pre-compression levels were defined for this study—corresponding to 30%, 50%, and 70% of the calculated admissible stress. These levels were designated as Series A, B, and C, respectively.

The analysis of horizontal loading considers the shear stresses in masonry walls, which follow the Coulomb failure criterion ($\tau = \tau_0 + \mu\sigma$). The Brazilian standard NBR 16868-1:2020 (Associação Brasileira de Normas Técnicas, 2020a) defines the characteristic shear strength along the horizontal joints of masonry walls (f_{vk}) as a function of the average compressive strength of the mortar (f_a) and the level of pre-compression ($\mu\sigma$), using a friction coefficient of $\mu = 0.5$, as indicated in Table 26.

Table 26 – Characteristic shear strength (f_{vk}) in horizontal joints according to NBR 16868-1:2020

	Average compressive strength of mortar (MPa)		
	1.5 to 3.4	3.5 to 7.0	Above 7.0
f_{vk}	$0.10 + 0.5\sigma \leq 1.0$	$0.15 + 0.5\sigma \leq 1.4$	$0.35 + 0.5\sigma \leq 1.7$

σ is the normal stress considering 90% of the characteristic value of permanent loads.

Source: Author (2025)

The adopted normal stress values are the same as those used for pre-compression. For the models constructed in this study and their corresponding series, the calculated shear resistance values are presented in Table 27.

Table 27 – Shear resistance values calculated for the constructed models and their equivalent series

Model	f_a (MPa)	σ(MPa)	f_{vk} (MPa)
PCO-A	4.55	0.837 (31.09 kN)	0.53 (13.93 kN)
PCO-B	4.55	1.395 (51.82 kN)	0.78 (20.58 kN)
PCO-C	4.55	1.950 (72.56 kN)	1.03 (27.19 kN)
PCE-A	10.72	0.783 (26.53 kN)	0.70 (16.95 kN)
PCE-B	10.72	1.306 (44.22 kN)	0.94 (22.63 kN)
PCE-C	10.72	1.827 (61.91 kN)	1.17 (28.30 kN)

Source: Author (2025)

For each series, the test procedure was conducted in three phases. In the first phase, a **vertical pre-load** corresponding to approximately 10% of the compressive strength (based on the gross area) was applied in two cycles to promote model accommodation. The second phase involved **applying the target vertical stress** corresponding to the selected pre-compression level, which was kept constant throughout the test. In the third phase, a **horizontal load was applied with a linearly increasing magnitude**, corresponding to fractions of the estimated shear resistance, in order to establish the damage scenarios. The applied forces (together with the load-distributing beam) were removed after each damage stage to allow for subsequent modal identification analysis.

4.3.3 Instrumentation

To measure the static response of the physical models, a set of six LVDTs – with measurement range up to 25mm – and two load cells were arranged as indicated in Figure 38. The readings were collected using an electronic data acquisition system. LVDT 1 is intended to monitor the out-of-plane displacement of the panel during testing. LVDTs 2 and 6 are positioned to measure potential slip between the top slab and the panel, and between the base slab and the laboratory reaction floor, respectively. LVDT 3 captures the global lateral deformation of the panel, while LVDTs 4 and 5 measure axial strains along the wall. LVDTs 1, 3, and 6 are mounted on independent steel support structures, decoupled from the reaction frame.

Figure 38 – Instrumentation of the walls – location of the LVDTs

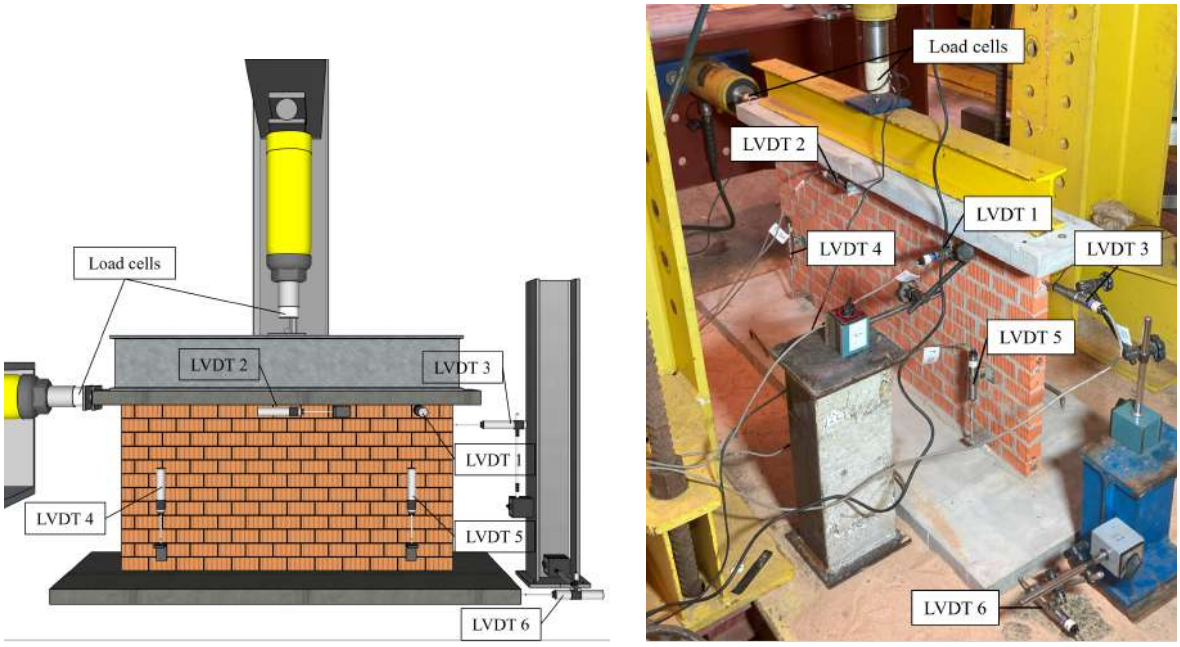

(a) Schematic of the instrumentation layout (b) Instrumentation as recorded during the test

Source: Author (2025)

4.4 Modal identification tests on masonry walls

This section presents the methodology adopted for modal identification using output-only data, carried out after each damage stage. The identification was first performed on the undamaged models and then repeated after each damage increment. It is important to note that the load-distributing beams were removed to avoid the influence of additional mass. The numerical model is presented first, followed by a discussion of the test planning approach.

4.4.1 Numerical estimation of modal parameters

According to Reynolds and Pavic (2000), the experimental modal analysis of structures can be broken down into four phases: preparation, exploratory phase, measurement, and estimation of modal parameters. The first phase involves defining the test objectives, identifying necessary resources, and creating a numerical model of the structure to determine probable dynamic properties. This modeling will also be crucial in analyzing the results. Initially, the model – typically developed using finite elements – doesn't need to be highly detailed or computationally expensive. A simplified model can already significantly contribute to accelerometer placement, determine the location of the reference accelerometer, and provide information about the probable frequency ranges of interest (Reynolds; Pavic, 2000).

The initial numerical model for this study was developed using the finite element software ABAQUS (version 6.26), employing eight-node linear brick elements (C3D8). A three-dimensional modeling approach was chosen to enable the estimation of all vibration modes. At this preliminary stage, the masonry panels were modeled as homogeneous and isotropic solids. The geometry consisted of two distinct parts: the masonry panel and the top slab. The bottom boundary was considered fully constrained.

In the homogenized masonry models, the elastic modulus considered was the static modulus obtained from the prism test, while the density was determined from measurements of the dimensions and mass of masonry wallettes specimens. The Poisson's ratio was adopted from values reported in the literature. Table 28 summarizes the material properties used in the simulations.

Table 28 – Material properties used in the numerical modeling of the wall specimens

Material	E **(MPa)**	υ	ρ **(ton/mm³)**
Concrete masonry	6410	0.23	$1.389e^{-}9$
Clay masonry	5190	0.17	$1.212e^{-}9$
Top slab	12280	0.20	$1.600e^{-}9$

Source: Author (2025)

A mesh convergence study was carried out following a procedure similar to that

described in Section 4.2.1.3. Four levels of mesh refinement were tested for the masonry portion, while the top slab retained the same element size in both models to isolate the analysis to the masonry component. The first 15 eigenvalues were computed, and the first mode was used as a reference for comparing the different mesh discretizations. As shown in Table 29, the relative difference (Δ) in the third refinement level dropped below 2%, indicating convergence of the results. Based mainly on the estimated errors, an element size of $s = 5$ was adopted for the concrete block walls and $s = 7.5$ for the clay block walls.

Table 29 – Mesh convergence study for the masonry panels

	Concrete block wall model				
	$s = 15$	$s = 10$	$s = 7.5$	$s = 5$	
Elements	6144	18432	40960	147456	
f_1 (Hz)	32.19	33.05	33.44	33.86	
Δ (%)	4.91	2.37	1.23	-	
t (s)	19	31	37	122	
	Clay block wall model				
	$s = 15$	$s = 10$	$s = 7.5$	$s = 5$	
Elements	4096	13824	40960	129024	
f_1 (Hz)	23.22	25.24	26.22	26.42	
Δ (%)	12.11	4.44	0.75	-	
t (s)	21	22	37	118	

Source: Author (2025)

Figure 39 presents the frequency values and corresponding mode shape configurations for the first fifteen vibration modes of the concrete block walls. The frequency range spans from 33.86 Hz to 837.51 Hz. Among these modes, only the 6th, 12th, and 13th exhibit in-plane behavior, associated with higher frequency values, whereas the remaining modes correspond to out-of-plane deformations.

Figure 40 presents the corresponding frequency values and mode shape configurations for the clay block walls. Compared to the concrete block walls, the frequencies are slightly lower, ranging from 26.22 Hz to 763.82 Hz. The in-plane modes are the same as those observed in the previous model; however, the order of the in-plane bending modes—specifically the 4th, 5th, 14th, and 15th—has changed.

4.4.2 Testing equipment and configuration

To monitor the dynamic response of the structure, seven uniaxial piezoelectric accelerometers from Brüel & Kjær were employed: five units of model 4533-B-002 (sensitivity of 490 mV/g, frequency range 0.2 Hz–12.8 kHz) and two units of model 8344 (sensitivity of 2500 mV/g, frequency range 0.2 Hz–3 kHz). The accelerometers were connected via ultra-low-noise Brüel & Kjær AC-0005-N coaxial cables to a data acquisition system com-

Figure 39 – Numerical modal estimation for the concrete block wall. Only the masonry is presented

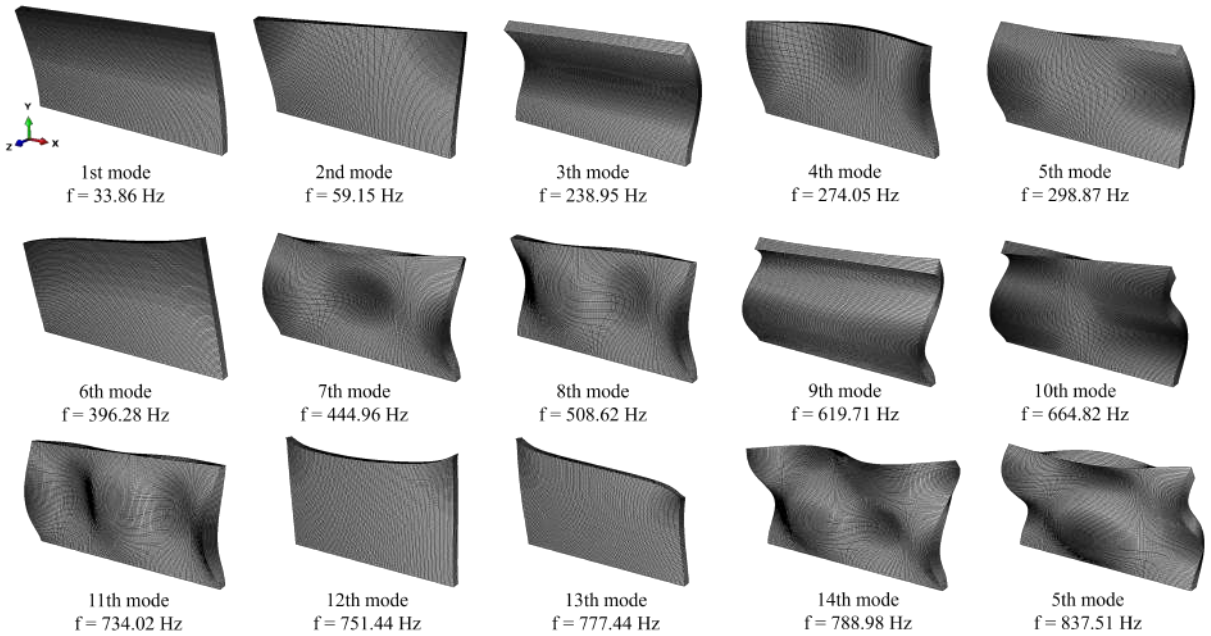

Source: Author (2025)

Figure 40 – Numerical modal estimation for the clay block wall. Only the masonry is presented

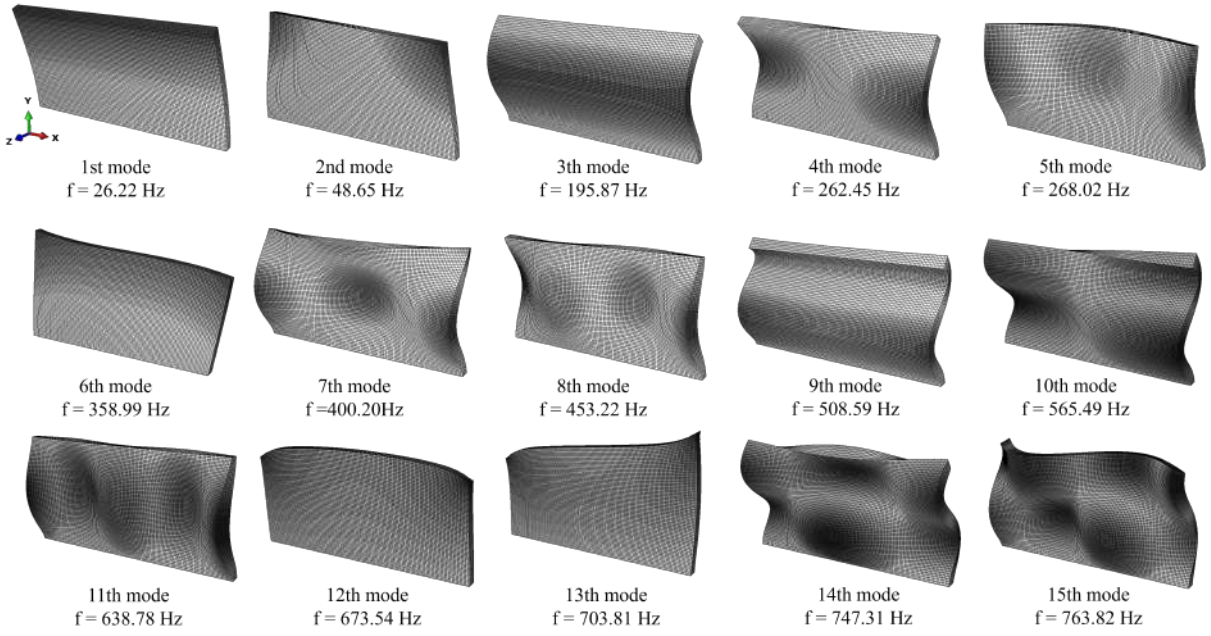

Source: Author (2025)

prising three NI 9232 modules housed in a NI cDAQ-9174 chassis (National Instruments), providing a total of nine analog input channels.

Signal acquisition was carried out using LabVIEW SignalExpress software on a laptop, with a sampling frequency of 3000 Hz, selected based on preliminary numerical analysis and in accordance with the Nyquist theorem. To ensure the capture of all mode shapes identified in the finite element analysis, three accelerometer configurations were designed to measure accelerations in both the out-of-plane and in-plane directions. Figure 41 illustrates the location of the measurement points for each setup.

Figure 41 – Location of the measuring points for the dynamic tests

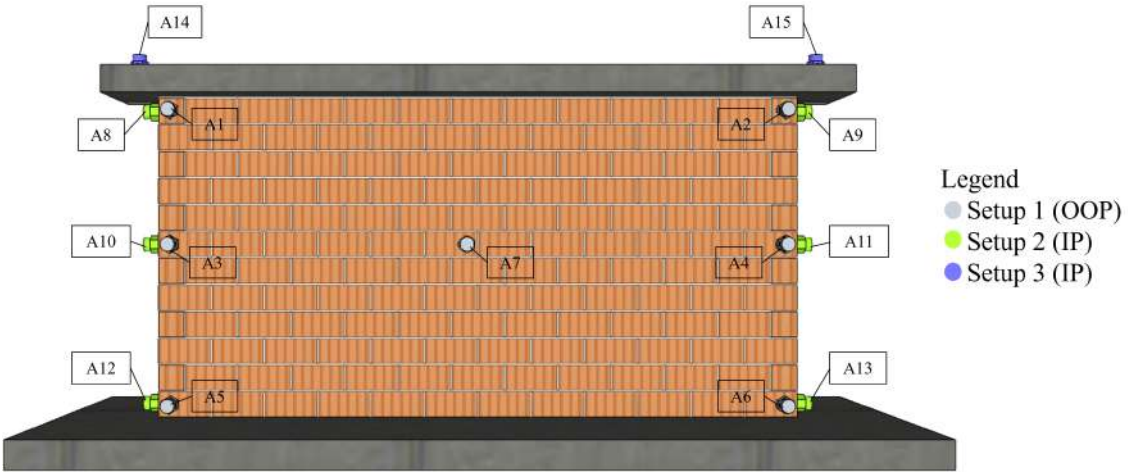

Source: Author (2025)

The accelerometers were affixed using metallic mounting studs that were directly bonded to the wall surfaces. For each test configuration, time segments were recorded with a total duration of at least 2000 times the fundamental period of the structure, resulting in a total measuring time of approximately 2 minutes.

To complement the ambient vibration levels and ensure sufficient excitation across a broad frequency range, spatially and temporally spaced random impacts were applied using a 250 g rubber hammer. This procedure aimed to enhance the structural response while maintaining the principles of Operational Modal Analysis.

5 RESULTS AND DISCUSSION

This chapter presents and discusses the experimental results obtained from all the physical models tested in the laboratory, including data from the damage analysis. As described in Chapter 4, the tests followed a predefined sequence: modal parameters were first extracted from the intact models, followed by a damage phase involving the application of load states, after which the models were retested under ambient vibration. The content includes static test graphs—load history and measured displacements—the results of ambient vibration data processing and dynamic parameter extraction at each stage, the application and discussion of damage metrics, and, finally, the evaluation of the influence of the tested variables.

5.1 Analysis of static testing results

During the application of horizontal loading, the formation of cracks was carefully monitored. For almost all models, the final pre-defined loading cycle did not lead to the ultimate failure of the panels. Therefore, an additional cycle was conducted until failure occurred. Before presenting the measured data, it is important to briefly address an issue observed during the testing of the first specimen, model PCE-A, since the problems encountered with this model led to adjustments that were implemented and maintained throughout the remainder of the tests.

The first problem with this model occurred during the vertical pre-load. At approximately 6 kN, cracking sounds were heard, and visible cracks appeared in parts of the top slab and in the blocks of the first course. It was concluded that the distribution beam was not properly supported, leading to stress concentration. To address this, a mineral fiber layer was placed beneath the steel beam to improve load transfer and ensure uniform distribution. This solution proved effective, allowing the test to continue without further issues.

After resolving this issue, monitoring of the test revealed that the pre-compression forces, and consequently the lateral loads, had been underestimated. This occurred because, in the first load calculations, the vertical load was calculated based on the compressive strength of the masonry walls using the design partial safety factor $\gamma_m = 2$. However, during the test cycles, it became evident that the resulting load levels were too low, producing little or no visible damage to the specimen. To address this, a reduced safety factor of $\gamma_m = 1$ was adopted for the subsequent models, corresponding to the values previously presented in Section 4.3.2. This adjustment resulted in higher applied loads, more consistent with the expected structural behavior under test conditions. As a result, no ultimate lateral load was applied to model PCE-A, and this distinction will be reflected

in the results presented in this section.

Most of the remaining wall models failed in shear, exhibiting diagonal cracking (as shown in Figure 42) and crushing in the compressed corner. These failures occurred abruptly during the final loading cycle, with few visible cracks observed in the preceding cycles. Only models PCO-A and PCO-C showed crack openings in the mortar joints at the tensioned corner. Model PCE-C showed a pre-existing crack in the first course, likely caused during transportation. Figure 43 illustrates the cracking patterns observed in all specimens at the end of the tests.

Figure 42 – Representative examples of diagonal cracking failure in the panels

(a) Model PCO-B (b) Model PCE-B

Source: Author (2025)

During the application of pre-compression, one closely monitored parameter was the evolution of the out-of-plane displacement of the wall panel. It is worth reiterating that pre-compression refers to the vertical load applied at the beginning of the test and maintained throughout the lateral loading cycles. The maximum displacements recorded across all cycles and models were 3.80 mm under a vertical load of 69.16 kN for the concrete block specimens, and 3.64 mm under 59.16 kN for the clay block specimens. Considering that this transverse displacement can be interpreted as the eccentricity of the vertical force relative to the panel base, the resulting moments at the panel base were $26.28\,\text{kN}\cdot\text{cm}$ and $21.53\,\text{kN}\cdot\text{cm}$, respectively. These are equivalent to horizontal forces of approximately 0.5 kN and 0.4 kN applied at the top of the panel. Visual inspection confirmed that this eccentricity did not induce stresses capable of damaging the models in a way that would compromise the test results.

Following the application of the vertical load, horizontal loading was initiated to establish the damage states of the wall panels. The global behavior during this phase was monitored by tracking the in-plane displacement measured by LVDT 3. Figure 44 shows the load–displacement curves corresponding to the horizontal loading phase for the concrete block models (PCO). In the third predefined cycle, horizontal loads of 12 kN, 20 kN, and 25 kN were applied to models PCO-A, PCO-B, and PCO-C, respectively;

Figure 43 – Cracking patterns of all masonry walls

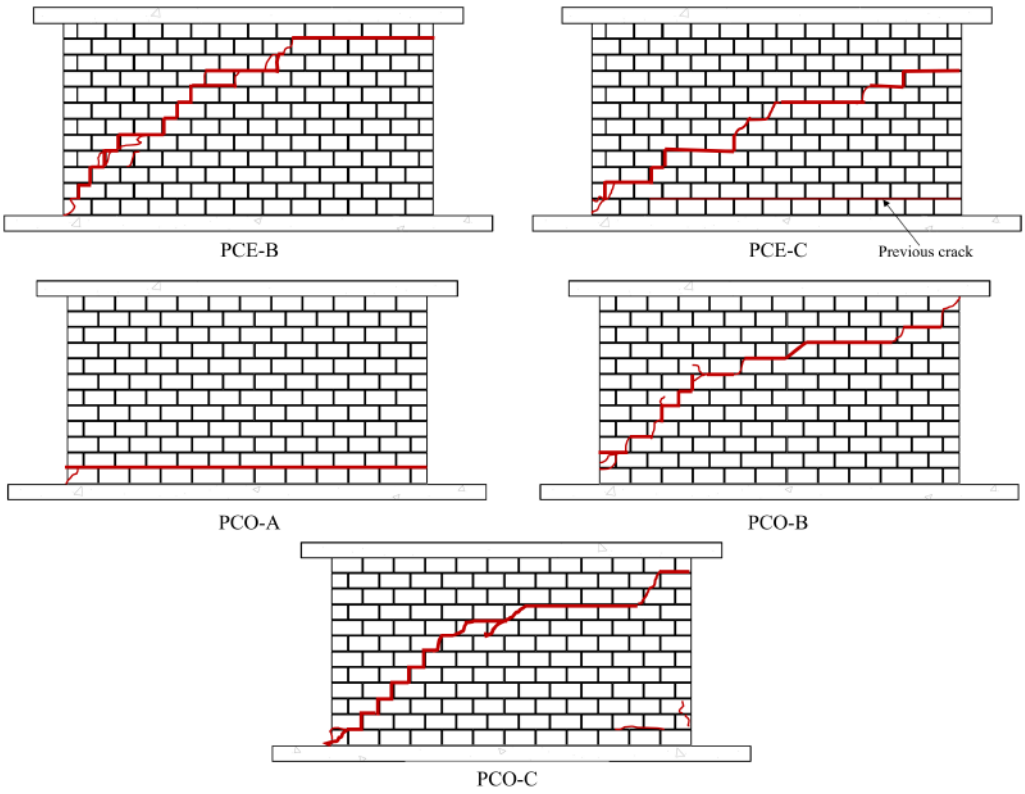

Source: Author (2025)

however, these values did not lead to failure. Therefore, an additional cycle was performed in which the load was increased until failure occurred.

Figure 44 – Horizontal load x In-plane displacements – PCO models

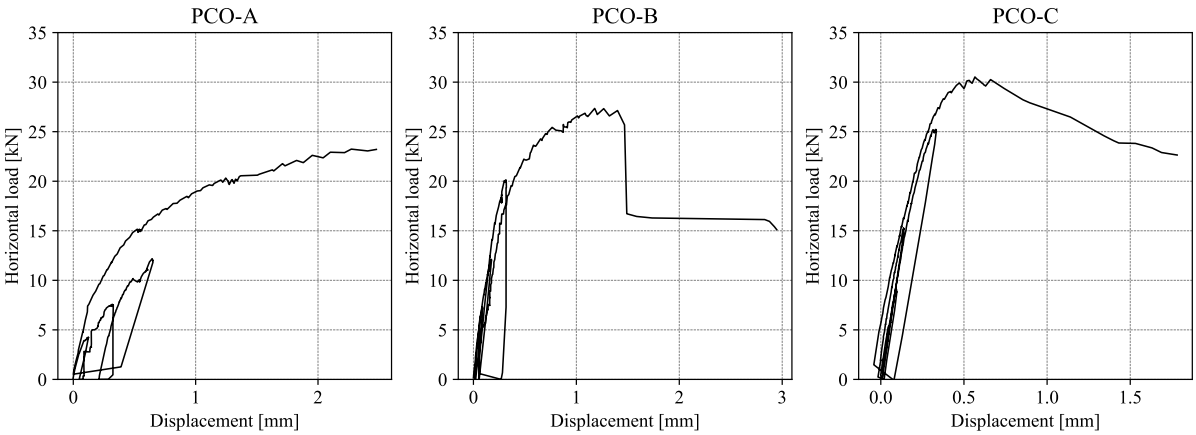

Source: Author (2025)

Figure 45 also presents the corresponding data for the clay block models. In the third cycle, loads of 6 kN, 20 kN, and 22 kN were applied to models PCE-A, PCE-B, and PCE-C, respectively. A fourth cycle was conducted only for models PCE-B and PCE-C, as previously discussed, and resulted in failure of both specimens.

Figure 45 – Horizontal load x In-plane displacements – PCE models

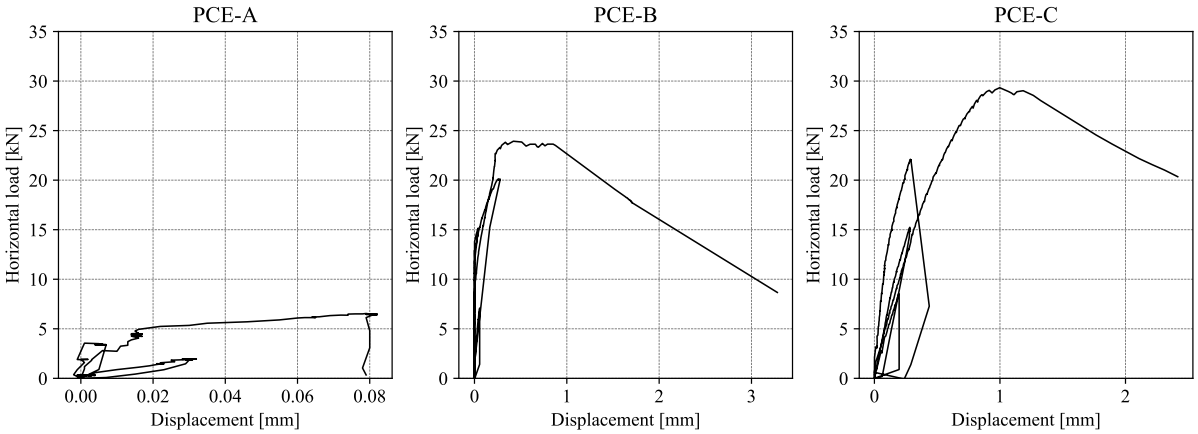

Source: Author (2025)

The peak horizontal loads applied during the tests varied across the different block models. For the concrete block models (PCO), the peak loads were 23.4 kN, 27.4 kN, and 30.5 kN for models A, B, and C, respectively. For the clay block models (PCE), the corresponding values were 6.5 kN, 23.9 kN, and 29.3 kN. These results highlight the increase in shear strength with increasing axial compression.

The graphs presented in Figures 44 and 45 exhibit initial linear segments, which align with the absence of visible cracking during the early loading cycles. As noted earlier, most panels exhibited sudden crack formation; however, the presence of nonlinear behavior preceding the ultimate load suggests the development of internal micro-cracking. This interpretation is supported by the observations of Nascimento Neto (2003), who associate such nonlinear responses with the progressive deterioration of the material at the micro-structural level.

Another way to evaluate the global behavior of the panel during this phase of the test is through the measurement of axial displacements, specifically the shortening of the compressed side (captured by LVDT 4) and the elongation of the tensioned side (captured by LVDT 5). These measurements are valuable for assessing the overall structural behavior of the panels and can be correlated with the development of cracking. Figure 46 presents these measurements for all test cycles in the concrete block wall models, while Figure 47 shows the corresponding data for the clay block models.

In these graphs, the initial values appear negative due to the shortening that occurs during the pre-compression phase. The onset of localized crushing at the panel base can be identified by a sudden drop in force accompanied by a sharp increase in the absolute displacement recorded by LVDT 5. This behavior, derived from the vertical displacements measured by the transducers, is particularly evident in models PCO-B and PCE-B.

The following graphs correspond to key aspects monitored throughout all tests. The

Figure 46 – Horizontal load x Axial displacements – PCO models

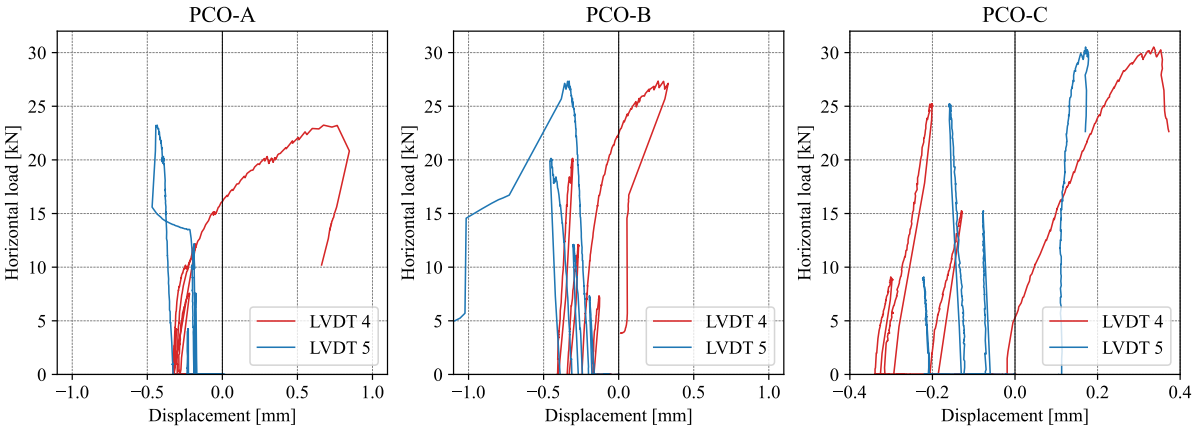

Source: Author (2025)

Figure 47 – Horizontal load x Axial displacements – PCE models

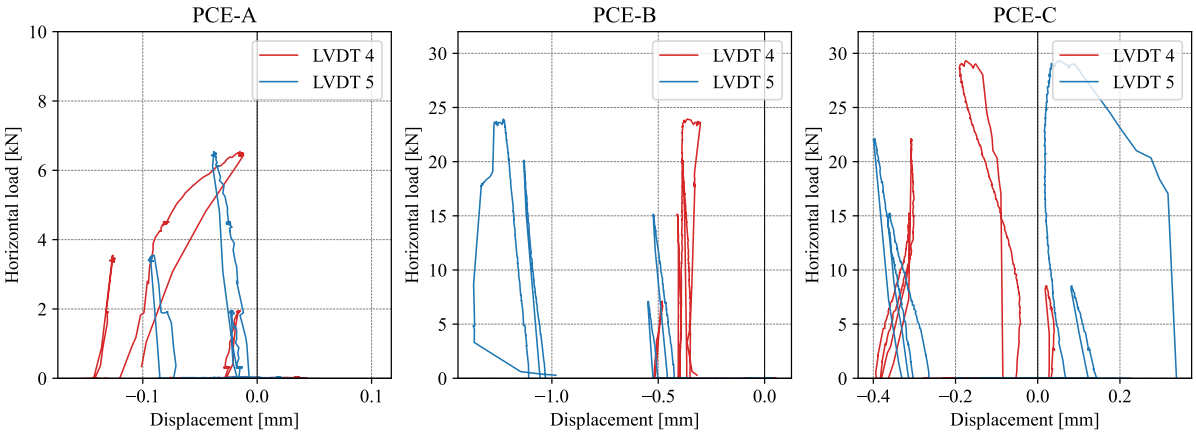

Source: Author (2025)

first verification involved assessing potential slip between the top slab and the masonry panel, as well as between the base slab and the laboratory floor, in order to ensure control over the boundary conditions. Figures 48 and 49 show that the top slab exhibited negligible displacement across all models, while the maximum slip observed at the base slab was approximately 0.7 mm, also too small.

The final verification concerns the consistency of the pre-compression force during the application of the horizontal load, which is necessary due to the slight inclination of the vertical hydraulic actuator and the characteristics of the hydraulic system used for applying this load. In this context, Figures 50a and 50b correlate the variation of the vertical and horizontal forces.

The graphs reveal an initial vertical segment corresponding to the application of pre-compression. For each model, variations in this segment can be observed with the application of lateral loading. It is important to note that adjustments using the hydraulic pump were performed only during the pre-compression phase to maintain the target load.

Figure 48 – Horizontal load x Slip of the slabs – PCO models

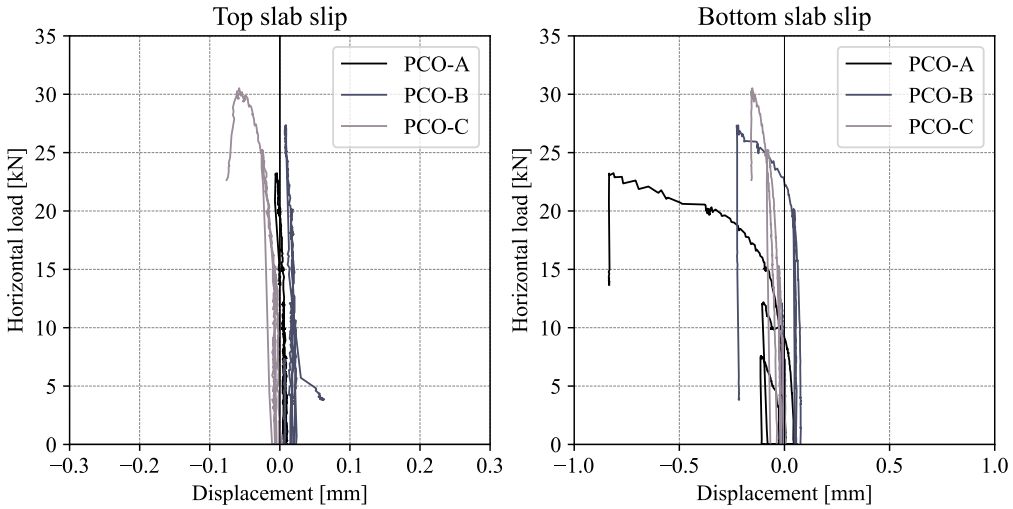

Source: Author (2025)

Figure 49 – Horizontal load x Slip of the slabs – PCE models

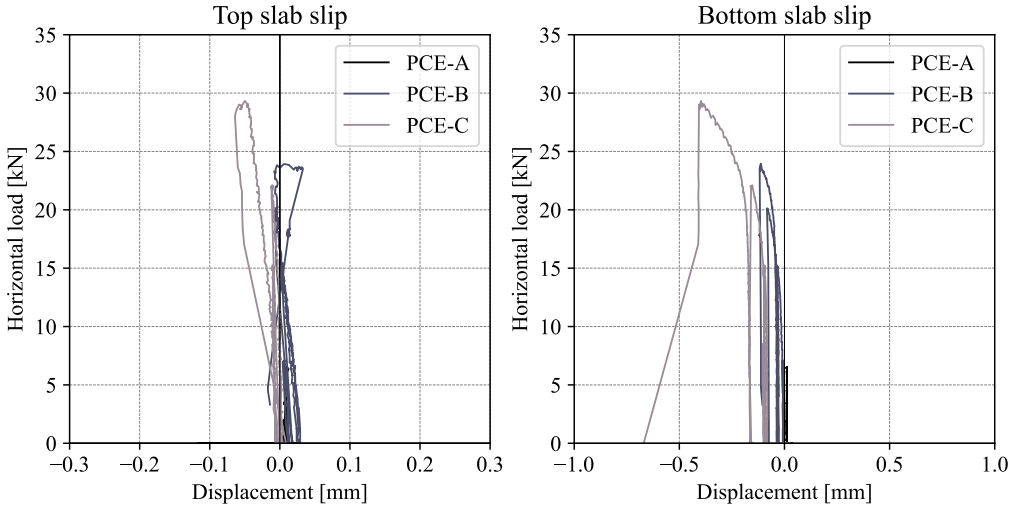

Source: Author (2025)

The inclinations of the hydraulic jacks were also measured using inclinometers, which indicated maximum deviations of up to 1 degree. According to the graphs, the models that exhibited the greatest variation were PCO-A and PCE-C during their final cycle of lateral loading. These variations, however, are expected to some extent and did not appear to compromise the integrity of the tests.

5.2 Extraction of modal parameters

The data collected during the dynamic tests were originally recorded as acceleration in units of g (which denotes the acceleration due to gravity, approximately 9.8 m/s^2). For consistency and analytical purposes, the acceleration data were converted to the International System unit of meters per second squared (m/s^2). Each test lasted 120

Figure 50 – Vertical load x Horizontal load

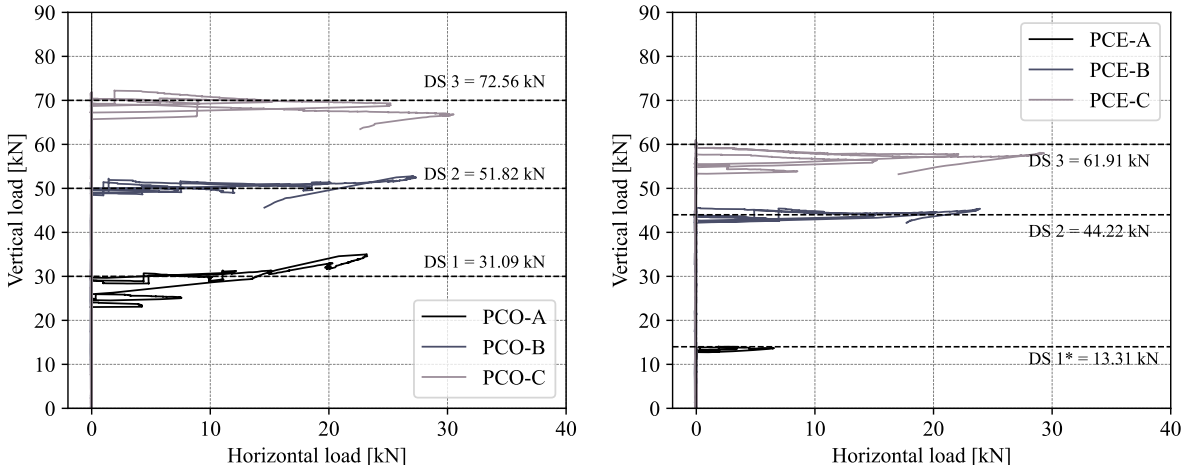

(a) PCO models (b) PCE models

Source: Author (2025)

seconds, during which random impacts were applied in the direction of vibration. Figure 51 presents a representative time-history plot of a single out-of-plane impact, while Figure 52 shows a typical acceleration time-history in which the sequence of impacts throughout the entire test can be observed.

Figure 51 – Time-history plot of a typical impact event

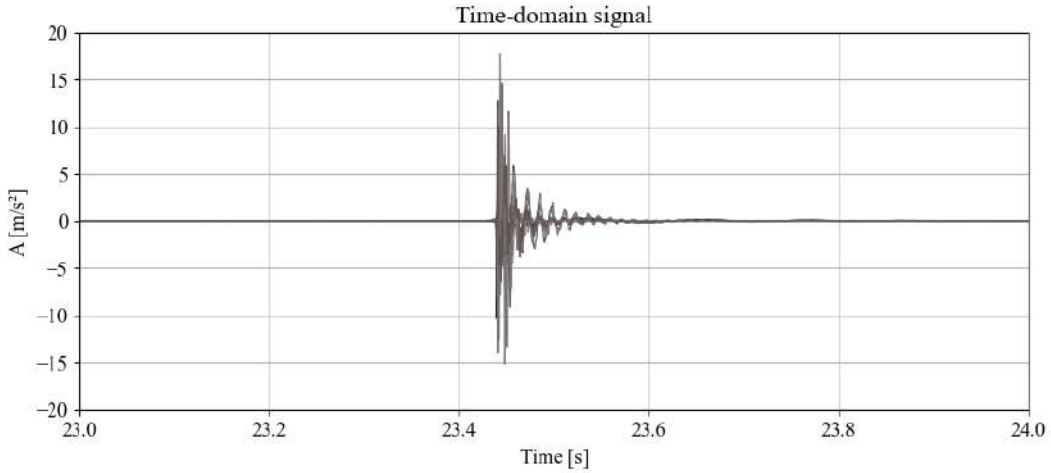

Source: Author (2025)

The raw data were processed using the Basic Frequency Domain method, implemented in Python using functions from the SciPy.signal library (Virtanen *et al.*, 2020). The Power Spectral Density of the structural response was estimated by using Welch's method. For this, the signals were divided into segments of 3000 points for the out-of-plane measurements and 4096 points for the in-plane data, both with 50% overlap. A Hanning window was applied to each segment to minimize spectral leakage. The PSD functions were

Figure 52 – Example of acceleration versus time plot

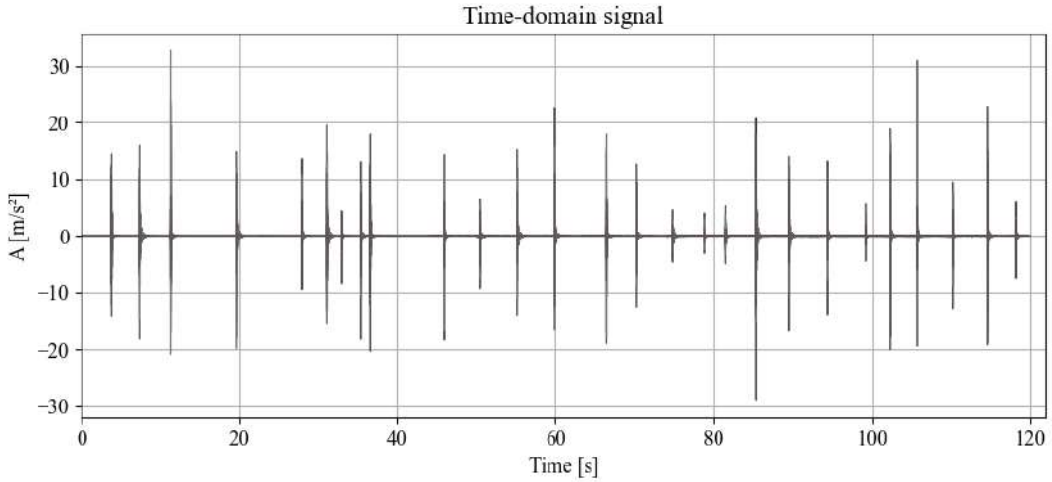

Source: Author (2025)

computed at the corresponding sampling frequencies, resulting in frequency resolutions of 1.00 Hz and 0.73 Hz, respectively.

The natural frequencies were identified from peaks in the Averaged Normalized Power Spectral Density (ANPSD), exemplified by in Figure 53. These peaks served as the primary indicators of the structure's natural frequencies. Additionally, coherence functions and cross-spectral analysis (Figure 54) were used to confirm the consistency and reliability of the frequencies identified in the ANPSD.

Independent tests were conducted for the in-plane and out-of-plane measurements, without a reference accelerometer between them. Accordingly, and to better understand the dynamic behavior and the sequence of the emerging vibration modes, unified PSD curves were plotted for the three tests performed. Figures 55 and 56 illustrate the outcome of this procedure for one specimen of each material.

The analysis of the PSD plots enabled the identification of peak responses and the estimation of natural frequencies. Tables 30 and 31 present the first six natural frequencies identified for the undamaged wall models, with in-plane modes indicated by (IP). It is important to note that the order in which the frequencies are listed does not necessarily indicate correspondence in mode shapes between models.

Table 30 – Natural frequencies of undamaged PCO wall models

Model	f_1 **(Hz)**	f_2 **(Hz)**	f_3 **(Hz)**	f_4 **(Hz)**	f_5 **(Hz)**	f_6 **(Hz)**
PCO-A	48.0	125.9	209.8	217.8 (IP)	225.8 (IP)	391.7
PCO-B	48.0	149.9 (IP)	180.9	237.8	394.7	414.7 (IP)
PCO-C	40.0	88.9 (IP)	160.9	173.9 (IP)	358.7	503.6 (IP)

Source: Author (2025)

Evidently, variations in geometry, mass, and excitation conditions may cause certain

Figure 53 – Average normalized spectrum of out-of-plane acceleration records and identified natural frequencies for PCO-C - Undamaged (Stage 0)

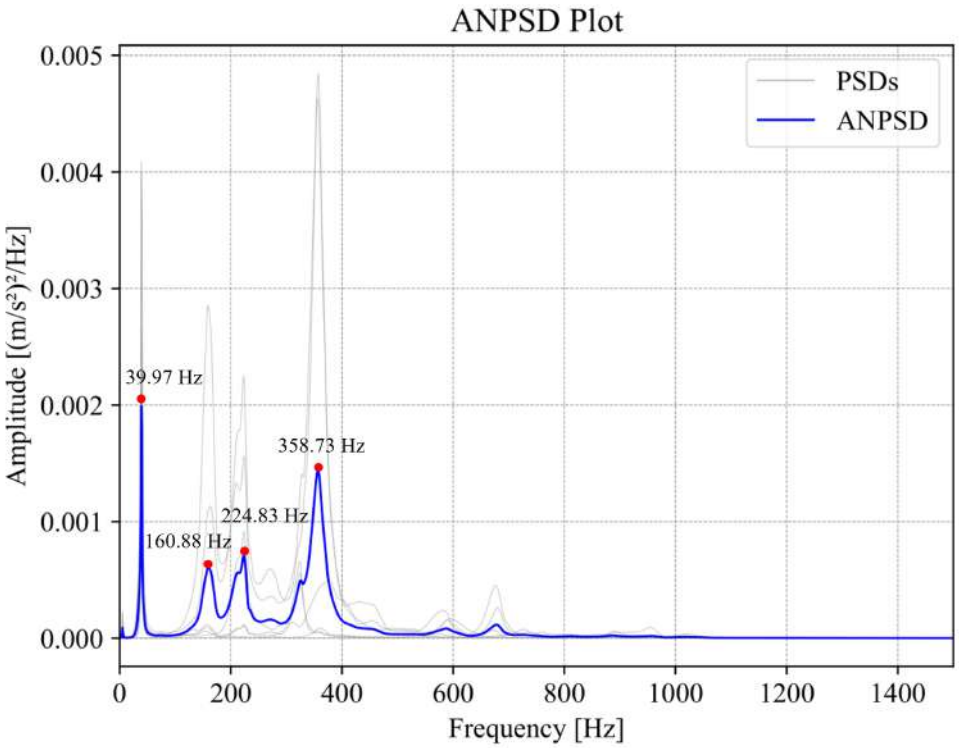

Source: Author (2025)

Figure 54 – Cross power spectral density of out-of-plane acceleration for PCO-C – Undamaged (Stage 0)

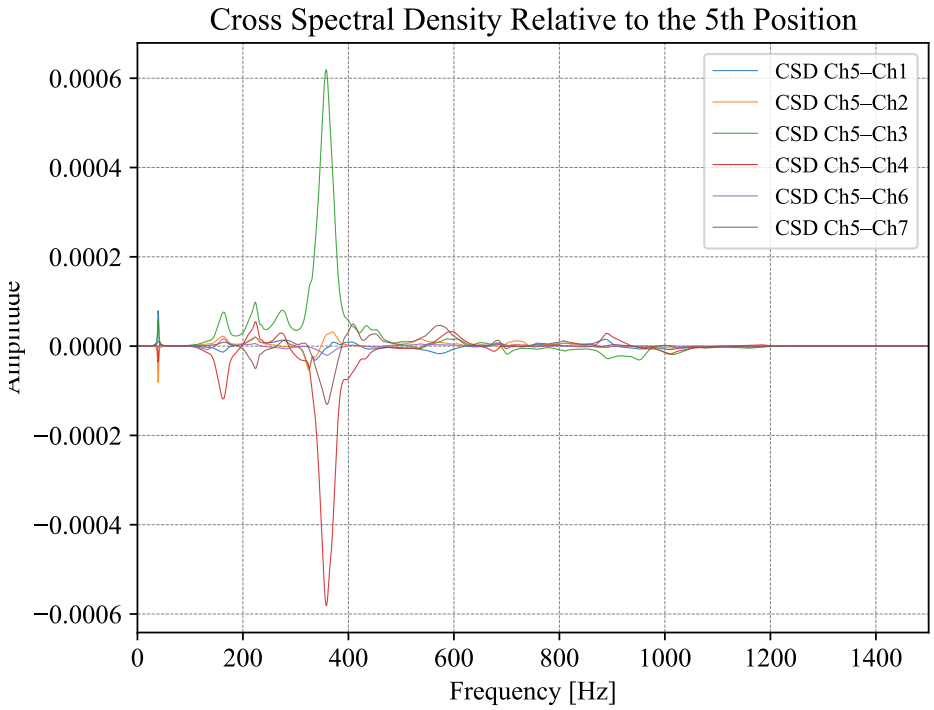

Source: Author (2025)

Figure 55 – PSD curves for out-of-plane and in-plane measurements: PCO-C – Undamaged (Stage 0)

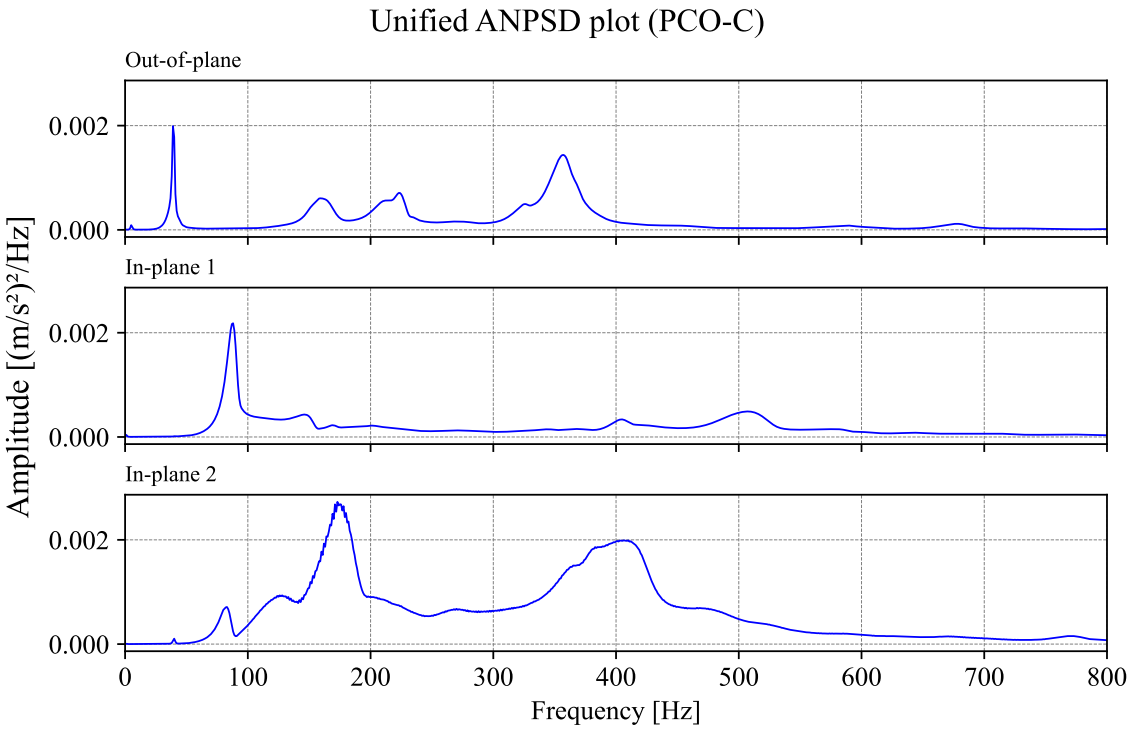

Source: Author (2025)

Figure 56 – PSD curves for out-of-plane and in-plane measurements: PCE-C – Undamaged (Stage 0)

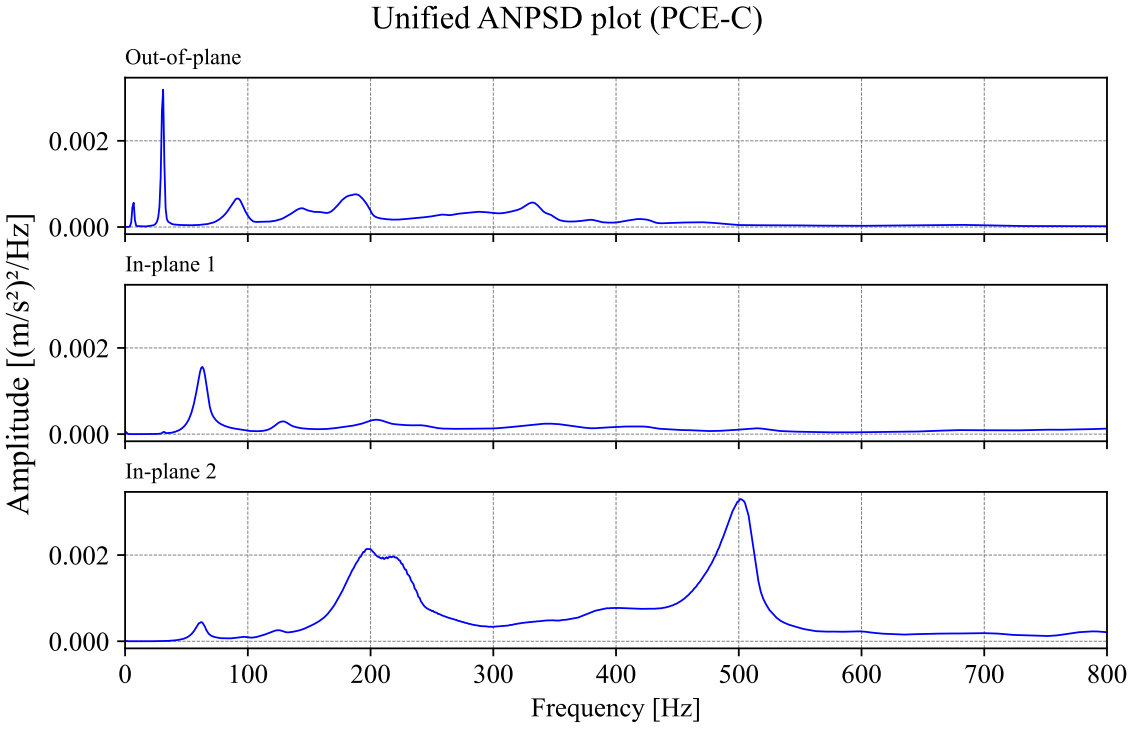

Source: Author (2025)

Table 31 – Natural frequencies of undamaged PCE wall models

Model	f_1 **(Hz)**	f_2 **(Hz)**	f_3 **(Hz)**	f_4 **(Hz)**	f_5 **(Hz)**	f_6 **(Hz)**
PCE-A	38.0	61.0 (IP)	87.0	125.0	175.8	218.8 (IP)
PCE-B	38.0	74.0 (IP)	124.0	231.8	352.7 (IP)	369.7
PCE-C	32.0	63.0 (IP)	92.0	142.9	218.8 (IP)	332.8

Source: Author (2025)

vibration modes to be absent or to appear in a different order across models, particularly those associated with lower modal participation factors. A Modal Assurance Criterion analysis is a way to evaluate the similarity between modes across the different models.

Mode shapes were estimated by evaluating the transfer functions between a reference response signal r and the remaining responses signals j at each resonance frequency ω_i. This is done using Equation 5.1, as presented by Rodrigues (2004), where $\tilde{G_{yi}}[r, j]$ represents the cross power spectral density between signals r and j and $\tilde{G_{yi}}[r, r]$ denotes the auto power spectral density at the reference point:

$$\Phi_{ji} \approx \frac{\tilde{G_{yi}}[r, j]}{\tilde{G_{yi}}[r, r]} \tag{5.1}$$

The mode shapes associated with the identified natural frequencies were plotted for all models at each damage stage. As an example, Figure 57 illustrates the first six mode shapes identified for the undamaged condition of model PCO-C. In the figure, the lighter-colored elements represent the undeformed configuration of the model, while the gradient-shaded elements depict the corresponding modal deformations. The first, third, and fifth modes are out-of-plane: the first and fifth exhibit out-of-plane bending, while the third is a combination of torsion and bending. The remaining modes are in-plane: the second and sixth correspond to bending in the XZ plane, and the fourth to bending in the Z direction.

To illustrate the mode shapes for the clay block models, Figure 58 presents those identified for the undamaged state of model PCE-C. In this representation, it is possible to see that the second and fifth modes are in-plane, with the second corresponding to bending in the XZ plane and the fifth to bending along the Z direction. The remaining modes are out-of-plane: the first, fourth, and sixth are out-of-plane bending modes, while the third mode is torsional.

In all cases, an AutoMAC analysis was performed, which evaluates the consistency of each mode shape with itself, allowing the identification of similar or repeated modes within the same analysis. For the out-of-plane mode shapes presented in Figures 57 and 58, the corresponding AutoMAC matrices are shown in Figure 59.

Low values observed outside the main diagonal suggest that the modal coordinates are not similar, indicating that the identified modes are distinct from one another. This

Figure 57 – Mode shape configurations for PCO-C – Undamaged (Stage 0)

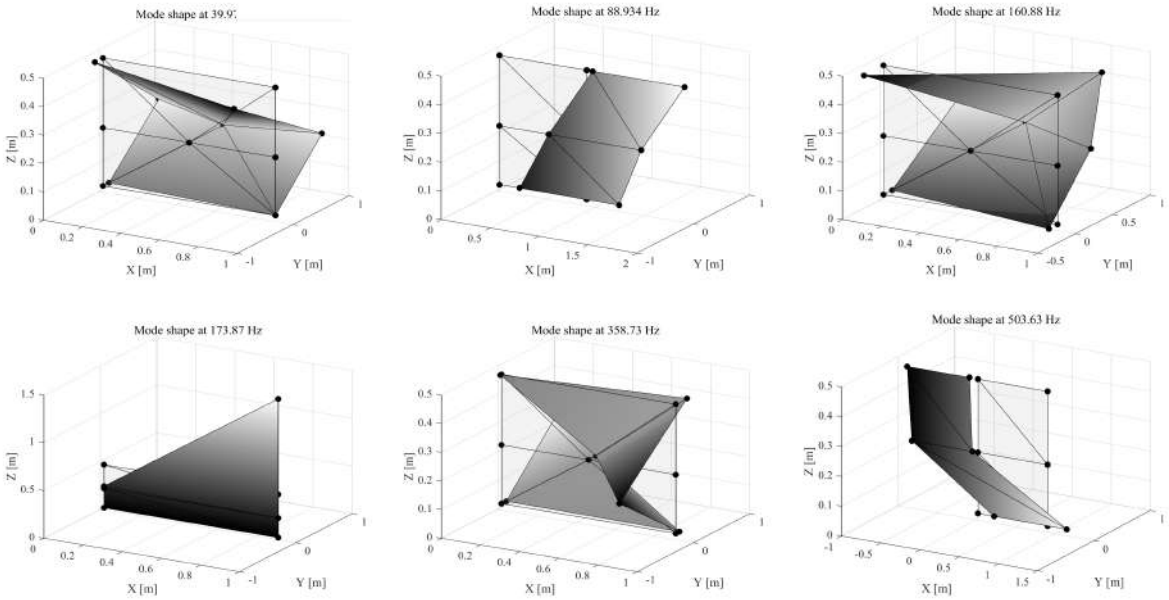

Source: Author (2025)

Figure 58 – Mode shape configurations for PCE-C – Undamaged (Stage 0)

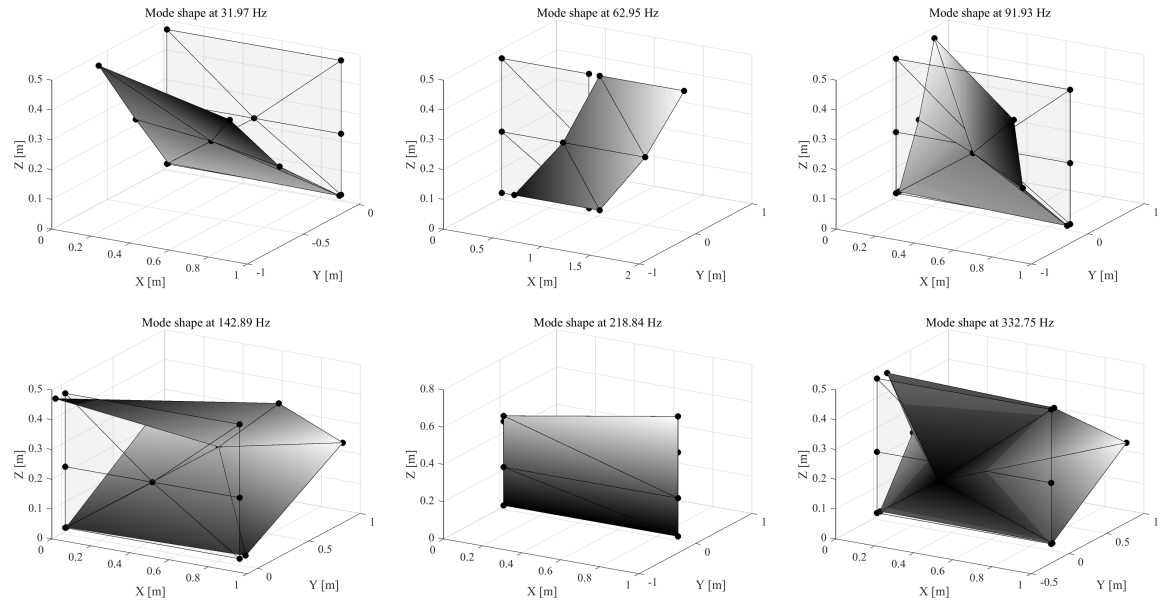

Source: Author (2025)

Figure 59 – AutoMAC analysis for mode shape verification

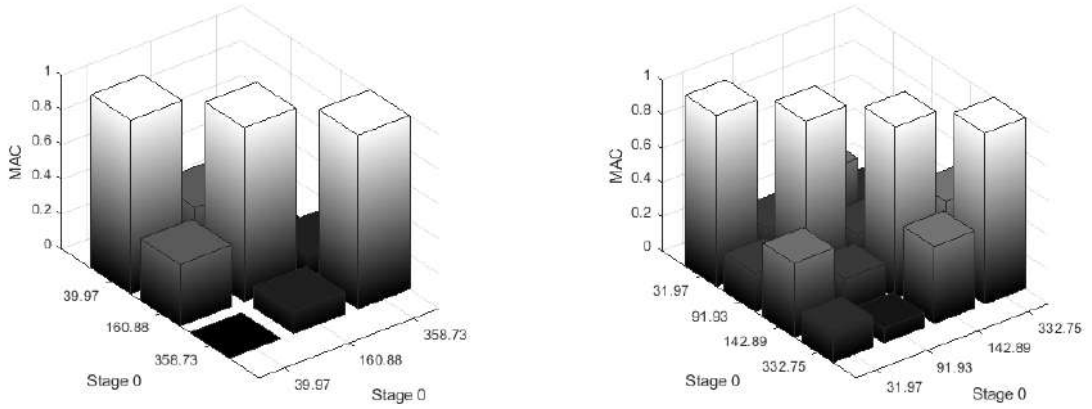

(a) PCO-C - Undamaged (b) PCE-C - Undamaged

Source: Author (2025)

interpretation is further supported by the spacing between the corresponding natural frequencies.

5.2.1 Modal identification of top slabs

An additional verification was conducted on the top slabs to determine the dynamic modulus of the reinforced mortar prior to their placement on the walls. The procedure followed the ASTM E1876-22 standard (Americal Society for Testing and Materials, 2022). Three accelerometers were mounted on three slab specimens, each supported at its fundamental nodal points (located at 0.224L from each end), as illustrated in Figure 60.

A procedure similar to that used for the walls was applied to these specimens, but with the specific aim of exciting only the fundamental flexural frequency. This was achieved through impacts applied near the center of each specimen using a non-instrumented hammer. The acceleration data were processed, and the target frequency was identified from the PSD plot (see Figure 61).

The specimens were also weighed and measured, allowing for the determination of all variables required to calculate the dynamic modulus of elasticity, E_{cd}, as expressed in Eq. 5.2.

$$E_{cd} = 0.9465 \left(\frac{m f_f^2}{b} \right) \left(\frac{L^3}{t^3} \right) T_1 \tag{5.2}$$

In this equation, E_{cd} is the dynamic Young's modulus (Pa); m is the mass of the bar (g); b, L and t are the width, length and thickness of the bar (mm), respectively; f_f is the fundamental resonant frequency of bar in flexure (Hz) and T_1 is the correction factor for fundamental flexural mode to account for finite thickness of bar, Poisson's ratio, and so forth.

Figure 60 – Sensor placement for impulse excitation testing on the top slabs

Source: Author (2025)

Figure 61 – Representative PSD plot used to identify the fundamental flexural frequency of the top slabs

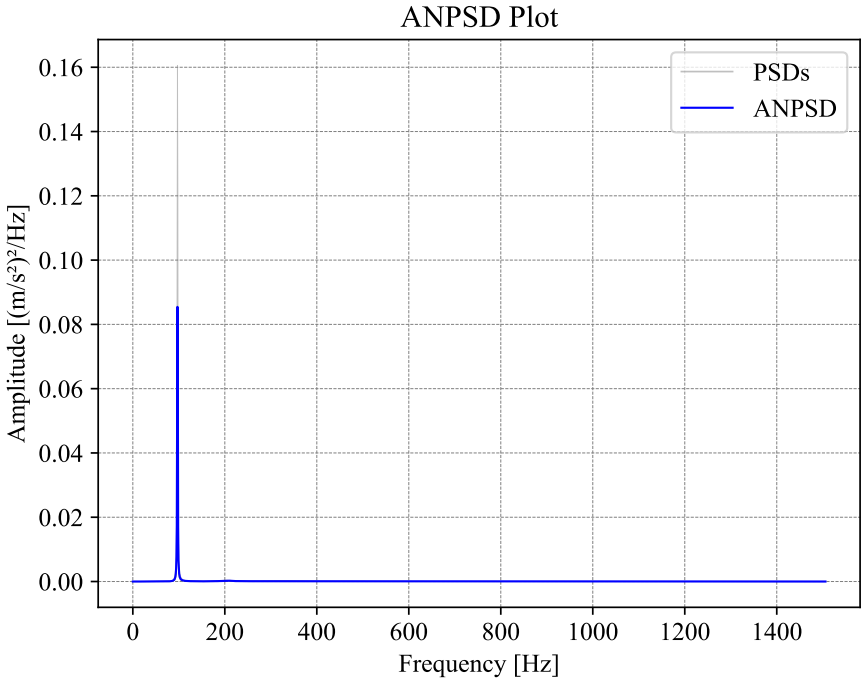

Source: Author (2025)

According to the standard, when $L/t \geq 20, T_1$ can be simplified to $1 + 6.585(t/T)^2$. Table 32 presents the collected parameters and the corresponding calculated dynamic modulus for each specimen.

Table 32 – Collected parameters and Dynamic Young's modulus for each top slab

Specimen	m (g)	b (mm)	L (mm)	t (mm)	f_f (Hz)	L/t	T_1	E_{cd} (GPa)
Slab 1	10800	150	1100	40	93.9	27.5	1.0087	12.613
Slab 2	11150	150	1100	40	99.9	27.5	1.0087	14.739
Slab 3	11800	150	1100	40	97.9	27.5	1.0087	14.980

Source: Author (2025)

The resulting average value was 14.11 GPa which is close to that obtained for the specimens presented in Section 4.2.2. The mean deviation of this sample was 1.30, and the coefficient of variation was 9.23%.

5.3 Experimental damage identification

Damage assessment in the masonry walls was based on the analysis of three key parameters: changes in natural frequencies, evaluation of the Modal Assurance Criterion, and analysis of the Coordinate Modal Assurance Criterion. The latter were developed in Python following the equations 2.29 and 2.30.

Damage detection based on shifts in natural frequencies is a widely used approach; however, it presents limitations, as it typically requires either highly precise measurements or significant levels of damage to be effective (Doebling *et al.*, 1996). Nevertheless, by compiling the ANPSD data from the tests executed in this study, a decreasing trend can be observed in the frequency of certain peaks, and consequently, in the corresponding natural frequencies. Figure 62 illustrates this behavior for specimen PCO-A, considering only out-of-plane modes.

In this model, cracking was observed in the lower courses only at damage stage 2. Nonetheless, a slight shift in peak frequencies can already be seen from the undamaged condition to stage 1, even though no visible cracks were present at this point. In stage 3, no new cracks formed, yet the trend of resonance peaks shifting leftward (i.e., to lower frequencies) becomes more evident.

Figure 63 presents the corresponding data for a clay block specimen. In this case, only very small cracks were observed at stage 3. Nevertheless, as with the concrete block model, a noticeable leftward shift in the spectral peaks can be seen, indicating a reduction in the associated natural frequencies. This trend reinforces the sensitivity of this type of analysis, even in the presence of minor or barely visible damage.

By comparing the fundamental frequency—i.e., the lowest frequency—listed in

Figure 62 – ANPSD curves for undamaged and damaged states – PCO-A model

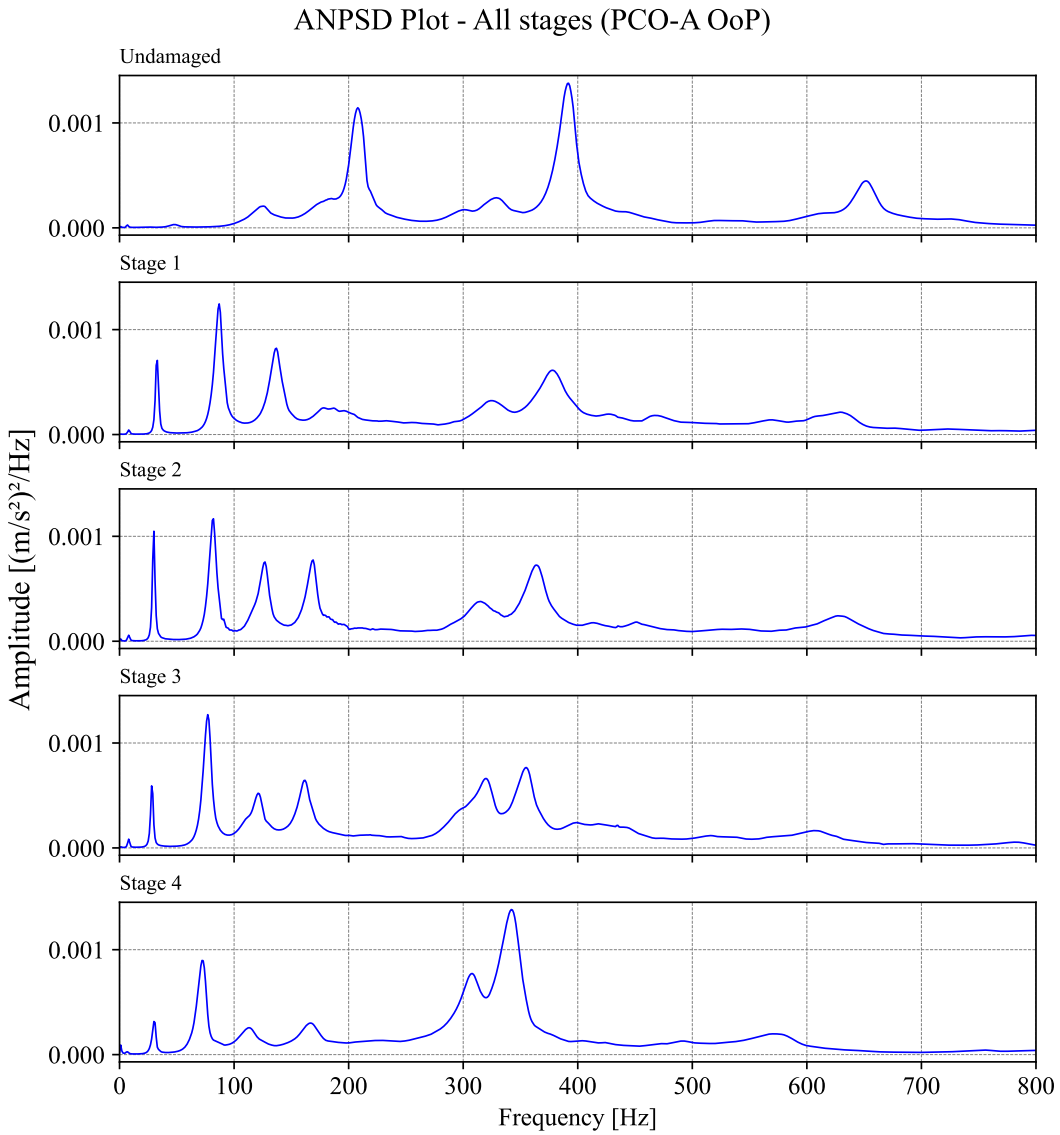

Source: Author (2025)

Tables 33 and 34, it is possible to evaluate the reduction through the parameter Δ, which denotes the frequency variation relative to the undamaged state.

A comparison of the values in these tables reveals a clear reduction in all natural frequencies. It is also noteworthy that, as the level of pre-compression increases, the magnitude of this reduction tends to decrease. A possible explanation lies in the broadly accepted understanding that axial compression in unreinforced masonry enhances its shear strength, thereby limiting the extent of damage under lateral loading.

A more detailed analysis of multiple vibration modes within a single model, considering the progression of damage, requires additional procedures. The first step involves aligning corresponding modes across different damage stages by comparing their mode shapes and calculating the MAC. In this study, a MAC value above 0.8 was considered indicative of a strong correlation between mode shapes. Tables 35 and 36 show the first four

Figure 63 – ANPSD curves for undamaged and damaged states – PCE-B model

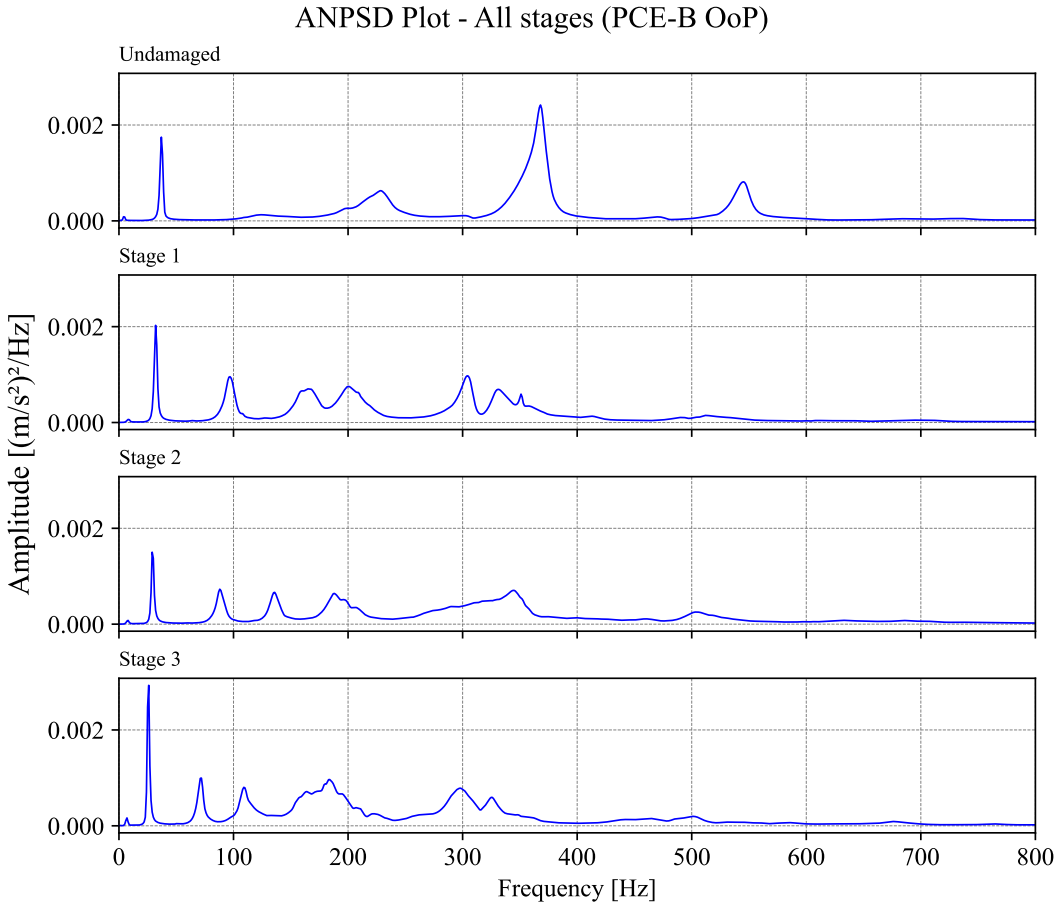

Source: Author (2025)

Table 33 – First natural frequency and its relative variation for the PCO models

Stage	**PCO-A**		**PCO-B**		**PCO-C**	
	ω (Hz)	Δ (%)	ω (Hz)	Δ (%)	ω (Hz)	Δ (%)
0	48.0	–	48.0	–	40.0	–
1	34.0	-29.17	35.0	-27.08	38.0	-5.00
2	31.0	-35.41	34.0	-29.18	36.0	-10.01
3	29.0	-39.58	32.0	-33.33	36.0	-10.01
4	31.0	-35.41	20.0	-58.33	–	–

Source: Author (2025)

Table 34 – First natural frequency and its relative variation for the PCE models

Stage	**PCE-A**		**PCE-B**		**PCE-C**	
	ω (Hz)	Δ (%)	ω (Hz)	Δ (%)	ω (Hz)	Δ (%)
0	38.0	–	38.0	–	32.0	–
1	27.0	-28.95	33.0	-13.17	30.0	-6.23
2	26.0	-31.58	30.0	-21.05	29.0	-9.36
3	25.0	-34.21	27.0	-28.94	28.0	-12.48

Source: Author (2025)

out-of-plane natural frequencies that exhibited correlation for the undamaged condition and for each damage stage of the PCO-C and PCE-C models, respectively.

Table 35 – Natural frequencies and relative variation for different vibration modes – PCO–C

Stage	1st Bending XY		1st Torsion		2nd Bending XY		3rd Bending XY	
	ω (Hz)	Δ (%)	ω (Hz)	Δ (%)	ω (Hz)	Δ (%)	ω (Hz)	Δ (%)
0	40.0	–	160.9	–	358.7	–	574.6	–
1	38.0	-5.00	137.9	-14.29	285.8	-20.33	331.8	-42.26
2	36.0	-10.01	130.9	-18.64	215.8	-39.83	300.8	-47.65
3	36.0	-10.01	129.9	-19.25	210.8	-41.22	299.8	-47.83

Source: Author (2025)

Table 36 – Natural frequencies and relative variation for different vibration modes - PCE–C

Stage	1st Bending XY		1st Torsion		2nd Bending XY		3rd Bending XY	
	ω (Hz)	Δ (%)	ω (Hz)	Δ (%)	ω (Hz)	Δ (%)	ω (Hz)	Δ (%)
0	32.0	–	91.9	–	142.9	–	332.8	–
1	30.0	-6.23	83.9	-8.69	114.9	-19.58	326.8	-1.80
2	29.0	-9.36	85.9	-6.52	114.9	-19.57	317.8	-4.51
3	28.0	-12.48	77.9	-15.22	109.9	-23.08	354.8	6.61

Source: Author (2025)

For both models, the final loading cycle caused significant damage to the structure, resulting in the loss of some measurement points. Therefore, the analysis is limited to the first three loading/damage cycles. Furthermore, no visible cracking or apparent damage was observed throughout the entire test. To visually present the evaluated modes and their variations, Figures 64 and 65 displays these modes along with their corresponding changes.

In this study, the MAC was calculated by comparing the mode shape vectors of the undamaged condition (Stage 0) with those of each damaged state. Although this coefficient is a Level 1 damage indicator—meaning it cannot localize damage but only confirm its presence—it remains a fundamental tool for damage identification. Figures 66 and 67 show the corresponding MAC matrices for the evaluated cases, presented in a three-dimensional graphical format.

Although the MAC is not considered a highly sensitive or precise indicator for damage detection, a noticeable reduction in correlation for modes 3 and 4 can be observed from Stage 2 onward in the PCE-C model, indicating that these modes were more affected by the damage. In the case of the PCO-C model, a significant and visible change in the deformed mode shapes occurs between Stage 0 and Stage 1, and this alteration persists throughout the subsequent stages. For this model, it is also useful to evaluate the variation in MAC values by comparing each stage with the next, as it may provide additional insight

Figure 64 – Mode shape configurations during progressive damage – PCO-C model

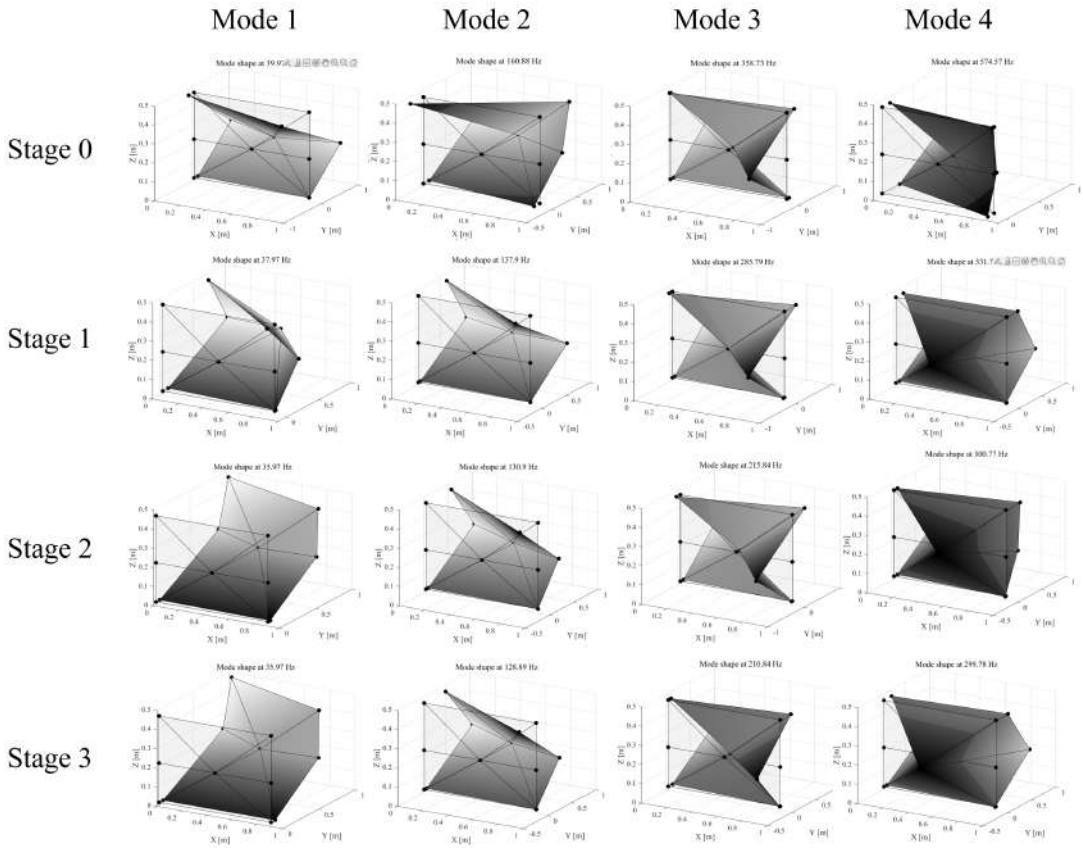

Source: Author (2025)

into the evolution of damage. Figure 68 shows the MAC matrices for the PCO-C model, highlighting this comparative analysis between consecutive stages.

The effect on the first natural frequency between damage Stages 1 and 2, as well as on the third frequency from Stage 2 to the final damage stage, can now be clearly observed by examining the corresponding values in the bars. This behavior reinforces the trends previously identified in Table 35.

The final damage parameter analyzed is the COMAC, which assesses the correlation for each modal coordinate associated with the structure's degrees of freedom. In this study, COMAC was employed to compare the undamaged condition with each of the damaged states. Figures 69 and 70 present the results for the measurement points related to out-of-plane mode shapes, where each bar color represents the comparison between a specific damage stage and the undamaged condition.

Although few cracks were visually detected during the test, the COMAC results for the PCE-C model reveal a reduction in correlation at point 5—located at the compressed corner—and at point 7, situated at mid-span, where a diagonal crack developed near the end of the test. Interestingly, an increase in the COMAC value was observed at point 6, which may lead to a misleading interpretation of the structural condition at that location.

Figure 65 – Mode shape configurations during progressive damage – PCE-C model

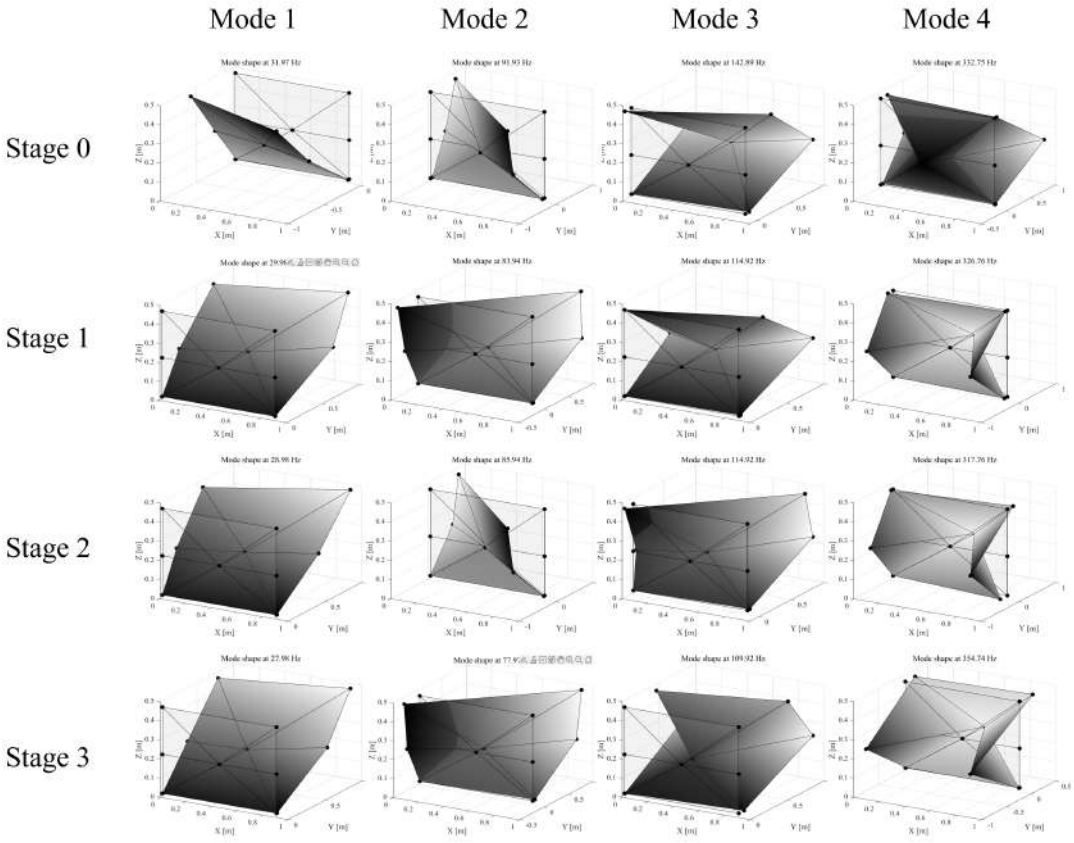

Source: Author (2025)

Figure 66 – MAC results for all damage stages of the PCO-C model

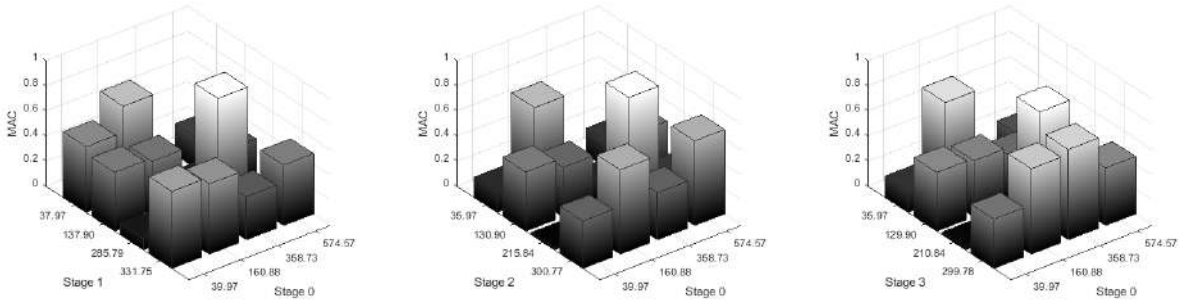

(a) Stage 0 - Stage 1 (b) Stage 0 - Stage 2 (c) Stage 0 - Stage 3

Source: Author (2025)

Figure 67 – MAC results for all damage stages of the PCE-C model

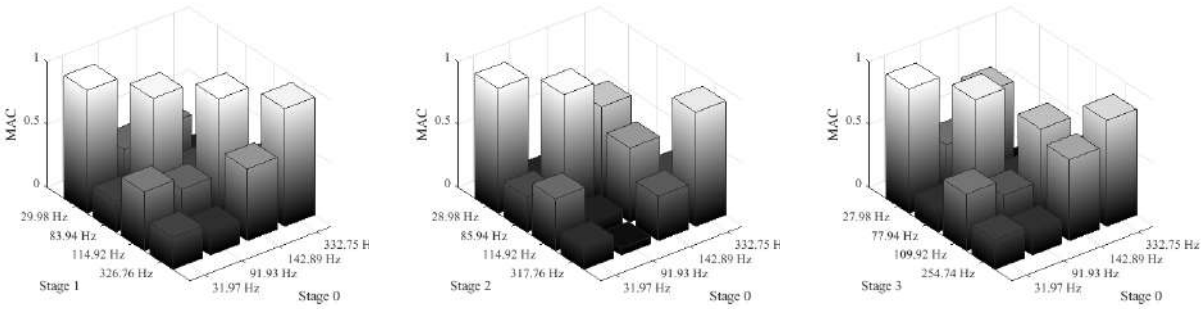

(a) Stage 0 - Stage 1 (b) Stage 0 - Stage 2 (c) Stage 0 - Stage 3

Source: Author (2025)

Figure 68 – MAC results between consecutive stages for the PCO-C model

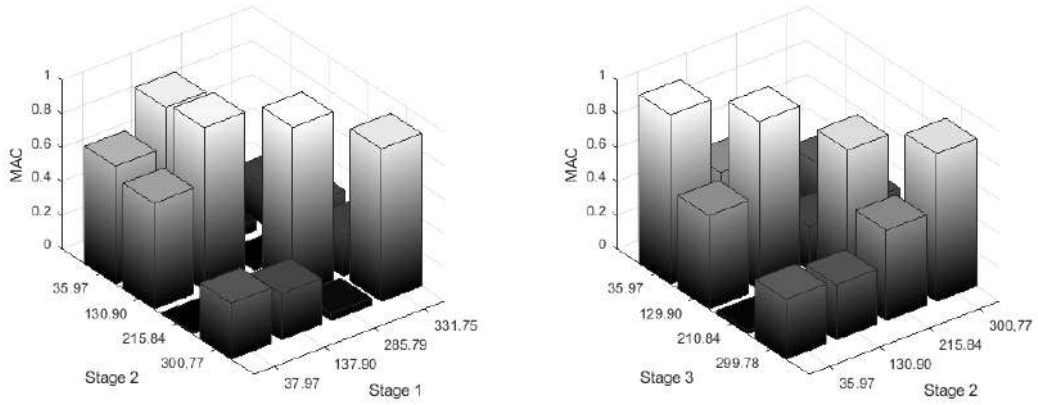

(a) Stage 1 - Stage 2 (b) Stage 2 - Stage 3

Source: Author (2025)

Figure 69 – COMAC coefficients – PCO-C model

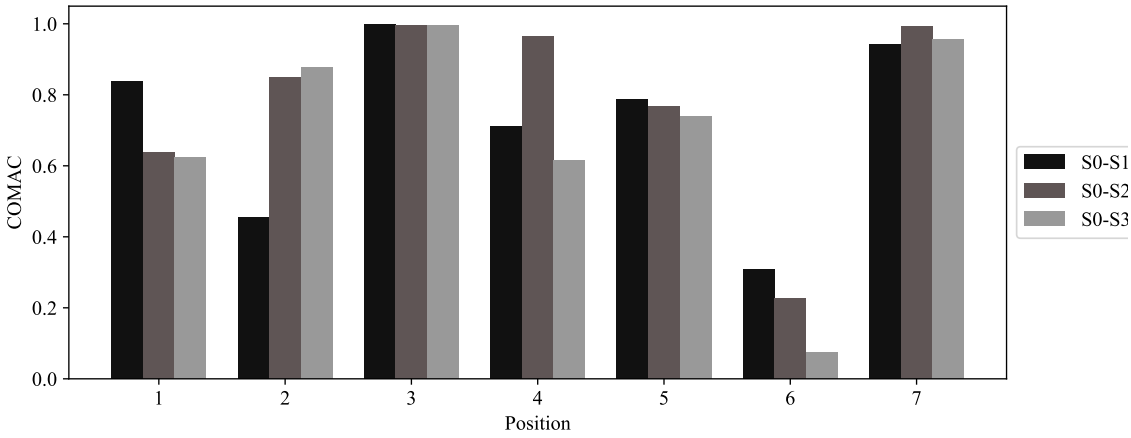

Source: Author (2025)

Figure 70 – COMAC coefficients – PCE-C model

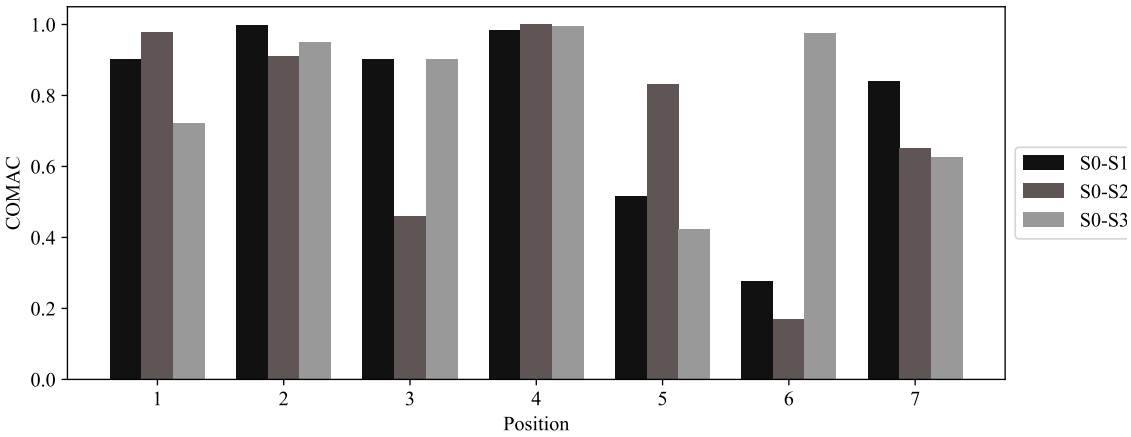

Source: Author (2025)

A similar trend was also observed in the PCO-C model.

An important observation regarding the COMAC values is that when all mode pairs are considered in the calculation, the indication of damage may be obscured by modes that are not sensitive to the damage, as emphasized by Doebling *et al.* (1996). This limitation could explain the unexpected behavior observed at certain measurement points in the analysis.

Moreover, the damage observed in the models was, for the most part, not localized within the wall. The loss of stiffness, as evidenced in the static response curves, suggests that the damage primarily resulted from internal micro-cracking. This condition may have limited the effectiveness of the COMAC index in this context. Nevertheless, variations detected in the MAC values and natural frequencies indicated the presence of damage and proved effective for assessing the structural integrity of the masonry walls.

6 CONCLUSIONS

This study evaluated the dynamic behavior of unreinforced masonry walls constructed with different materials and explored damage identification techniques based on modal parameters. To this end, reduced-scale physical models of walls were built, and ambient vibration tests were conducted on these specimens.

To ensure reliable prediction of the desired parameters and to gain a comprehensive understanding of the material behavior, a thorough characterization of the masonry components was conducted. In this phase, both mechanical properties related to the stiffness of the elements and physical properties associated with mass were evaluated. For the determination of the dynamic elastic modulus, special emphasis was placed on the use of non-destructive acoustic resonance testing, applied to both the mortar and the blocks. In the case of concrete and clay blocks, whose geometry does not conform to standard specifications for this type of test, an established novel methodology was adopted methodology was adopted, combining numerical analysis – through the assessment of vibration modes and parametric studies – with experimental determination of natural frequencies via acoustic tests. This approach successfully enabled the evaluation of the blocks' elastic modulus, representing a significant contribution of the work. Ultimately, the results for both materials aligned with expected values, reinforcing the effectiveness of the adopted methodology. Additionally, the compressive strength of blocks and prisms was measured, confirming the structural adequacy of the masonry used in this study. This characterization step was essential not only for the development of a finite element model capable of predicting mode shapes and natural frequencies consistent with those observed in the experimental tests, but also for determining the load levels used in the static test.

The preliminary numerical model was developed for both wall configurations: walls made of concrete blocks and walls made of clay blocks. The goal of this preparatory analysis was to gain prior insight into the dynamic behavior of the structure and, consequently, to conduct the dynamic tests with greater precision and reliability. This approach allowed for the strategic placement of accelerometers, ensuring effective capture of the main natural frequencies and vibration modes. Furthermore, it enabled the estimation of a suitable acquisition frequency for the dynamic tests based on the magnitude of the predicted frequencies, as well as an initial assessment of the modal participation factors.

Six panels were constructed—three for each block typology. For each material, three levels of pre-compression intensity were defined to evaluate the influence of this condition on the static and dynamic behavior of the models. Cycles of horizontal force application were also established to induce damage due to bending and shear—mechanisms commonly observed in shear walls and in infill masonry walls subjected to lateral loads. The static

shear tests on the wall models were successfully conducted. The applied pre-compression and lateral loads matched the expected values, and the resulting failure patterns were consistent with anticipated behavior, characterized mainly by diagonal cracking.

Following the static tests, which induced various damage states, ambient vibration tests were performed to identify the in-plane and out-of-plane modal properties of the masonry walls. Acceleration data were collected for all physical models using three distinct and independent setups, each designed to capture different mode types. Measurements were repeated after each cycle of lateral loading. Distinct peaks were identified in the averaged normalized power spectral density plots, and overlaying these plots enabled the interpretation of the sequence of in-plane and out-of-plane modes. This technique proved effective, as the natural frequencies were sufficiently spaced and the vibration levels allowed for the identification of several modes with high coherence.

The data obtained from these tests revealed a consistent decrease in the natural frequencies corresponding to the same vibration modes across all models as damage progressed—even in cases where no visible cracks were observed. This behavior is in line with structural dynamics theory, which establishes a direct relationship between stiffness and dynamic properties. However, the reduction in frequency was more pronounced for certain modes than for others. The MAC coefficient was used to consistently track the identified vibration modes across all damage stages. To ensure a correlation above 0.8, some results from specific models had to be excluded; however, the remaining data exhibited the expected behavior.

The comparison of natural frequencies confirmed the presence of damage, as did the MAC, which showed sensitivity even at early stages. The COMAC index also indicated reduced correlation in expected regions; however, because this metric is based on modal displacements from multiple vibration modes, its interpretation can be less intuitive. This is especially true in the case of the models studied, where the damage was not localized, and visible cracks were only observed in models PCO-A and PCE-B during the stages prior to failure.

This work and its methodology demonstrate the viability of employing non-destructive techniques—such as dynamic analysis—for the monitoring of masonry structures. The applied methods, along with the damage indicators analyzed, show strong potential for application to real-scale structures in the assessment of their structural integrity.

As recommendations for future studies aimed at enhancing dynamic analysis and damage detection in masonry walls, the following points are suggested:

- Employ more robust identification methods, including time-domain techniques, to improve the quality of extracted data and enable a more comprehensive comparison

between parameters obtained from different approaches.

- Explore additional damage identification techniques derived from modal parameters, such as mode shape curvature and strain mode shapes, in order to increase the reliability of the methodologies applied to masonry models.
- Introduction of damage in the numerical model for subsequent comparison with the experimentally observed behavior, enabling the evaluation and comparison of damage identification techniques in such scenarios.
- Conduct comparisons with full-scale models and real structures to better understand scale effects in dynamic analyses and to validate the findings obtained from reduced-scale specimens.
- Perform calibration and updating of the numerical model based on experimental data, enabling parametric analyses and sensitivity studies that broaden the scope of investigation into the dynamic behavior of masonry structures.

REFERENCES

ABDEL WAHAB, M. M.; DE ROECK, G. Damage detection in bridges using modal curvatures: application to a real damage scenario. **Journal of Sound and Vibration**, v. 226, n. 2, p. 217–235, 1999.

ALLEMANG, R. J. The modal assurance criterion–twenty years of use and abuse. **Sound and Vibration**, v. 37, p. 14–23, 2003.

ALLEMANG, R. J.; BROWN, D. L. Experimental modal analysis. *In*: HARRIS, C. M.; PIERSOL, A. G. (ed.). **Harris' Shock and Vibration Handbook**. New York: McGraw-Hill, 2002. p. 20.1–20.83.

ALVA, G. M. S.; MONTANDON, G. A. Structural models for analysis of reinforced concrete frame buildings with masonry infills. **Revista IBRACON de Estruturas e Materiais**, v. 12, p. 1058–1085, Out. 2019.

ALVES, H.; OTANI, L. B. **Determinação dos módulos de elasticidade do concreto empregando a Técnica de Excitação por Impulso (ABNT NBR 8522-1&2:2021)**. 2022. [S.l.: s.n.]. Available at: www.sonelastic.com. Access in: 23 June 2025.

AMERICAL SOCIETY FOR TESTING AND MATERIALS. **C215-14**: Standard test method for fundamental transverse, longitudinal, and torsional resonant frequencies of concrete specimens. Pennsylvania, 2014.

AMERICAL SOCIETY FOR TESTING AND MATERIALS. **E1876-22**: Standard test method for dynamic young's modulus, shear modulus, and poisson's ratio by impulse excitation of vibration. Pennsylvania, 2022.

AMERICAN CONCRETE INSTITUTE. **ACI 530-05**: Building code requirements for masonry structures. Detroit, 2005.

ANDREAUS, U. Failure criteria for masonry panels under in-plane loading. **Journal of Structural Engineering**, v. 122, n. 1, p. 37–46, 1996.

ANWAR, A. M.; ELWALY, A. M. A. Modal displacement vs curvature functions as damage identifier for masonry structures. **Alexandria Engineering Journal**, v. 68, p. 527–538, 4 2023.

ASSOCIAÇÃO BRASILEIRA DE NORMAS TÉCNICAS. **NBR 13279**: Mortars applied on walls and ceilings - determination of the flexural and the compressive strength in the hardened stage. Rio de Janeiro, 2005.

ASSOCIAÇÃO BRASILEIRA DE NORMAS TÉCNICAS. **NBR 7584**: Hardened concrete — evaluation of surface hardness by reflecting esclerometer — test method. Rio de Janeiro, 2012.

ASSOCIAÇÃO BRASILEIRA DE NORMAS TÉCNICAS. **NBR 6136**: Hollow concrete blocks for concrete masonry — requirements. Rio de Janeiro, 2016.

ASSOCIAÇÃO BRASILEIRA DE NORMAS TÉCNICAS. **NBR 15270-3**: Ceramic components - part 3: Structural and non-structural ceramic blocks - test methods. Rio de Janeiro, 2017.

ASSOCIAÇÃO BRASILEIRA DE NORMAS TÉCNICAS. **NBR 16868-1**: Structural masonry - part 1: Design. Rio de Janeiro, 2020.

ASSOCIAÇÃO BRASILEIRA DE NORMAS TÉCNICAS. **NBR 16868-3**: Structural masonry - part 3: Test methods. Rio de Janeiro, 2020.

ASSOCIAÇÃO BRASILEIRA DE NORMAS TÉCNICAS. **NBR 13281**: Mortars applied on walls and ceilings - requirements. Rio de Janeiro, 2023.

ASSOCIAÇÃO BRASILEIRA DE NORMAS TÉCNICAS. **NBR 15270-2**: Ceramic components - hollow and bricks for masonry - part 2: Test method. Rio de Janeiro, 2023.

AVCI, O. *et al.* A review of vibration-based damage detection in civil structures: from traditional methods to machine learning and deep learning applications. **Mechanical Systems and Signal Processing**, v. 147, Jan. 2021.

AVITABILE, P. Experimental modal analysis: a simple non-mathematical presentation. **Sound and Vibration**, v. 35, p. 20–31, 2001. Access in: 25 June 2025. Available at: https://api.semanticscholar.org/CorpusID:53000019.

BACHMANN, H. *et al.* **Vibration Problems in Structures**: practical guidelines. Basel: Springer Basel AG, 1995.

BENDAT, J.; PIERSOL, A. **Random Data**: analysis and measurement procedures. [*S.l.: s.n.*]: Wiley, 2011. (Wiley Series in Probability and Statistics).

BERNAT-MASÓ, E.; GIL, L. Assessing the performance of cfrp strengthening on masonry walls using experimental modal analysis. **Engineering Structures**, v. 193, p. 184–193, Aug. 2019.

BHASKAR, J. K.; BHUNIA, D.; PALCHURI, N. Numerical simulation of rc-masonry infill wall system strengthened with textile reinforced concrete. **Materials Today: Proceedings**, 2023.

BKSV. **Heavy-duty impact hammers types 8207, 8208 and 8210**. Brüel & Kjær Sound & Vibration Measurement A/S, 2012. Access in: 5 jun. 2025. Available at: https://www.bksv.com/-/media/literature/Product-Data/bp2079.ashx.

BKSV. **LDS V8900 shaker**. Brüel & Kjær Sound & Vibration Measurement A/S, 2019. Access in: 5 jun. 2025. Available at: https://www.bksv.com/-/media/literature/Product-Data/bp2560.ashx.

BOUARROUDJ, M. A.; BOUDAOUD, Z. Comparison between numerical modeling approaches of infilled frames under in-plane load. **Frontiers in Built Environment**, v. 7, 2022.

BRASIL, R. M. L. R. F.; SILVA, M. A. **Introdução à dinâmica das estruturas para a engenharia civil**. 2. ed. São Paulo: Blucher, 2015.

BRINCKER, R. Some elements of operational modal analysis. **Shock and Vibration**, v. 2014, p. 1–11, 2014.

BRINCKER, R. *et al.* Modal analysis of civil engineering structures using operational techniques. *In*: **13th International Modal Analysis Conference (IMAC)**. Nashville: Dept. of Building Technology and Structural Engineering, Aalborg University, 1995. p. 12. Fracture and Dynamics, No. 61. PDF for print: 12 pp.

CAETANO, E. **Identificação experimental de parâmetros dinâmicos em sistemas estruturais**. 1992. Dissertação (Mestrado) — Faculty of Engineering, University of Porto, Portugal, 1992.

CAPUZZO NETO, V. **Interação de paredes em alvenaria estrutural cerâmica sob ações verticais**. 2015. Tese (Doutorado) — Universidade de São Paulo, Escola de Engenharia de São Carlos, São Carlos, 2015.

CASABURO, A. *et al.* **A review of similitude methods for structural engineering**. [*S.l.: s.n.*]: American Society of Mechanical Engineers (ASME), 2019.

CERAVOLO, R. *et al.* Vibration-based monitoring and diagnosis of cultural heritage: a methodological discussion in three examples. **International Journal of Architectural Heritage**, v. 10, p. 375–395, 2016.

CHOPRA, A. K. **Dynamic of structures**: theory and applications to earthquake engineering. 5th. ed. [*S.l.: s.n.*]: Pearson, 2020.

CLOUGH, R. W.; PENZIEN, J. **Dynamics of structures**. 3. ed. Berkeley, California: Computers and Structures, Inc., 2003.

COOLEY, J. W.; TUKEY, J. W. An algorithm for the machine calculation of complex fourier series. **Mathematics of Computation**, v. 19, n. 90, p. 297–301, 1965.

COSTIGAN, A.; PAVÍA, S.; KINNANE, O. An experimental evaluation of prediction models for the mechanical behavior of unreinforced, lime-mortar masonry under compression. **Journal of Building Engineering**, v. 4, p. 283–294, Dec. 2015.

CUNHA, A.; CAETANO, E. Experimental modal analysis of civil engineering structures. **Sound and Vibration**, v. 40, June 2006.

DOEBLING, S. *et al.* **Damage identification and health monitoring of structural and mechanical systems from changes in their vibration characteristics**: a literature review. Los Alamos, NM: [*S.l.: s.n.*], 1996. Access in: 25 June 2025. Available at: http://www.osti.gov/servlets/purl/249299-n4r7Vr/webviewable/.

DÖNMEZ, C.; ÇANKAYA, M. A. Effect of infill walls on the drift behavior of reinforced concrete frames subjected to lateral-load reversals. **Journal of Earthquake Engineering**, v. 17, n. 5, p. 611–636, Feb. 2013.

DØSSING, O.; KJÆR, B. . **Structural testing part I**: mechanical mobility measurements. Nærum: Brüel & Kjær, 1988. Access in: 25 June 2025. Available at: https://www.bksv.com/media/doc/br0458.pdf.

DRYSDALE, R.; HAMID, A.; BAKER, L. **Masonry structures**: behavior and design. Cambridge: Prentice Hall, 1994.

EUROPEAN COMMITTEE FOR STANDARDIZATION. **EN 1996-1-1: Eurocode 6**: General rules for reinforced and unreinforced masonry structures. Belgium, 2005.

EWINS, D. **Modal testing**. [*S.l.: s.n.*]: Wiley, 1984. (Engineering dynamics series).

EWINS, D. J. Modal analysis, experimental: basic principles. *In*: **Encyclopedia of Vibration**. Oxford: Elsevier, 2001. p. 805–813.

FAN, W.; QIAO, P. Vibration-based damage identification methods: a review and comparative study. **Structural Health Monitoring**, v. 10, p. 83–111, Jan. 2011.

FEIJÃO, A. C. M. **Avaliação de índices modais para identificação de danos em passarelas metálicas**. 2023. Dissertação (Mestrado) — Pontifícia Universidade Católica do Rio de Janeiro, Rio de Janeiro, 2023. Access in: 25 June 2025. Available at: https://doi.org/10.17771/PUCRio.acad.63038.

GADE, S.; HERLUFSEN, H.; KONSTANTIN-HANSEN, H. How to determine the modal parameters of simple structures. **Sound & Vibrations**, v. 36, n. 1, p. 72–73, 2002.

HAACH, V. **Development of a design method for reinforced masonry subjected to in-plane loading based on experimental and numerical analysis**. 2009. Tese (Doutorado) — Universidade do Minho - Escola de Engenharia, Guimarães, 2009.

HAACH, V. G. *et al.* Application of acoustic tests to mechanical characterization of masonry mortars. **NDT and E International**, v. 59, p. 18–24, 2013.

HAACH, V. G.; VASCONCELOS, G.; LOURENÇO, P. B. Influence of aggregates grading and water/cement ratio in workability and hardened properties of mortars. **Construction and Building Materials**, v. 25, p. 2980–2987, June 2011.

HAMID, A. A.; SCHULLER, M. **Assessment and retrofit of masonry structures**. [*S.l.: s.n.*]: The Masonry Society, 2019.

HARRIS, C. M.; PIERSOL, A. G. **Harris' Shock and Vibration Handbook**. 5. ed. New York: McGraw-Hill, 2002. (McGraw-Hill Handbooks).

HARRIS, H. G.; SABNIS, G. M. **Structural modeling and experimental techniques**. 2. ed. Boca Raton, FL: CRC Press, 1999. 808 p.

HOU, R.; XIA, Y. Review on the new development of vibration-based damage identification for civil engineering structures: 2010–2019. **Journal of Sound and Vibration**, v. 491, Jan. 2021.

IBRAHIM, S. R. Fundamentals of time domain modal identification. *In*: SILVA, J. M. M.; MAIA, N. M. M. (ed.). **Modal Analysis and Testing**. Dordrecht: Springer Netherlands, 1999. p. 241–250.

JOHANSSON, P. **Vibration of hollow core concrete elements induced by walking**. Box 118, S-221 00 Lund, Sweden: [*S.l.: s.n.*], 2009.

JULIANI, T. M. **Detecção de danos em pontes em escala reduzida pela identificação modal estocástica**. 2014. Dissertação (Mestrado) — Universidade de São Paulo, Escola de Engenharia de São Carlos, São Carlos, 2014.

KOMUR, M. A.; KARA, M. E.; DENEME, I. O. Infill wall effects on the dynamic characteristics of rc frame systems via operational modal analysis. **Structural Engineering and Mechanics**, v. 74, p. 121–128, Apr. 2020.

LOURENÇO, P. B. **Computational Strategy for Masonry Structures**. 1996. Tese (Doutorado) — Deft University of Technology, Netherlands, 1996.

MAGALHÃES, F.; CUNHA, Á. Explaining operational modal analysis with data from an arch bridge. **Mechanical Systems and Signal Processing**, v. 25, n. 5, p. 1431–1450, July. 2011.

MAIA, N. M. M. Modal identification methods in the frequency domain. *In*: SILVA, J. M. M.; MAIA, N. M. M. (ed.). **Modal analysis and testing**. Dordrecht: [*S.l.: s.n.*], 1999. p. 251–264.

MAIA, N. M. M. Modal analysis, experimental: parameter extraction methods. *In*: **Encyclopedia of Vibration**. [*S.l.: s.n.*]: Elsevier, 2001. p. 820–824.

MAIA, N. M. M.; SILVA, J. M. M. Modal analysis identification techniques. **Philosophical Transactions of the Royal Society of London. Series A: Mathematical, Physical and Engineering Sciences**, v. 359, n. 1778, p. 29–40, Jan. 2001.

MARCOS, L. K. **Sensibilidade a vibrações de pavimentos com lajes alveolares**. 2015. Dissertação (Mestrado) — Universidade de São Paulo, Escola de Engenharia de São Carlos, São Carlos, 2015.

MASCIOTTA, M.-G.; RAMOS, L. F. Dynamic identification of historic masonry structures. *In*: **Long-term Performance and Durability of Masonry Structures**. [*S.l.: s.n.*]: Elsevier, 2019. p. 241–264.

MAURÍCIO, R. M. **Estudo teórico e experimental das ligações diretas contra-fiadas entre paredes de blocos de concreto em escala real e reduzida 1:4**. 2005. Tese (Doutorado) — Universidade de São Paulo, Escola de Engenharia de São Carlos, São Carlos, 2005.

MAYO, S. **Practical understanding of key accelerometer specifications**. [*S.l.*], 2022. Access in: 25 June 2025. Available at: https://www.endevco.com/resources/technical-papers/328-practical-understanding-key-accelerometer-specifications.

MILANI, A. S. *et al.* Case study of prototype and small-scale model behavior of clay blocks masonry under compression. **Case Studies in Construction Materials**, v. 15, Dec. 2021.

MOREIRA, E. M. d. S. **Análise experimental em escala reduzida de ligações entre paredes de alvenaria estrutural de blocos cerâmicos submetidas a ações verticais**. 2007. Dissertação (Mestrado) — Universidade de São Paulo, Escola de Engenharia de São Carlos, São Carlos, 2007.

NADERPOUR, H.; FAKHARIAN, P. A synthesis of peak picking method and wavelet packet transform for structural modal identification. **KSCE Journal of Civil Engineering**, v. 20, p. 2859–2867, Nov. 2016.

NASCIMENTO NETO, J. A. do. **Estudo de painéis com abertura constituídos por alvenaria estrutural de blocos**. 2003. Tese (Doutorado) — Universidade de São Paulo, Escola de Engenharia de São Carlos, São Carlos, 2003.

NICOLETTI, V. *et al.* Vibration-based tests and results for the evaluation of ifill masonry walls influence on the dynamic behaviour of buildings: a review. **Archives of Computational Methods in Engineering**, v. 29, p. 3773–3787, Dec. 2022.

NÓBREGA, P. G. B. d. **Análise dinâmica de estruturas de concreto: estudo experimental e numérico das condições de contorno de estruturas pré-moldadas**. 2005. Tese (Doutorado) — Universidade de São Paulo, Escola de Engenharia de São Carlos, São Carlos, 2005.

ORCESI, A. *et al.* Investigating the effects of climate change on structural actions. **Structural Engineering International**, v. 32, p. 563–576, 2022.

OYARZO-VERA, C.; CHOUW, N. Damage identification of unreinforced masonry panels using vibration-based techniques. **Shock and Vibration**, v. 2017, p. 1–14, 2017.

PACÍFICO, A. L. **Análise dimensional e semelhança**. 2017. Access in: 17 May 2024. Available at: https://edisciplinas.usp.br/pluginfile.php/2889753/mod_resource/content/5/2.1-analise_dimensional_e_semelhanca.pdf.

PANDEY, A.; BISWAS, M.; SAMMAN, M. Damage detection from changes in curvature mode shapes. **Journal of Sound and Vibration**, v. 145, n. 2, p. 321–332, 1991.

PARSEKIAN, G. A.; HAMID, A. A.; DRYSDALE, R. G. **Comportamento e dimensionamento de alvenaria estrutural**. 2. ed. São Carlos: EdUFSCar, 2013. 1-723 p.

POTTER, D.; EREN, H. Data acquisition fundamentals. *In*: . [*S.l.: s.n.*], 2012. p. 330–341.

RAHMAN, A. G. *et al.* Enhancement of impact-synchronous modal analysis with number of averages. **Journal of Vibration and Control**, v. 20, p. 1645–1655, 2014.

RAINIERI, C.; FABBROCINO, G. **Operational modal analysis of civil engineering structures**. New York: Springer, 2014.

RAMALHO, M. A.; CORRÊA, M. R. S. **Projeto de edifícios de alvenaria estrutural**. São Paulo: [*S.l.: s.n.*], 2003. 188 p.

RAMOS, L. *et al.* Damage identification on arched masonry structures using ambient and random impact vibrations. **Engineering Structures**, v. 32, n. 1, p. 146–162, Jan. 2010.

RAMOS, L. F. **Damage identification on masonry structures based on vibration signatures**. 2007. Tese (Doutorado) — Universidade do Minho - Escola de Engenharia, Guimarães, 2007.

RAMOS, L. F. *et al.* Vibration based damage identification of masonry structures. *In*: **Proceedings of the international conference on structural analysis of historical constructions**. New Delhi: Macmillan India Ltd., 2006.

REYNOLDS, P.; PAVIC, A. Quality assurance procedures for the modal testing of building floor structures. **Experimental Techniques**, v. 24, n. 1, p. 36–41, 2000.

RODRIGUES, J. M. V. B. L. **Identificação modal estocástica. Métodos de análise e aplicações em estruturas de engenharia civil**. 2004. Tese (Doutorado) — Universidade do Porto, 2004.

RYTTER, A. **Vibration based inspection of civil engineering structures**. 1993. Tese (Doutorado) — Department of Building Technology and Structural Engineering, Aalborg University, Aalborg, Denmark, 1993.

SANTOS, E. A. F. *et al.* Evaluation of elastic modulus of concrete blocks using acoustic tests. *In*: **Proceedings of the 9th International Masonry Conference**. Guimarães, Portugal: [*S.l.: s.n.*], 2014.

SARHOSIS, V.; LEMOS, J. V. A detailed micro-modelling approach for the structural analysis of masonry assemblages. **Computers & Structures.**, v. 206, p. 66–81, Aug. 2018.

SHAN, S. *et al.* Effect of partial infill walls on collapse behavior of reinforced concrete frames. **Engineering Structures**, v. 197, Oct. 2019.

SILVA, J. M. M.; MAIA, N. M. M. (ed.). **Modal Analysis and Testing**. [*S.l.: s.n.*]: Springer Dordrecht, 1999. v. 355. (NATO Science Series E, v. 355).

SILVA, W. J. d. **Análise experimental e numérica da distribuição das ações verticais entre paredes de alvenaria estrutural com a utilização de modelo físico reduzido na escala 1:5**. 2014. Tese (Doutorado) — Universidade de São Paulo, Escola de Engenharia de São Carlos, São Carlos, 2014.

ŠIPOŠ, T. K.; RODRIGUES, H.; GRUBIŠIĆ, M. Simple design of masonry infilled reinforced concrete frames for earthquake resistance. **Engineering Structures**, v. 171, p. 961–981, Sept. 2018.

SOMBRA, T. N. **Aplicação do ensaio de ressonância acústica na caracterização mecânica de unidades de alvenaria estrutural**. 2020. Dissertação (Mestrado) — Universidade de São Paulo, Escola de Engenharia de São Carlos, São Carlos, 2020.

SOMBRA, T. N.; HAACH, V. G. Application of acoustic tests for the mechanical characterization of hollow masonry units. **Journal of Materials in Civil Engineering**, v. 34, June 2022.

SORIANO, H. L. **Introdução à dinâmica das estruturas**. Rio de Janeiro: Elsevier, 2014.

UEMURA, L. K. **Desenvolvimento e aplicação de formulações para simulação numérica do comportamento mecânico de elementos em alvenaria estrutural utilizando o Método dos Elementos Finitos**. 2023. Dissertação (Mestrado) — Universidade de São Paulo, Escola de Engenharia de São Carlos, São Carlos, 2023.

VAROTO, P. S. **Análise modal no domínio da frequência: um método de identificação multi-modos**. 1991. Dissertação (Mestrado) — Universidade de São Paulo, Escola de Engenharia de São Carlos, São Carlos, 1991.

VIRTANEN, P. *et al.* SciPy 1.0: Fundamental algorithms for scientific computing in python. **Nature Methods**, v. 17, p. 261–272, 2020.

ZAHID, F. B.; ONG, Z. C.; KHOO, S. Y. A review of operational modal analysis techniques for in-service modal identification. **Journal of the Brazilian Society of Mechanical Sciences and Engineering**, v. 42, Aug. 2020.

ZAHID, F. B. *et al.* Implementation of BCI based semi-automated impact device for performing impact synchronous modal analysis. **Measurement**, v. 208, Feb. 2023.

ZRAYKA, A. K.; MUCCHI, E. A comparison among modal parameter extraction methods. **SN Applied Sciences**, v. 1, n. 7, June 2019.

PPG
SET

EESC • USP